



HAL
open science

Cavity based high-fidelity and non-destructive single atom detection on an atom chip

Roger Gehr

► **To cite this version:**

Roger Gehr. Cavity based high-fidelity and non-destructive single atom detection on an atom chip. Atomic Physics [physics.atom-ph]. Université Pierre et Marie Curie - Paris VI, 2011. English. NNT : . tel-00593418

HAL Id: tel-00593418

<https://theses.hal.science/tel-00593418>

Submitted on 15 May 2011

HAL is a multi-disciplinary open access archive for the deposit and dissemination of scientific research documents, whether they are published or not. The documents may come from teaching and research institutions in France or abroad, or from public or private research centers.

L'archive ouverte pluridisciplinaire **HAL**, est destinée au dépôt et à la diffusion de documents scientifiques de niveau recherche, publiés ou non, émanant des établissements d'enseignement et de recherche français ou étrangers, des laboratoires publics ou privés.



THÈSE DE DOCTORAT DE L'UNIVERSITÉ PARIS VI

Spécialité : PHYSIQUE QUANTIQUE

présentée par

Roger P. GEHR

pour obtenir le grade de

Docteur de l'Université Paris VI

Sujet :

**Cavity based high-fidelity and non-destructive
single atom detection on an atom chip**

Soutenue le 13/05/2011 devant le jury composé de :

M ^{me}	BOUCHOULE ISABELLE	Institut d'Optique	Examineur
M.	ESCHNER JÜRGEN	Universität des Saarlandes	Examineur
M.	GRANGIER PHILIPPE	Institut d'Optique	Rapporteur
M.	KÖHL MICHAEL	Cambridge University	Rapporteur
M.	RAIMOND JEAN-MICHEL	Université Pierre et Marie Curie	Examineur
M.	REICHEL JAKOB	Université Pierre et Marie Curie	Directeur de thèse

Summary

In this thesis, we demonstrate the preparation and detection of single atoms on an atom chip. We prepare a single Rubidium atom strongly coupled to a high-finesse cavity integrated to the atom chip. The atom is extracted from a Bose-Einstein condensate and trapped at the maximum of the cavity field. The prepared system is reproducibly in the strong-coupling regime of cavity quantum electrodynamics, as shown by a measurement of the normal mode spectrum of the coupled system. We use the cavity reflection and transmission signal to infer the atomic hyperfine state with a fidelity exceeding 99.93% in a detection time of 100 microseconds. The atom remains trapped during the detection. This performance of the detector is comparable to the best ion-trap experiments and makes the detector suitable for error correcting schemes in the context of quantum information processing. Additionally, the cavity-based detection scheme greatly reduces scattering compared to optical detection schemes in free space. We measure the scattering rate during detection, and show that we are able to detect the atomic internal state with an error below 10% while scattering less than 0.2 photons on average. To finalize the characterization of the detection process, we analyze the projection of the atomic state due to the measurement by performing a quantum Zeno type experiment. We find that each photon incident on the cavity reduces the coherence of the atomic state by a factor of 0.7. The presented detection is close to the textbook example of a projective measurement of a two-level quantum system.

Résumé

Dans ce mémoire, nous démontrons la préparation et la détection d'atomes uniques sur une puce à atomes intégrant un résonateur optique de haute finesse. L'atome est extrait d'un condensat de Bose-Einstein et piégé à une position de couplage maximum au résonateur. Nous mesurons le spectre du système atome-cavité et démontrons qu'il se situe dans le régime de couplage fort. Ceci nous permet d'utiliser la transmission et la réflexion du résonateur pour déduire l'état hyperfin de l'atome. Nous obtenons une fidélité de détection de 99.93% avec un temps de détection de 100 microsecondes. L'atome reste piégé pendant la détection. Ces caractéristiques sont comparables à celles obtenues dans les expériences avec des ions piégés. Nous mesurons également le taux de diffusion de photons pendant la détection, et démontrons que nous détectons l'état interne de l'atome avec une erreur inférieure à 10% en diffusant en moyenne moins de 0.2 photons. Pour conclure la caractérisation du processus de détection, nous analysons la projection de l'état atomique due à la mesure en effectuant une expérience de type Zeno quantique. Nous démontrons que chaque photon incident sur la cavité réduit la cohérence de l'état atomique d'un facteur 0.7. La détection présentée est donc proche d'une mesure projective idéale pour un système quantique à deux niveaux.

Contents

Introduction	9
1. Cavity quantum electrodynamics with single atoms	13
1.1. Ideal case: Two atomic levels, one light mode	13
1.1.1. The Jaynes-Cummings model of the closed system	13
1.1.2. Master equation for an open system	16
1.1.3. Steady state solution to the master equation	18
1.1.4. Analysis of the steady state solution	19
1.2. Real-world atoms and cavities	21
1.2.1. Master equation for many levels and two light modes	21
1.2.2. Solution to the full master equation	24
1.3. Conclusion	27
2. Setup	29
2.1. Overview	29
2.2. Cold atoms and BEC on an atom chip	29
2.2.1. Atomchip and magnetic micro traps	29
2.2.2. Vacuum apparatus	31
2.2.3. Laser system for cold atoms	33
2.2.4. The optical setup around the vacuum chamber	34
2.3. The high-finesse cavity	34
2.3.1. Introduction	34
2.3.2. FFP laser system and locking scheme	38
2.3.3. Transfer cavity	41
2.4. Experimental sequence	43
2.4.1. From the magneto-optical trap to a BEC in the cavity	45
3. Coupling single atoms to the cavity	51
3.1. Introduction	51
3.2. Coupling of single atoms in a waveguide to the cavity	51
3.3. Microwave based single atom extraction	54
3.3.1. Heralded preparation of single atoms	54
3.3.2. The reservoir and single atom extraction	55
3.3.3. Reservoir removal	58
3.3.4. Zeeman-state preparation	59
3.3.5. Two atom probability	61

3.4. Characterisation of the single atom-cavity system	62
3.4.1. Dipole trap lifetime	62
3.4.2. Single atom internal state dynamics	63
3.5. Vacuum Rabi splitting	65
3.5.1. Spectroscopy of the strongly coupled system	65
3.5.2. Fluorescence single atom vacuum Rabi spectrum	67
3.6. Conclusion	69
4. Detection of a single atom hyperfine state	71
4.1. Introduction	71
4.1.1. Single atom state detection methods	72
4.1.2. Detection error and fidelity	73
4.2. Accessing the quantum state from photon counts	73
4.2.1. Counts thresholding in two dimensions	73
4.2.2. Maximum likelihood method	76
4.3. Experimental results	78
4.3.1. Measurement of the detection efficiency	78
4.3.2. Time dependency of the detection efficiency	80
4.4. Conclusion	83
5. Measurement backaction	85
5.1. Information gain and scattering in cavities and in free space	85
5.1.1. The minimum detection error	85
5.1.2. Backaction and scattering	88
5.2. Non-ideal cavities and measurements	91
5.2.1. Helstrom bound for our cavity	91
5.2.2. Photon counting and the Chernoff information	92
5.2.3. Scattering in non-ideal cavities	94
5.3. Experimental results: Scattering and accessible information	94
5.3.1. Experimental parameters	95
5.3.2. Measurement of Zeeman state diffusion and scattering rate	96
5.3.3. Detection error vs. scattering	97
5.4. Measurement of the Helstrom bound of the atom-cavity system	99
5.4.1. The quantum Zeno effect	99
5.4.2. Zeno effect on a single atom coupled to the cavity	99
5.4.3. Zeno effect for a single atom	101
5.4.4. The Helstrom bound	102
5.5. Conclusion	102
6. Conclusion and Outlook	107
A. Appendix	109
A.1. Rubidium data	109
A.1.1. Physical properties	109

Contents

A.1.2. Hyperfine structure	110
A.2. APD correction factor	111
A.3. Publications	112
Bibliography	113

List of Figures

1.1. The atom-cavity system	14
1.2. Jaynes-Cummings ladder	15
1.3. Jaynes-Cummings spectrum	16
1.4. Analytical solution to the JC master equation	20
1.5. Level scheme for the master equation	22
1.6. Full master equation solutions	25
1.7. Full master equation solutions	26
2.1. Setup overview	30
2.2. Basis and science chip	31
2.3. Vacuum apparatus	32
2.4. Relevant ^{87}Rb levels for laser cooling	33
2.5. Optical table setup 1	35
2.6. Optics around the chamber	36
2.7. FFP cavities on the atom chip	38
2.8. Science cavity lock chain	40
2.9. Science cavity lock scheme	42
2.10. Transfer cavity setup	43
2.11. Optical table setup 2	44
2.12. Important wires on the chip and their names	45
2.13. The chip P-Trap	46
2.14. Magnetic chip potentials	47
2.15. BEC transition	48
3.1. Waveguide trap chip wires	52
3.2. Atom transport through cavity	53
3.3. Telegraph signals	53
3.4. Waveguide detection histogram	54
3.5. Principle of single atom extraction	55
3.6. Reservoir preparation time line	56
3.7. Single atom extraction I	58
3.8. Single atom extraction II	58
3.9. Reservoir push out	60
3.10. Two atom probability	61
3.11. Dipole trap lifetime	63
3.12. Quantum jumps of a single atom	64
3.13. Hyperfine states lifetimes	64

3.14. Experimental vacuum Rabi splitting	66
3.15. Rabi splitting with $m_F = 0$ Preparation	68
3.16. Fluorescence vacuum Rabi splitting	69
4.1. Cavity detection principle	74
4.2. Calculated detection histogram	75
4.3. Maximum likelihood vs threshold detection	76
4.4. Detection histogram	79
4.5. Transmission and reflection detection histograms	81
4.6. Detection error vs. detection time	82
4.7. Detection histogram $2\mu s$	83
5.1. Cavity detection compared to shelving technique	87
5.2. Helstrom bound of free-space and cavity detection	90
5.3. Measurement light outgoing modes	91
5.4. The Chernoff bound	93
5.5. Level scheme	95
5.6. Level scheme	96
5.7. Measurement of Zeeman state diffusion	97
5.8. Detection error vs. scattered photons	98
5.9. The Zeno effect	100
5.10. Measurement of the Zeno effect	103
5.11. The cavity as a detector figure of merit	104
A.1. ^{87}Rb hyperfine structure	110
A.2. APD correction factor	111

List of Tables

2.1. Cavity parameters	39
4.1. Detection error	80
A.1. Physical properties of ^{87}Rb	109

Introduction

The study of the interaction between matter and light is at the very origin of quantum physics. Max Planck first proposed the quantization of the energy exchanged between the electromagnetic field and matter as a solution to the spectrum of black-body radiation [1]. Shortly after, the hypothesis was successfully expanded and applied to the photoelectric effect by Albert Einstein [2]. Since those early days of quantum mechanics, quantum electrodynamics (QED) has never ceased to be an area of active research. Today, a hundred years later, rapid technological progress enables fundamental tests as well as potential applications of basic quantum mechanics. A surge in experimental studies has ensued. At the heart of this experimental progress lies an ever increasing control over the quantum world.

Cavity quantum electrodynamics [3, 4] is based on the fascinating insight first put forward by Purcell [5] that the spontaneous emission rate of an atom can be dramatically increased by placing a resonator around the atom. By altering the boundary conditions on the electromagnetic field, a resonator "colors" the vacuum's mode density and thereby changes the radiative properties of the atom. The Purcell effect thus unequivocally demonstrates that the spontaneous emission rate is not an intrinsic characteristic of a quantum emitter but rather arises from the coupling to a large number of modes in a reservoir.

If one decreases the mode volume of the resonator, the coupling between the atom and the resonator mode is enhanced. In the extreme case where this coupling strength surpasses the decay rates associated with the atom and the cavity, new physics beyond the Purcell effect can be observed. In this so-called strong coupling regime, the atom and the light field can no longer be considered as separate systems, since entanglement between the atomic state and the cavity field state is created [6]. In this regime, cavity QED effectively implements the most elementary model of the interaction between a two-level atom and a single mode of the electromagnetic field first described by Jaynes and Cummings [7, 8].

Experimentally reaching the regime of strong coupling has proven to be a challenging task. Pioneering implementations of cavity QED were achieved with Rydberg atoms coupled to a high-finesse microwave cavity [6, 9–14]. Experiments with optical cavities followed suit [15–22]. More recently, artificially engineered quantum systems have been coupled to resonators in a variety of systems. Experiments with quantum dots coupled to Bragg-mirror cavities or photonic crystal microcavities in semiconductors [23–27] and superconducting Cooper-pair boxes embedded in strip-line microwave cavities [28–30] have been able to show strong coupling in their systems.

Experiments in the strong coupling regime have provided a fertile soil for groundbreaking results in experimental quantum mechanics. They have led to results such as

the observation of non-classical states and the measurement of their decoherence [31, 32], quantum non-demolition photon counting [33], or the realization of cavity optomechanics [34].

Practical applications of cavity QED have grown to considerable relevance with the rise of "information" as a central concept in quantum mechanics. Quantum information theory arose out of seminal contributions in particular by Feynman, who proposed a universal quantum computer [35–38] as well as a quantum simulation machine [39]. Since then, a host of quantum information protocols have been proposed for cavity QED systems [40–44]. Additionally, the coherent interaction between matter and light realized in strongly coupled systems makes them ideal candidates for coherent light-matter interfaces in quantum communications networks [45–50].

Common to all the experimental efforts in the field are the severe requirements imposed on experimental techniques. There needs to be a way to prepare the system in a well-defined initial quantum state. In order to preserve coherence over an experimental cycle, the system has to be well isolated from the environment. A mechanism is required to control the internal and external state of the system. For the creation of entanglement, strong interaction between sub-systems is required. Finally, it is of paramount importance to accurately detect the final state to read out the result of an experiment or computation.

Atomic physics has been successful in addressing many of these difficulties. Laser cooling and magnetic trapping of ensembles of atoms lead to unprecedented control over the external degrees of freedom. The motional ground state is routinely reached by performing evaporative cooling until Bose-Einstein condensation (BEC) takes place [51]. Similarly, trapped single ions can be cooled to their motional ground state by resolved sideband cooling [52].

Cavity QED experiments have taken advantage of some of these advances in atomic physics. Single atom cavity QED experiments often use magneto-optical traps as a source of cold atoms [53–55]. While this approach has been successful, the temperature of laser cooled atoms is too high to allow for very precise positioning of the atoms within the cavity mode [19, 55, 56]. Imperfect control over the coupling strength is the undesired consequence. Only recently have experiments been realized that combine a high-finesse cavity and a BEC [57, 58] that have the potential to overcome this difficulty.

In this thesis, we present results obtained with a single atom cavity QED system that presents a major step forward in control over internal and external degrees of freedom of the atom. The main results concern the preparation of ultracold single atoms from a BEC coupled to the cavity and the high-finesse and nondestructive detection of a qubit state encoded in the atom's internal state.

For the preparation, we make use of the tailored magnetic potentials available on an atom chip. A Bose-Einstein condensate is placed at a position of maximum coupling to the high-finesse cavity. We extract a single atom from the BEC and measure its coupling strength to the cavity, showing that all single atoms prepared in this way couple with identical strength to the cavity.

Since the atom-cavity system so prepared is in the high-cooperativity regime, cavity reflection and transmission are strongly dependent on the atom's hyperfine state. Ex-

exploiting this effect, we achieve a hyperfine state read-out fidelity of 99.93%, on par with the best ion trap experiments [59]. Additionally, the cavity based read-out scheme offers very fast detection times down to the submicrosecond range. Since the atom remains trapped after the state read-out, the method can also be used to prepare a well-defined hyperfine state.

Besides the low detection error, our detection scheme offers the advantage that it does not rely on scattering for the read-out of the state. It therefore avoids the most important source of heating of the traditional fluorescence detection method. We measure the scattering rate during detection and show that our system is well within the regime of energy exchange free measurements. A quantum Zeno effect experiment allows us to measure the projection of the atomic state our measurement causes. As a result, we show that our detection is very close to an ideal textbook example of a purely projective state measurement.

Overview

The organization of the thesis is as follows. The first chapter gives an introduction to the theory of strongly coupled atom-cavity systems. A master equation that takes into account the particularities of our experiment is presented and solved numerically. Chapter two presents the experimental setup and the basic experimental steps common to all experiments of this thesis. In the third chapter, the preparation of single atoms with controlled coupling to the cavity is described. Experimental results characterizing the coupled atom-cavity system are presented, in particular in the form of measured normal-mode spectra. Chapter five investigates the capacities of the high-finesse cavity to act as a hyperfine-state dependent single atom detector. Two detection methods are introduced, and both methods are shown to lead to a high-fidelity detection. Chapter five scrutinizes the measurement induced backaction on the single atom. Scattering during detection is quantified and its relation to the detection error mapped out. The decoherence of the atom's internal states caused by the detection is measured via the observation of a quantum Zeno effect. As a central result, it is shown that the cavity-based detection scheme is capable of a measurement that does not rely on energy exchange. Finally, the conclusion summarizes the results and presents an outlook on future experiments.

1. Cavity quantum electrodynamics with single atoms

This chapter gives an introduction to the theoretical framework underlying strongly coupling cavity QED. The basic model, the Jaynes-Cummings Hamiltonian, is introduced at first. In order to be able to take incoherent losses into account, the master equation approach is used. Finally, a more realistic model of our atom-cavity system is discussed. It takes into account birefringence of cavity mirrors, multiple atomic levels and light shifts due to the dipole trap. The resulting master equation is numerically solved for our parameters.

1.1. Ideal case: Two atomic levels, one light mode

A single two-level atom coupled to a single mode of the electromagnetic field is one of the simplest quantum systems one can imagine. This system can be realized using a high-finesse resonator (see figure 1.1). When neglecting the decay channels of the atom and the cavity, the system is described by the Jaynes-Cummings Hamiltonian [7]. The most important characteristics of the system is already present in this very simple model. For experimental applications, the decay channels however are of paramount importance, since they provide a means of interaction with and read-out of the system. In the following, we discuss the formalism used to describe both the closed and open system.

1.1.1. The Jaynes-Cummings model of the closed system

The Jaynes-Cummings model considers a single point-like atom with two internal energy levels, called $|g\rangle$ and $|e\rangle$, coupled via electrical dipolar interaction to the quantized light field of an optical resonator. The Hamiltonian describing the system in the rotating wave and dipole approximation is the Jaynes-Cummings Hamiltonian, given by

$$\hat{H}_{JC} = \hbar\omega_a\hat{\sigma}^+\hat{\sigma}^- + \hbar\omega_c\hat{a}^\dagger\hat{a} + \hbar g_0(\hat{a}^\dagger\hat{\sigma}^- + \hat{\sigma}^+\hat{a}), \quad (1.1)$$

where $\hat{\sigma}^- \equiv |g\rangle\langle e|$ and $\hat{\sigma}^+ \equiv |e\rangle\langle g|$ are the atomic lowering and rising operators, and $\omega_a/2\pi$ and $\omega_c/2\pi$ are the atomic and cavity resonance frequencies and \hat{a} and \hat{a}^\dagger are the destruction and creation operator for photons, obeying the canonical commutation relation for bosons, $[\hat{a}, \hat{a}^\dagger] = 1$. The strength of the interaction is described by the

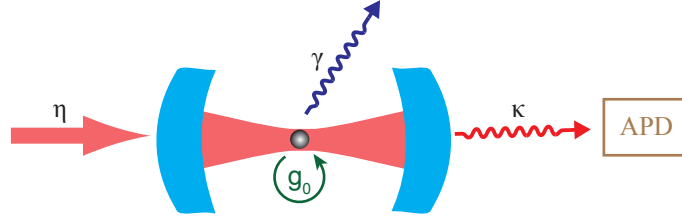


Figure 1.1.: A sketch of the atom-cavity system. A single atom is coupled to the single mode of the electromagnetic field resonant to a high-finesse optical cavity. The coherent coupling constant is g_0 . The system is coherently pumped by a laser through one of the cavity mirrors. The pump strength is η . Two decay channels exist: One is through spontaneous emission of photons into free space from the excited atom with rate 2γ , the other is through optical losses through the cavity mirrors with rate 2κ . In typical experiments, the photons leaking from the cavity are detected by an avalanche photodiode to observe the system.

coupling constant g_0 , defined as

$$g_0 = \sqrt{\frac{\omega_c}{2\hbar\epsilon_0 V}} \cdot \mu_{eg}. \quad (1.2)$$

g_0 therefore depends on the mode volume V and the dipole matrix element μ_{eg} of the atomic transition. The mode volume for a Gaussian beam is given by

$$V = \pi\omega_0^2 L_c/4 \quad (1.3)$$

where L_c is the resonator length and ω_0 the TEM₀₀ mode waist.

In general, the effective coupling constant g also depends on the localization of the atom,

$$g(\vec{r}) = g_0\psi(\vec{r}) \quad (1.4)$$

$$\psi(\vec{r}) = \cos(kx)e^{-(y^2+z^2)/\omega_0^2}. \quad (1.5)$$

Here, $\psi(\vec{r})$ is the spatial mode of the TEM₀₀ resonator mode with wave number $k = \omega_c/c$ and waist ω_0 .

The Jaynes-Cummings Hamiltonian is very simple, yet contains the most important features of quantized matter-light interactions: $\hat{\sigma}^\dagger\hat{a}$ describes the absorption of a photon by the atom, $\hat{\sigma}\hat{a}^\dagger$ describes the inverse process of the emission of a photon by the atom. The Jaynes-Cummings Hamiltonian can be diagonalized to obtain the eigenstates of the coupled system. The ground state of the system is $|g, 0\rangle$, with the atom in the ground state and the electromagnetic field in the vacuum state. The other eigenstates of the coupled system are so-called dressed states, linear superpositions of the states $|g, n\rangle$ (atom in the ground state and n photons in the cavity) and $|e, n-1\rangle$ (atom in the

excited state and $n - 1$ photons in the cavity. They can be written as

$$|n+\rangle = \cos \theta_n |e, n-1\rangle + \sin \theta_n |g, n\rangle \quad (1.6)$$

$$|n-\rangle = -\sin \theta_n |e, n-1\rangle + \cos \theta_n |g, n\rangle. \quad (1.7)$$

The mixing angle θ_n is determined by the coupling g_0 as well as the cavity-atom detuning $\Delta_{ca} = \omega_c - \omega_a$:

$$\theta_n = \arctan \frac{g_0 \sqrt{n}}{-\Delta_{ca}/2 + \sqrt{g_0^2 n + (\Delta_{ca}/2)^2}}. \quad (1.8)$$

The energy eigenvalues of the system form a ladder of doublets. The splitting of the

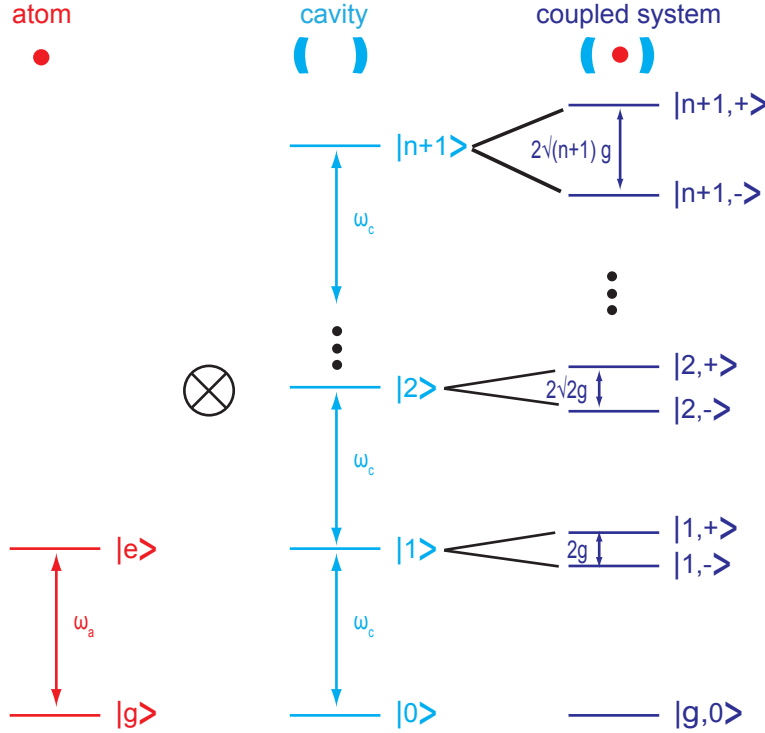


Figure 1.2.: The Jaynes-Cummings model. A single two-level atom is coupled to one mode of the electromagnetic field. The electromagnetic field is represented by a harmonic oscillator with an infinite number of levels spaced by the photon energy. The coupling of the system leads to a splitting in the energy levels, such that a structure of a ladder of doublets emerges. The splitting between the doublet states increases with the square root of the principal quantum number n of the mode, making the coupled system anharmonic.

doublets increases with the square root of the photon number n (see figure 1.2)

$$E_{n,+} = n\hbar\omega_c + \frac{\hbar}{2} \left(-\Delta_{ca} + \sqrt{\Delta_{ca}^2 + 4g_0^2 n} \right) \quad (1.9)$$

$$E_{n,-} = n\hbar\omega_c + \frac{\hbar}{2} \left(-\Delta_{ca} - \sqrt{\Delta_{ca}^2 + 4g_0^2 n} \right) \quad (1.10)$$

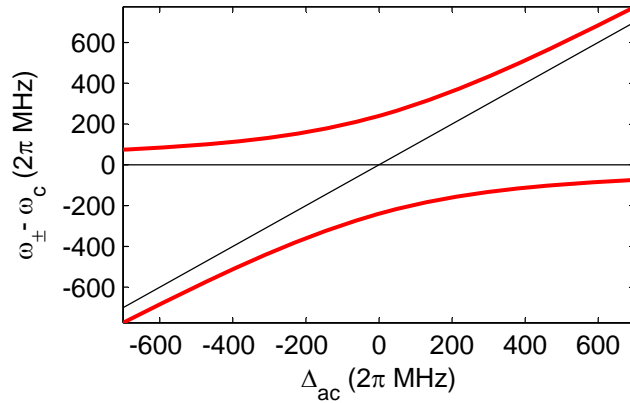


Figure 1.3.: The spectrum of the Jaynes-Cummings Hamiltonian with a single excitation ($n=1$) and $g_0/2\pi = 240$ MHz for different values of Δ_{ac} . For the y-axis, ω_+ (resp. ω_-) is defined as $E_{1,+}/\hbar$ (resp. $E_{1,-}/\hbar$).

The variation of the dressed energies as a function of Δ_{ac} is represented in figure 1.3 for $n = 1$. Note that for large detunings, the coupled states are only slightly shifted from the uncoupled atomic or cavity states. At zero detuning $\Delta_{ac} = 0$ however, the dressed energies show an avoided crossing, where the minimal energy difference, $\min(E_{1,+} - E_{1,-})$, is the coupling energy $2\hbar g_0$. This is the so-called vacuum-Rabi splitting.

1.1.2. Master equation for an open system

The Jaynes-Cummings Hamiltonian describes a closed quantum system, where no energy is exchanged between the atom-cavity system and the environment. The interaction of the system with the environment is neglected. In experimental situations however, the system under consideration cannot be completely shut off from interaction with the environment. An energy exchange and the loss of coherence from the system has to be taken into account. The main sources of decoherence in the optical domain are the process of spontaneous emission of the atom into free space and the loss of photons from the cavity. While these damping mechanisms lead to the often unwanted loss of coherence, they also allow to collect information of the system. Another experimentally vital part not included in the Jaynes-Cummings Hamiltonian is the pump process required to probe the system.

The master equation framework [60] allows to extend the Jaynes-Cummings model to include these processes. To obtain the master equation, the joint evolution of the system and its environment is calculated. The environment is modeled as a reservoir of modes, i.e. the collection of all free-space modes that couple to either the atom or the cavity. It is assumed that correlations within the reservoir decay on a timescale much faster than the timescale of the interaction with the system. The state of the reservoir is therefore independent of the state of the system, meaning that the environment does

not contain any information of the state of the system at earlier times. This assumed lack of memory on the part of the environment is the Markov approximation, which is satisfied with the reservoirs encountered in quantum optics.

The master equation for the density matrix ρ of a system takes the general linear form

$$\dot{\rho} = \mathcal{L}\rho, \quad (1.11)$$

where \mathcal{L} is the Liouvillian superoperator. It is given by

$$\mathcal{L}\rho = -\frac{i}{\hbar} [H, \rho] + \sum_i \gamma_i \mathcal{D}[\hat{c}_i]\rho, \quad (1.12)$$

where H is the Hamiltonian of the system, and the decay superoperator $\mathcal{D}[\hat{c}_i]$ takes into account the decay process associated with operator c_i and decay rate $2\gamma_i$. It is defined as

$$\begin{aligned} \mathcal{D}[\hat{c}]\rho &\equiv 2\hat{c}\rho\hat{c}^\dagger - \{\rho, \hat{c}^\dagger\hat{c}\} \\ &= 2\hat{c}\rho\hat{c}^\dagger - \hat{c}^\dagger\hat{c}\rho - \rho\hat{c}^\dagger\hat{c}, \end{aligned} \quad (1.13)$$

where $\{\cdot, \cdot\}$ is the anti-commutator. In our case, the two loss processes are cavity decay at a rate 2κ and atomic spontaneous emission at a rate 2γ . The master equation therefore reads

$$\dot{\rho} = -i[\hat{H}, \rho] + \kappa\mathcal{D}[\hat{a}]\rho + \gamma\mathcal{D}[\hat{\sigma}]\rho. \quad (1.14)$$

The contribution of an external pump field can be added to the Jaynes-Cummings Hamiltonian in a term of the form ([61])

$$\hat{H}_{pump} = -i\eta(\hat{a}e^{i\omega_p t} - \hat{a}^\dagger e^{-i\omega_p t}), \quad (1.15)$$

such that the total Hamiltonian in a frame rotating with ω_p becomes

$$\hat{H} = \Delta_{ap}\hat{\sigma}^+\hat{\sigma}^- + \Delta_{cp}\hat{a}^\dagger\hat{a} + g_0(\hat{a}^\dagger\hat{\sigma}^- + \hat{\sigma}^+\hat{a}) - i\eta(\hat{a} - \hat{a}^\dagger). \quad (1.16)$$

The definitions of the detunings are $\Delta_{ap} = \omega_a - \omega_p$ and $\Delta_{cp} = \omega_c - \omega_p$.

Coupling regimes

In order for the Hamiltonian evolution of the master equation 1.14 to be observable before the decay terms lead to a loss of coherence, g_0 needs to be larger than the decay rates of the atom γ and the cavity κ . This is the condition for strong coupling in cavity QED:

$$g_0 > \kappa, \gamma \quad (1.17)$$

Systems, for which $g_0 < \kappa$ are said to be in the "bad cavity" limit. Other characteristics of the system are described by the critical photon number, $n_0 = \gamma^2/g_0^2$ and the critical atom number $N_0 = 2\kappa\gamma/g_0^2$. The critical photon number n_0 gives the maximum number of photons in the resonator before the coherent interaction starts to saturate the atom.

The critical atom number N_0 gives the mean number of atoms that need to be coupled to the resonator in order for the coherent interaction to be dominant. The inverse of the critical atom number is the cooperativity, defined as

$$C = \frac{g_0^2}{2\kappa\gamma} \quad (1.18)$$

An intuitive understanding of the cooperativity is most easily obtained by considering the Purcell effect.

Purcell effect

In free space, an atom in the excited state decays spontaneously to its ground state with a typical time constant $1/\gamma$ while emitting a photon. The addition of a resonator to the system influences the situation quite strongly. The emission of the photon now occurs predominantly into the resonator mode. In the bad cavity limit, the photon is then lost through the cavity mirrors. Purcell predicted this effect [5], and it was first measured using microwave resonators and atoms in a Rydberg state [62]. The altered emission rate γ' of the coupled atom is

$$\gamma' = \gamma + \frac{g_0^2}{\kappa} = (1 + 2C)\gamma. \quad (1.19)$$

The factor $(1+2C)$ is called the Purcell factor. The cooperativity is here seen to be the ratio between the spontaneous emission rate into the cavity mode and the emission rate into free space.

1.1.3. Steady state solution to the master equation

The master equation 1.14 can be solved analytically in the weak excitation limit. In this limit, only the ground state $|g, 0\rangle$ and first doublet states $|g, 1\rangle$ and $|e, 0\rangle$ are populated. In this approximation, the algebra of the pseudo-spin operators σ^+ , σ^- and σ_z can be approximated by the harmonic oscillator algebra. The solution in this limit was first calculated by Hechenblaikner [63] (see also [64]).

Here, we are interested in the steady state solution given by $\mathcal{L}\rho_{ss} = 0$. The following notations simplify the expressions for the steady state solution:

$$\tilde{\Delta}_{ap} = \Delta_{ap} - i\gamma \quad (1.20)$$

$$\tilde{\Delta}_{cp} = \Delta_{cp} - i\kappa \quad (1.21)$$

$$(1.22)$$

Using this notations, the steady-state expectation values for the intracavity photon number $\langle a^\dagger a \rangle_{ss}$ and the atomic excitation $\langle \sigma^+ \sigma^- \rangle_{ss}$ read

$$\langle a^\dagger a \rangle_{ss} = \eta^2 \frac{|\tilde{\Delta}_{ap}|^2}{|g_0^2 - \tilde{\Delta}_{ap}\tilde{\Delta}_{cp}|^2} \quad (1.23)$$

$$\langle \sigma^+ \sigma^- \rangle_{ss} = \eta^2 \frac{g_0^2}{|g_0^2 - \tilde{\Delta}_{ap}\tilde{\Delta}_{cp}|^2}. \quad (1.24)$$

The solution for the intracavity photon number $n_{cav} = \langle \hat{a}^\dagger \hat{a} \rangle$ is of special interest, since $n_{cav}\kappa$ is the rate of photons leaking from the cavity, which the experimenter can detect. In expanded form n_{cav} is

$$n_{cav} = \frac{\eta^2/\kappa^2}{\left(1 + 2C \frac{1}{1+\Delta_{ap}^2/\gamma^2}\right)^2 + \left(\frac{\Delta_{cp}}{\kappa} - 2C \frac{\Delta_{ap}/\gamma}{1+\Delta_{ap}^2/\gamma^2}\right)^2}. \quad (1.25)$$

Interestingly, the same result can be obtained by treating the electromagnetic field in a classical manner. It is in this semiclassical approximation that Lugiato derived his solution [65] in the study of optical bistability.

1.1.4. Analysis of the steady state solution

A number of interesting consequences arise from the steady state solution to this simple system, in particular with respect to the use of the cavity as a single atom detector.

The cavity transmission obtained from the intracavity photon number (equation 1.25) is plotted in figure 1.4 as a function of atom-cavity detuning and laser-cavity detuning, using the parameters of our system. Since our system is in the strong coupling regime ($g_0/2\pi = 240$ MHz, $\kappa/2\pi = 53$ MHz and $\gamma/2\pi = 3$ MHz), the vacuum Rabi splitting is clearly visible when probing the coupled system (right graphs in figure 1.4).

The empty cavity transmission (blue lines) can be obtained from the steady state solution for the intracavity photon number n_e by putting $g_0 = 0$:

$$n_e(\Delta_{cp}) = \langle \hat{a}^\dagger \hat{a} \rangle = \frac{\eta^2}{\kappa^2 + \Delta_{cp}^2} \quad (1.26)$$

This is of course just the Lorentzian with width κ expected for the cavity resonance. By setting $\Delta_{cp} = 0$, we see that the pump term η is given by the intracavity photon number when the empty cavity is resonant to the probe:

$$\eta = \sqrt{n_e \kappa}, \quad (1.27)$$

where we write $n_e = n_e(0)$.

From the spectrum of the coupled system, it is clear that the cavity can act as a detector of single atoms. When probing the cavity resonantly, the transmission strongly changes when an atom is coupled to it. The transmission of the coupled system is only a fraction of the empty cavity transmission:

$$n_{cav}\kappa = \frac{\eta^2\kappa^2}{(1 + 2C)^2} \kappa \approx \frac{n_e}{4C^2} \kappa \quad (1.28)$$

What about the spontaneous emission rate when the system is probed? The spontaneous emission rate Γ_{eff} for an atom coupled to the cavity is calculated from the excited state population as

$$\Gamma_{\text{eff}} = 2\gamma \langle \sigma^+ \sigma^- \rangle_{ss} = \frac{2\gamma\eta^2 g_0^2}{|g_0^2 - \kappa\gamma|^2} \cong \frac{2\gamma\eta^2}{g_0^2} \quad (1.29)$$

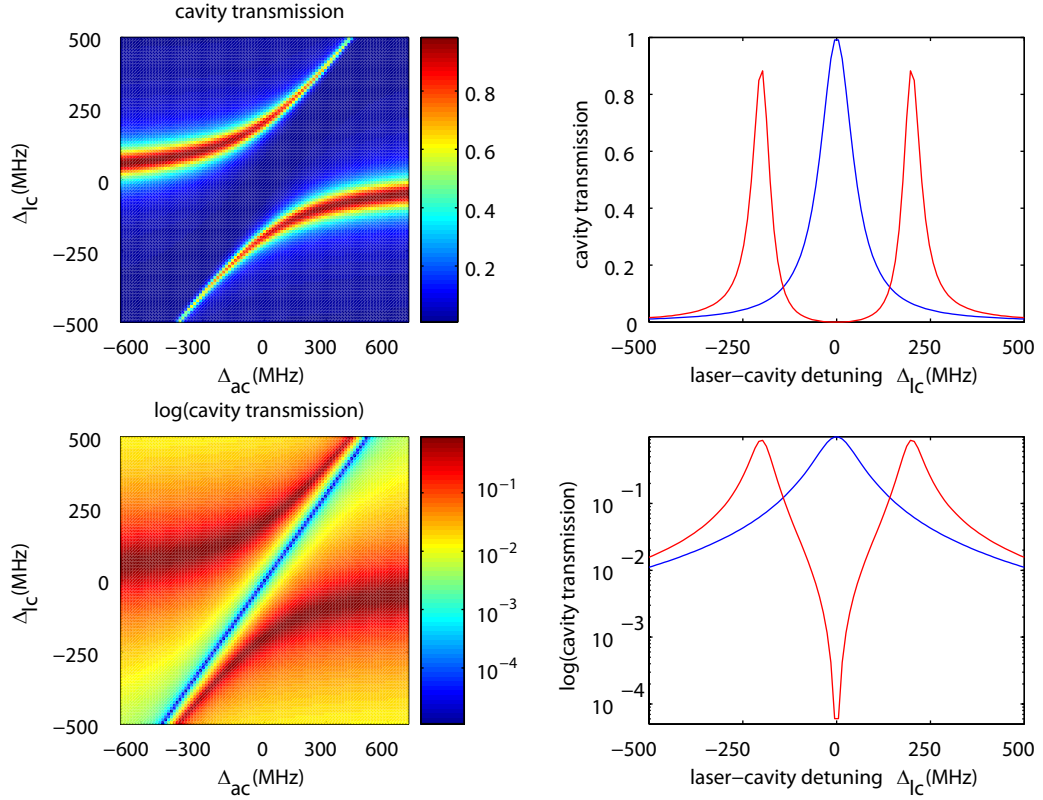


Figure 1.4.: The analytical solution to the master equation of a two-level atom coupled to a single-mode cavity in the weak excitation limit. The upper graphs show the result with a linear scaling, the lower ones with logarithmic scaling. The parameters chosen are those of our system: $g_0/2\pi = 240$ MHz, $\kappa/2\pi = 53$ MHz and $\gamma/2\pi = 3$ MHz. On the two-dimensional plot on the left, both atom-cavity detuning Δ_{ac} (x-Axis) and laser-cavity detuning Δ_{lc} (y-Axis) are scanned. The one-dimensional graphs on the right correspond to a spectroscopy at $\Delta_{ac} = 0$. Blue lines correspond to the empty cavity, the red lines to the coupled atom-cavity system. Compared to the empty cavity, a dramatic decrease in the cavity transmission is observed when probing the coupled system on resonance ($\Delta_{lc} = \Delta_{ac} = 0$).

Since the rate at which pump photons couple to the cavity is η^2/κ , the scattering probability per incoming photon is

$$p_{\text{scat}} = 1/C \quad (1.30)$$

We can conclude that while the transmission of the cavity is strongly reduced due to the presence of an atom, this reduction is not due to spontaneous scattering. Rather, the photons are reflected from the cavity when an atom is coupled to it. In a simple picture, this is due to the cavity resonance being shifted out of resonance due to the vacuum Rabi splitting.

From equation 1.29 also follows the pump rate η_{sat} at which the atom starts to saturate. The excited state population goes as η^2/g_0^2 . To avoid saturating the atom, pump power η^2 should therefore be chosen such that

$$\eta^2/g_0^2 \ll 1. \quad (1.31)$$

In our experiment, we obtain a count rate on the transmission avalanche photo diode of 1×10^6 counts/s for an intracavity photon number of $n_{cav} = 2.5 \times 10^{-2}$. At this empty cavity photon number, which is typical for many of our experiments, condition 1.31 is fulfilled.

A test of the validity of the weak excitation limit was done in [66] by comparing the numerical solution to the master equation to the analytical weak-pumping limit. Condition 1.31 is shown to be correct as far as atomic saturation is concerned. Cavity transmission however increases already at a lower pump power, leading to the more stringent condition

$$\eta^2/g_0^2 \ll 1/C^2. \quad (1.32)$$

1.2. Real-world atoms and cavities

The model discussed so far considered the idealized situation of a two-level atom and a single mode cavity. In this section, we discuss the adaption of this model to our particular situation, where we have to take into account multiple atomic levels and two cavity modes with perpendicular polarizations. Additionally, we use an intracavity dipole trap to trap the atom inside the cavity, leading to state-dependent light shifts. Finally, a magnetic field is applied to the system to avoid mixing between the Zeeman levels of the ground state.

1.2.1. Master equation for many levels and two light modes

All our experiments are performed close to the $F = 2 \rightarrow F' = 3$ transition of the ^{87}Rb D_2 line. The relevant level scheme is shown in figure 1.5 (for a complete ^{87}Rb level scheme, see annexe A.1.2). Even though most of the system dynamics takes place on the $F = 2 \rightarrow F' = 3$ transition, we can not neglect the other excited hyperfine states. The hyperfine splitting here are 267 MHz (between $F' = 3$ and $F' = 2$) and 157 MHz (between $F' = 2$ and $F' = 1$). The coupling strength g between the levels is on the same order, leading to the excitation of all hyperfine states in the $5^2P_{3/2}$ multiplet (with the exception of $F' = 0$, which has no allowed transitions to $F' = 2$). The hyperfine state splitting of the ground state (6.8 GHz) however is much bigger than in the excited state, such that we can neglect the $F = 1$ ground state in our model.

Due to the multiple atomic levels, the Pauli-operator σ^- used in the Jaynes-Cummings model is replaced by the atomic lowering operator \hat{D}_q^- , defined in the usual way as

$$\hat{D}_q^- = \sum_{m_F=-2}^2 \sum_{F'=1}^3 \sum_{m'_F=-F'}^{F'} |F=2, m_F\rangle \langle F=2, m_F | \mu_q | F', m'_F + q \rangle \langle F', m'_F + q |, \quad (1.33)$$

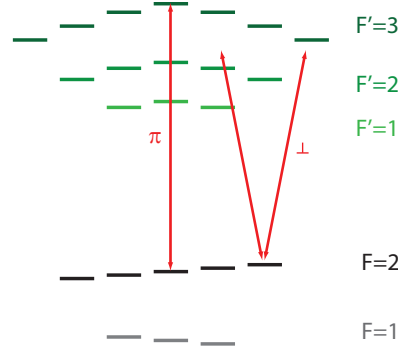


Figure 1.5.: The level scheme of the ^{87}Rb D_2 line as it is taken into account in a full master equation. Since we are interested in experiments near resonant to the $F = 2 \rightarrow F' = 3$ transition, the $F = 1$ ground state is neglected. The effect of a dipole trap is a m_F -state dependent light shift in the excited states. Additionally, a magnetic field is applied to lift the degeneracy of the ground state Zeeman levels. The cavity modes with linear polarizations π and \perp are schematically shown as red arrows. Birefringence in the mirror coatings leads to a different resonance frequency for the two different polarizations.

where $q \in \{-1, 0, 1\}$ and μ_q is the dipole matrix element for σ^-, π, σ^+ transitions, normalized such that for the cycling transition $\langle \mu \rangle = 1$. As in the Jaynes-Cummings model, the atom-field interaction will be approximated to be dipole interactions.

The assumption of a single mode cavity in the Jaynes-Cummings Hamiltonian also does not hold in our case. Our cavity mirrors induce a polarization dependent phase shift on the probe light in the cavity, leading to two polarization TEM₀₀ modes separated by a birefringent splitting of $\Delta_{bi}/2\pi = 540$ MHz. Both polarization modes are linearly polarized. Accordingly, two polarization vectors of unity length ($\vec{\mathcal{E}}_1$ and $\vec{\mathcal{E}}_2$, such that $\vec{\mathcal{E}}_1 \cdot \vec{\mathcal{E}}_2 = 0$) describe the polarization of the intracavity probe light.

The coherent interaction between the light and the cavity in analogy to the Jaynes-Cummings model (taking into account all atomic levels and the two cavity modes) is therefore given by

$$\hat{H}_{int} = g_0 \left(\sum_{i=1,2} \hat{a}_i^\dagger \left(\vec{\mathcal{E}}_i \hat{D}^- \right) + \left(\vec{\mathcal{E}}_i \hat{D}^+ \right) \hat{a}_i \right), \quad (1.34)$$

where \hat{a}_i and \hat{a}_i^\dagger are the destruction and creation operator for the cavity field mode i .

The purely atomic and photonic terms H_{at} and H_{ph} are given, in straightforward generalization and in the frame rotating at ω_p , by

$$H_{at} = \sum_{F'} \sum_{m'_F} \Delta_{HF}(F') |F', m'_F\rangle \langle F', m'_F| \quad (1.35)$$

$$H_{ph} = \sum_{i=1,2} \Delta_{c;ip} \hat{a}_i^\dagger \hat{a}_i \quad (1.36)$$

where Δ_{HF} are the excited states hyperfine splittings and $\Delta_{c,p}$ are the detunings of the two cavity modes to the probe laser frequency.

We use a linearly polarized intracavity dipole trap at 830 nm. For linearly polarized traps, the ground state light shift Δ_{ls} is Zeeman state independent to a very good degree. For the excited states however, the light shift depends on the Zeeman state due to the contribution of higher excited states [67]. Since these light-shifts are larger than the Zeeman shifts, we choose the dipole trap polarization as quantization axis. We can write therefore write the dipole trap contribution to the Hamiltonian as a diagonal term,

$$H_{trap} = \sum_{m_F=-2}^2 \Delta_{ls}(F=2) |F=2, m_F\rangle \langle F=2, m_F| + \quad (1.37)$$

$$\sum_{F'} \sum_{m'_F} \Delta_{ls}(F', m'_F) |F', m'_F\rangle \langle F', m'_F| \quad (1.38)$$

The calculation of Δ_{ls} is done in the usual way [68]. The depth of the ground state trapping potential Δ_{ls} is between 2 MHz and 60 MHz in our experiment.

To lift the Zeeman state degeneracy of the $F=2$ ground state, we apply a bias magnetic field on the order of typically 1 G. The magnetic field leads to a Zeeman state dependent shift of the atomic energy levels when it is oriented along the quantization axis. In general however, its contribution includes off-diagonal terms and is given by

$$H_B = g_{F2} \mu_B \left(\vec{B} \cdot \hat{F}_2 \right) + \sum_{F'=1,2,3} g_{F'} \mu_B \left(\vec{B} \cdot \hat{F}_{F'} \right) \quad (1.39)$$

Here, g_F 's are the g -factors of the hyperfine states, \vec{B} is the magnetic field vector and the components of \hat{F}_F are the angular momentum operators corresponding to angular momentum F .

Finally, we can state the complete, general Hamiltonian for our system in the rotating frame:

$$\begin{aligned} \hat{H}_{full} = & g_0 \left(\sum_{i=1,2} \hat{a}_i^\dagger \left(\vec{\mathcal{E}}^i \hat{D}^- \right) + \left(\vec{\mathcal{E}}^i \hat{D}^+ \right) \hat{a}_i \right) \\ & + \sum_{F'} \sum_{m'_F} [\Delta'_{HF}(F') + \Delta_{ls}(F', m'_F)] |F', m'_F\rangle \langle F', m'_F| + \sum_{i=1,2} \Delta_{c,p} \hat{a}_i^\dagger \hat{a}_i \\ & + g_{F2} \mu_B \left(\vec{B} \cdot \hat{F}_2 \right) + \sum_{F'=1,2,3} g_{F'} \mu_B \left(\vec{B} \cdot \hat{F}_{F'} \right) \\ & - i \sum_{i=1,2} \eta_i \left(\hat{a}_i - \hat{a}_i^\dagger \right) \end{aligned} \quad (1.40)$$

Note that we have added pump terms for both polarization modes as a last term. We include the ground state light shift as an offset to Δ_{HF} , such that $\Delta'_{HF} = \Delta_{HF} + \Delta_{ls}(F=2)$.

For the master equation of our system, we need the decoherence terms associated with spontaneous decay. The decoherence due to the two cavity modes is given as a sum of the decay operators of each individual mode:

$$\mathcal{L}_{cav}\rho = \kappa \sum_{i=1,2} \mathcal{D}[\hat{a}_i]\rho. \quad (1.41)$$

For spontaneous emission of the atom, we define the following superoperator:

$$\mathcal{L}_{at}\rho = \gamma \sum_{q=-1,0,1} \mathcal{D}[\hat{D}_q^-]\rho. \quad (1.42)$$

Here, a little care has to be taken. Since we neglect the $F = 1$ ground state in our model (and therefore in the lowering operator \hat{D}_q^-), \mathcal{L}_{at} strictly speaking neglects spontaneous decays into $F = 1$. However, for the experiments discussed in this thesis, both cavity and laser are usually resonant to the $F = 2 \rightarrow F' = 3$. The atomic excitation therefore is dominantly in $F' = 3$, which has no allowed transition to $F = 1$. The approximation of equation 1.42 is therefore justified.

1.2.2. Solution to the full master equation

The full master equation of our system includes 20 atomic levels and two modes of the electromagnetic field with orthogonal polarization. In the weak-pumping limit, we can restrict the population of the light modes to at most one photon, reducing the size of the system's density matrix.

We numerically calculate the steady-state solution in the weak-pumping limit. For this, the system's density matrix ρ with dimensions 80×80 is written as a vector $\vec{\rho}$ of length 6400. The total Liouville operator \mathcal{L} is written in matrix form as L with dimensions 6400×6400 . In this form, the time evolution of the system is expressed as a simple linear relationship

$$\frac{d\vec{\rho}}{dt} = L \cdot \vec{\rho}. \quad (1.43)$$

The steady state is the eigenvector ρ_{ss} of L with eigenvalue zero.

Figure 1.6 shows the steady state solution as a function of probe laser frequency. The parameters used are following: Probe light is polarized orthogonally to the dipole trap light. The dipole trap depth is 60 MHz, leading to an excited state light shift of around 30 MHz for the $F' = 3, m'_F = 0$ state. The lower frequency polarization mode of the cavity is resonant to the $F = 2, m_F = 0 \rightarrow F' = 3, m'_F = 0$ atomic resonance frequency. This cavity mode is pumped, at a pump power well below saturation. The pump laser frequency is scanned from -300 MHz to +300 MHz with respect to the $F = 2, m_F = 0 \rightarrow F' = 3, m'_F = 0$ atomic resonance frequency. A bias magnetic field of 3.7 G is applied in different directions. These are the same parameters we later use for atomic state detection.

Both the cavity transmission (figure 1.6 a and b) and atomic state populations (c and d) are plotted. A relatively complex spectrum results in the cavity transmission. Due to

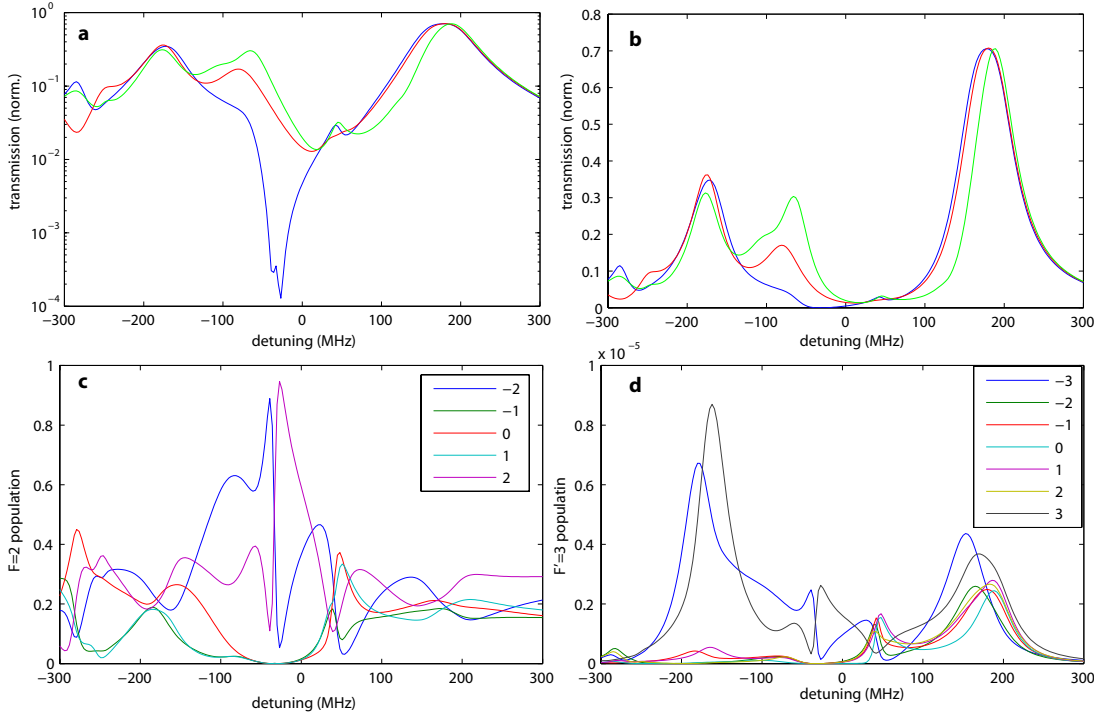


Figure 1.6.: The solution of the full master equation as a function of probe laser detuning for $\sigma^+ + \sigma^-$ probe light polarization. Plotted in a) and b) is the cavity transmission (in logarithmic scale in a and linear scale in b). The color of the curves correspond to different magnetic field orientations: blue is along the quantization axis z , green is along the cavity axis x , and red is perpendicular to both z and x . In panels c) and d), the atomic state populations in the different Zeeman sublevels of $F = 2$ and $F' = 3$ are plotted. For these curves, the magnetic field is oriented along z . The pump rate is $\eta = \kappa\sqrt{3} \times 10^{-5}$. All other parameters are described in the text.

the different atomic levels, a variety of local transmission peak arise, in contrast to the normal vacuum Rabi splitting. The different magnetic field orientations (blue, red and green curves in figure 1.6 a and b) has an important influence and cavity transmission, since it leads to a redistribution of population in the different m_F levels when it is not parallel to the dipole trap polarization.

Only when the magnetic field is parallel to the dipole trap polarization (blue curve in figure 1.6 a and b, and all curves in c and d), the minimum transmission drops to a very low value of 10^{-4} . At the probe laser detuning where this happens (-27 MHz), the $F = 2, m_F \pm 2 \rightarrow F' = 3, m'_F \pm 3$ cycling transitions are resonant to the probe light. The light therefore predominantly drives these cycling transitions, and the atom is pumped into the $F = 2, m_F \pm 2$ ground states, as can be seen in panels c) and d). It can be seen that at this detuning, only the stretched state of the $F = 2$ and $F' = 3$ levels are populated. Since the system is largely symmetric with respects to m_F states (except

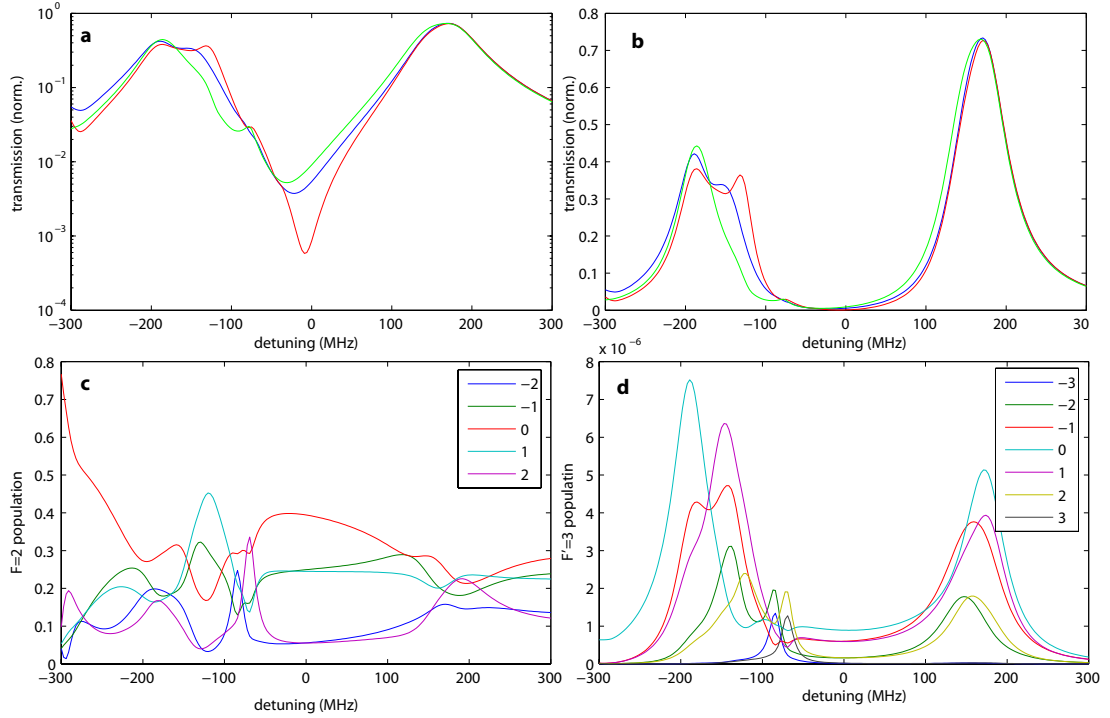


Figure 1.7.: The solution of the full master equation as a function of probe laser detuning for π polarized probe light. Plotted in a) and b) is the cavity transmission (in logarithmic scale in a) and linear scale in b). The color of the curves correspond to different magnetic field orientations: blue is along the quantization axis z , green is along the cavity axis x , and red is perpendicular to both z and x . In panels c) and d), the atomic state populations in the different Zeeman sublevels of $F = 2$ and $F' = 3$ are plotted. For these curves, the magnetic field is oriented along z . The pump rate is $\eta = \kappa\sqrt{3} \times 10^{-5}$. All other parameters are described in the text.

for the Zeeman shifts), the system behaves very similarly to a two-level system in this situation.

Figure 1.6 shows the steady state solution for π -polarized probe light. Here, Probe light is polarized parallel to the dipole trap light, and the higher frequency polarization mode of the cavity is resonant to the $F = 2, m_F = 0 \rightarrow F' = 3, m'_F = 0$ atomic resonance frequency. This cavity mode is pumped. The other parameters are the same as for the previous results. For this parameters, the minimum transmission is higher than for $\sigma^+ + \sigma^-$ probe light. The populations of the Zeeman sublevels in $F = 2$ and $F' = 3$ are markedly different, with in general less population in the $m_F = \pm 2$ resp. $m'_F = \pm 3$ states.

1.3. Conclusion

In this chapter, the basic theoretical formalism necessary for the theoretical understanding of our atom-cavity system was presented. The results obtained from the simple model of a two-level atom and a single-mode cavity show the potential of the cavity to act as a single atom detector that is able to largely avoid scattering. When modifying this model to take into account the level structure of ^{87}Rb and the two modes of our cavity, the behavior of the system becomes more complex. Therefore, it is important to carefully choose the correct set of parameters (probe light polarization, detuning, magnetic field orientation) to obtain the optimum signal for the desired application.

2. Setup

This chapter is devoted to the presentation of the experimental apparatus. The goal of the description provided here is to give a complete overview of setup. The vacuum chamber and the atom chip are briefly described, and the fiber-based cavity is introduced. The laser systems necessary for atom cooling and cavity stabilization and probing are described. Special care is taken to present an outline of the locking schemes necessary for the length stabilization of the science cavity.

2.1. Overview

At the heart of the experimental setup is a high-finesse, fiber based Fabry-Pérot (FFP) cavity [58, 69]. The primary aim of the setup is to provide an ensemble of trapped ultracold atoms well controlled spatially, and to couple them to the FFP cavity. To optimize coupling, the atoms need to be positioned at an antinode of the cavity mode. Figure 2.1 gives a schematic overview of how this aim is achieved. A MOT and an optical molasses are used to trap and pre-cool a large number of atoms. The atoms are then transferred into a magnetic trap created by the atom chip. The atoms are magnetically transported to the chip region where the cavity is positioned. Here, evaporative cooling in a strongly confining magnetic trap is employed to achieve Bose-Einstein condensation. After an optional phase of surface evaporation, the BEC is positioned at the exact center of the cavity mode, and an intracavity dipole trap is ramped up to trap the atoms inside the cavity. The atom-cavity system can now be investigated at will. The following sections provide more details on each of the experimental steps.

The design and construction of the core of the apparatus goes back a few years and is documented in [70]. A number of changes and improvements were implemented during the work for this thesis, and most of these changes are described in [66].

2.2. Cold atoms and BEC on an atom chip

2.2.1. Atomchip and magnetic micro traps

The energy of an atom with angular momentum F , magnetic quantum number m_F and g-factor g in a magnetic field is given by $E(m_F) = g\mu_B m_F B$, where μ_B is the Bohr magneton. Particles in states for which $gm_F > 0$ experience a force towards magnetic field minima. Atoms in such low-field seeking states can therefore be trapped in magnetic field distributions with a minimum (Maxwell's equations do not allow maxima of the magnetic field in free space [71]). Traditionally, arrangements of coils have been (and are

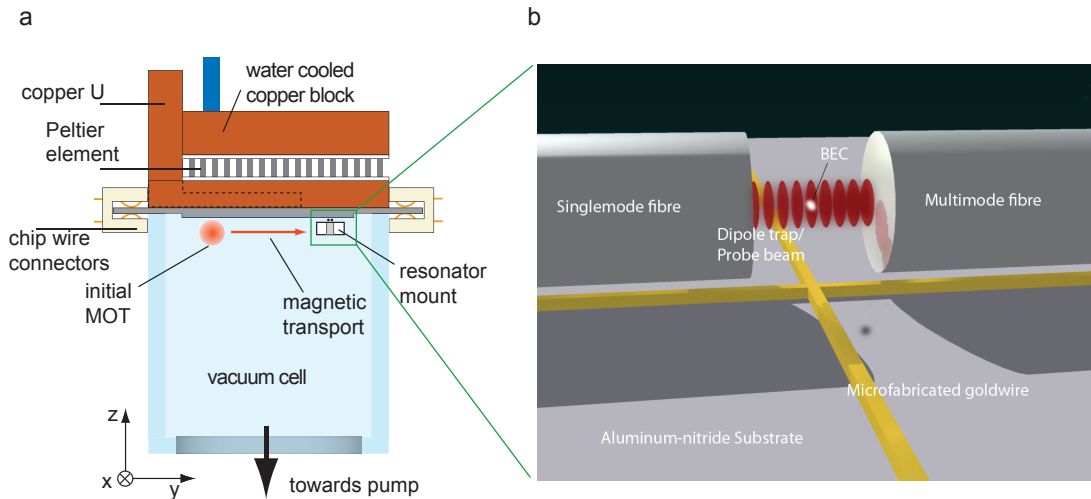


Figure 2.1.: A schematic overview of the experimental vacuum chamber. Panel a) shows the glass cell from the side, with the atom chip glued onto the top. Active cooling is used for the atom chip. A mirror MOT extracts atoms from the background gas. The trapped atoms are transferred to a magnetic trap and transported towards the resonator, where a BEC is obtained by evaporative cooling. Panel b) shows a sketch of the high-finesse resonator above the atom chip (in the experiment, the resonator is below the atom chip). The BEC is loaded into an intracavity dipole trap. The cavity is probed by a pump laser through the single-mode fiber. Panel a) adapted from [70]

being) used to create magnetic traps [72]. This approach, while successfully employed in many experiments, allows a limited range of geometries and control over the magnetic traps. Atom chips present some advantages in this regard.

An atom chip [73–75] uses a combination of microfabricated wires and macroscopic coils to generate magnetic field distributions well suited for trapping atoms. The use of standard microfabrication methods allows the generation of relatively complex wire configurations and therefore enables the creation of a large variety of magnetic potentials. The small structure size of the current carrying structures results in the possibility of microstructuring the magnetic field [76] and gives the experimenter high-precision control of the position of the magnetic trap, with a resolution much better than optical wavelengths.

Our atom chip

Our atom chip is constituted of a basis chip and a science chip glued together with a vacuum compatible epoxy glue. Both layers are shown in figure 2.2. The basis chip contains wire structures with a typical width of 0.2 mm - 1 mm and a thickness of 7 μm .

It is glued on top of the glass cell, thereby closing the experiment chamber. PCI-connectors are used to connect the 48 contacts of the basis chip. 12 of these contacts connect wires directly on the basis chip, whereas the remaining contacts are used to connect the science chip via bonding wires. The science layer is glued onto the basis

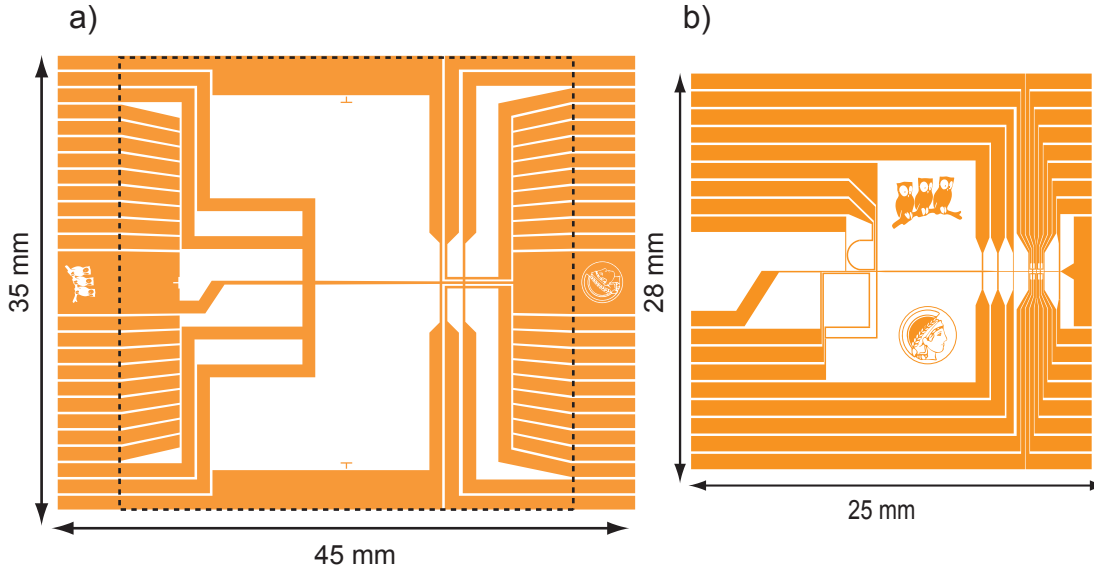


Figure 2.2.: a) The basis chip, which covers the glass cell. b) The science chip which is glued onto the basic chip.

layer. It is smaller and lies entirely within the vacuum chamber. This chip contains a large number of wires that can be connected individually using any of 34 contacts. The wire structures on the science layer typically have a width of at least $50 \mu\text{m}$ and a thickness of $7 \mu\text{m}$. A dielectric mirror covers the surface of the science chip. It is separated from the microwires by a layer of epoxy glue of about $10 \mu\text{m}$ thickness.

A macroscopic U-shaped copper wire is placed on top of the basis substrate, outside the vacuum chamber. A current of $\sim 60 \text{ A}$ through the copper U generates the quadrupole magnetic field for the initial MOT. The copper-U is inside a block of copper which covers the backside of the basis chip. A Peltier element on top of this copper block actively stabilizes the atom chip temperature. The heat extracted by the Peltier is removed by a second copper block which is water-cooled.

2.2.2. Vacuum apparatus

The vacuum apparatus consists of the experiment chamber, a Rubidium dispenser and an ion getter pump. The geometry of the setup is shown in figure 2.3. The chamber itself is formed by a cubic glass cell of dimensions $30 \text{ mm} \times 30 \text{ mm} \times 30 \text{ mm}$, onto the top of which the atom chip is glued. The opposite side of the cube has a hole of 27 mm diameter. Epoxy glue was used to connect a glass-metal transition to the cube via this hole. The feedthroughs for both the optical fibers that form the FFP-cavities as well as

the wires contacting the cavity piezo elements were realized by cutting grooves into two opposing walls of the cubic glass cell. The epoxy glue used to glue the atom chip to the cell also seals these feedthrough grooves. A 25l ion getter pump maintains the vacuum

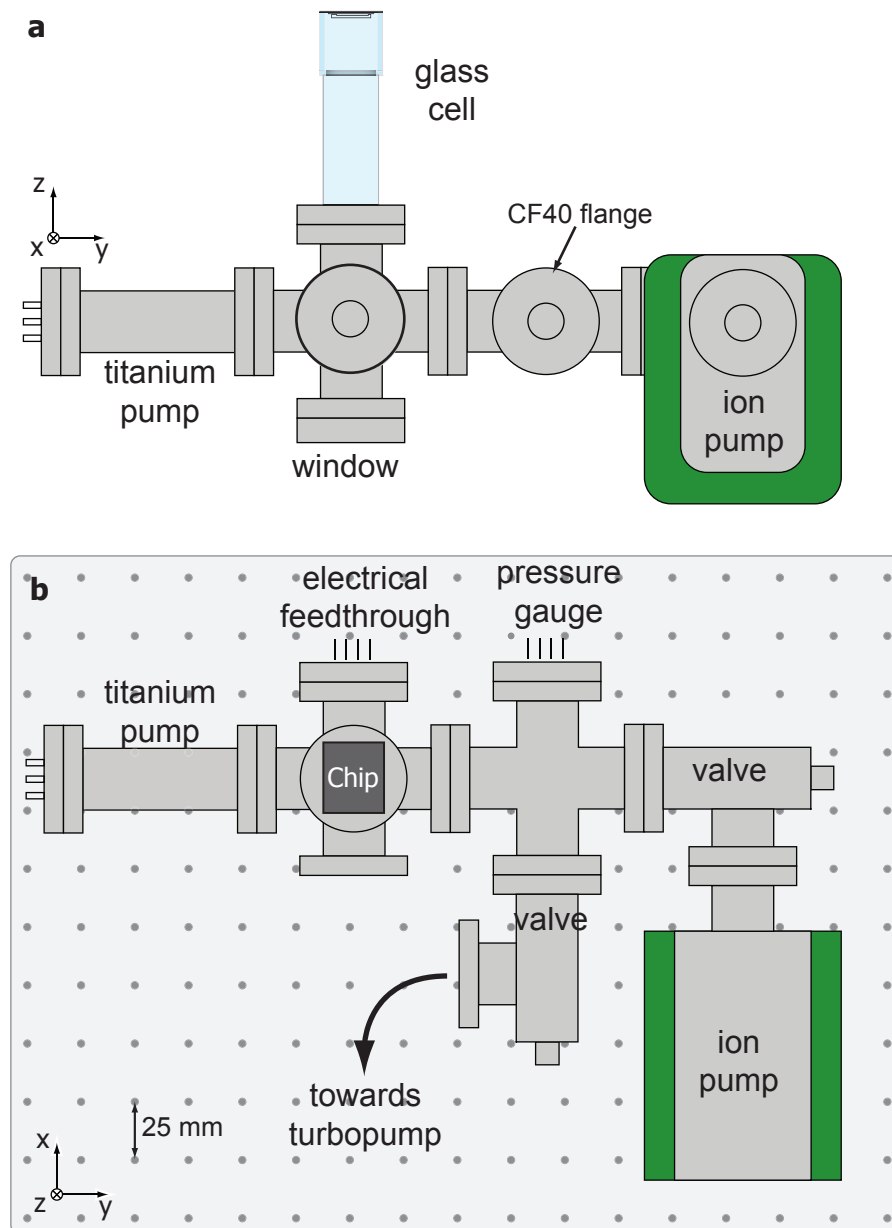


Figure 2.3.: Sketch of the vacuum apparatus. a) side view b) top view. The glass cell is used together with standard ultra-high vacuum components: One six-way cross, one four-way cross, an ion pump (25l/s), a titanium sublimation pump, a pressure gauge, and six electrical feedthroughs. The windowed flange below the chip gives optical access perpendicular to the chip and is used for a cavity side excitation beam. Adapted from [70].

in the chamber. A titanium sublimation pump can be used to improve the pressure. As source of Rubidium, commercially available dispensers are used and contacted via electrical feedthroughs. The resulting background pressure is around 10^{-9} mbar.

2.2.3. Laser system for cold atoms

The laser system used can be conveniently grouped into two mostly independent subsystems. Three laser diodes are used to laser-cool the atoms, three more are required for the locking and probing of the FFP cavity. The two systems are described independently, the system for laser cooling here, the cavity-related system in chapter 2.3.2.

The level scheme of the ^{87}Rb $D2$ -line is shown in figure 2.4, along with the different frequencies needed for laser cooling. The main cooling laser operates red detuned to the $|F = 2\rangle \rightarrow |F' = 3\rangle$ transition. A repump laser resonant to the $|F = 1\rangle \rightarrow |F' = 2\rangle$ transition prevents pumping into $|F = 1\rangle$. A circularly polarized pump beam resonant to the $|F = 2\rangle \rightarrow |F' = 2\rangle$ transition is used to optically pump the atoms into $|F = 2, m_F = 2\rangle$.

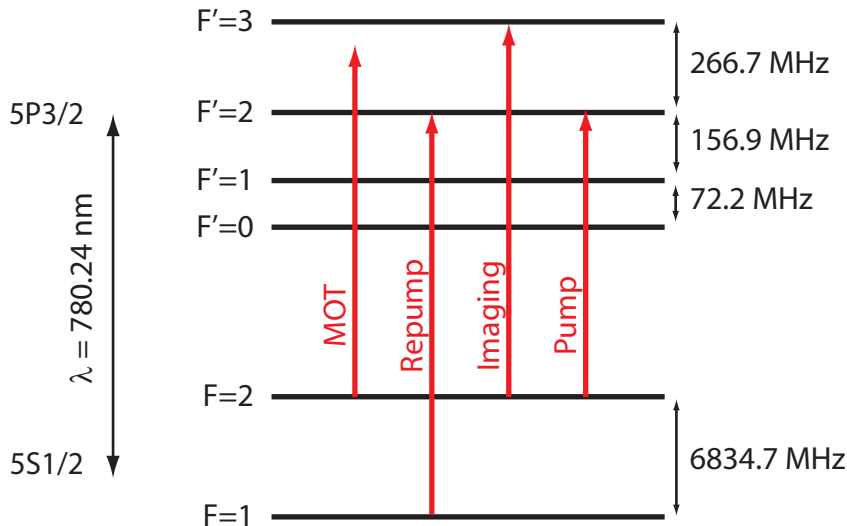


Figure 2.4.: ^{87}Rb Levels used for laser cooling.

The light with the required frequencies is generated by three diode lasers: the master, the slave and the repumper. The optical setup is shown in figure 2.5. Tunable external-cavity diode lasers in the Littrow configuration [77] are used for all but one of the laser sources. Frequency modulation Doppler-free saturation spectroscopy setups [78–80] are used to lock these lasers to well-determined detunings with respect to ^{87}Rb transitions. The slave laser is frequency locked by light injected from the master. In the following section, we describe the complete setup used for the generation the required light fields.

The cooling light is provided by two laser sources in a master-slave setup. The master is locked on the $|F = 2\rangle \rightarrow |F' = 2\rangle$ $|F = 2\rangle \rightarrow |F' = 3\rangle$ cross-over resonance of

an saturated absorption spectroscopy. Part of the light from the master diode injects the slave laser diode. The injection light is frequency shifted by an acousto-optical modulator (AOM) in double pass configuration running at a frequency from 60 MHz to 115 MHz. This allows to bring the frequency of the slave laser to a range of $+2\Gamma$ to -14Γ with respect to the $|F = 2\rangle \rightarrow |F' = 3\rangle$ transition. Most of the slave output is used as MOT cooling light after further frequency shifting by an AOM running at 80 MHz. It is therefore divided into four parts using polarization optics and coupled into the MOT fibers. Since we use a mirror MOT (see section 2.2.4), only four beams are required for the MOT.

The repump laser is locked on the $|F = 1\rangle \rightarrow |F' = 1\rangle$ $|F = 1\rangle \rightarrow |F' = 2\rangle$ cross-over resonance of a saturated absorption spectroscopy. It is frequency shifted by a single-pass AOM operating at 83 MHz, leading to a frequency resonant to the $|F = 1\rangle \rightarrow |F' = 2\rangle$ transition. It is superposed with the 45° MOT beam before fiber coupling.

The light required for the pump beam is obtained from the master laser output. It is frequency shifted in a double-pass AOM configuration running at -67 MHz to make it resonant to the $|F = 2\rangle \rightarrow |F' = 2\rangle$ transition.

Absorption imaging requires light resonant to the $|F = 2\rangle \rightarrow |F' = 3\rangle$ transition. A small portion of the slave beam is separated from the MOT light for imaging. A single-pass AOM at -55 MHz shifts the frequency to the right value. Since there are two spatially separated regions of interest for absorption imaging on the chip (the MOT region and the cavity region), the imaging beam is split into two before being coupled into optical fibers.

2.2.4. The optical setup around the vacuum chamber

There are three groups of optical components around the vacuum chamber (more precisely, around the glass cell), pertaining to three different functions: the MOT beams, two independent imaging systems, and cavity side-excitation beams aligned vertically to the cavity axis. Figure 2.6 shows a picture of the optics around the chamber.

The MOT uses the mirror MOT configuration [73, 81] that only uses four laser beams, two of which are reflected from a dielectric mirror on the chip surface. For absorption imaging, two independent systems are installed. One allows imaging in the region where the MOT is created, the other images the cavity region, where the BEC is created. The two side-excitation beams allow the pumping of atoms coupled to the cavity. One side excitation beam is aligned parallel to the chip surface, the other perpendicular to it (see [66, 70] for details).

2.3. The high-finesse cavity

2.3.1. Introduction

The core of the experiment is the FFP cavity. Just as conventional high-finesse cavities [16, 53, 82], it is formed by two highly reflective, multilayer dielectric mirrors. The

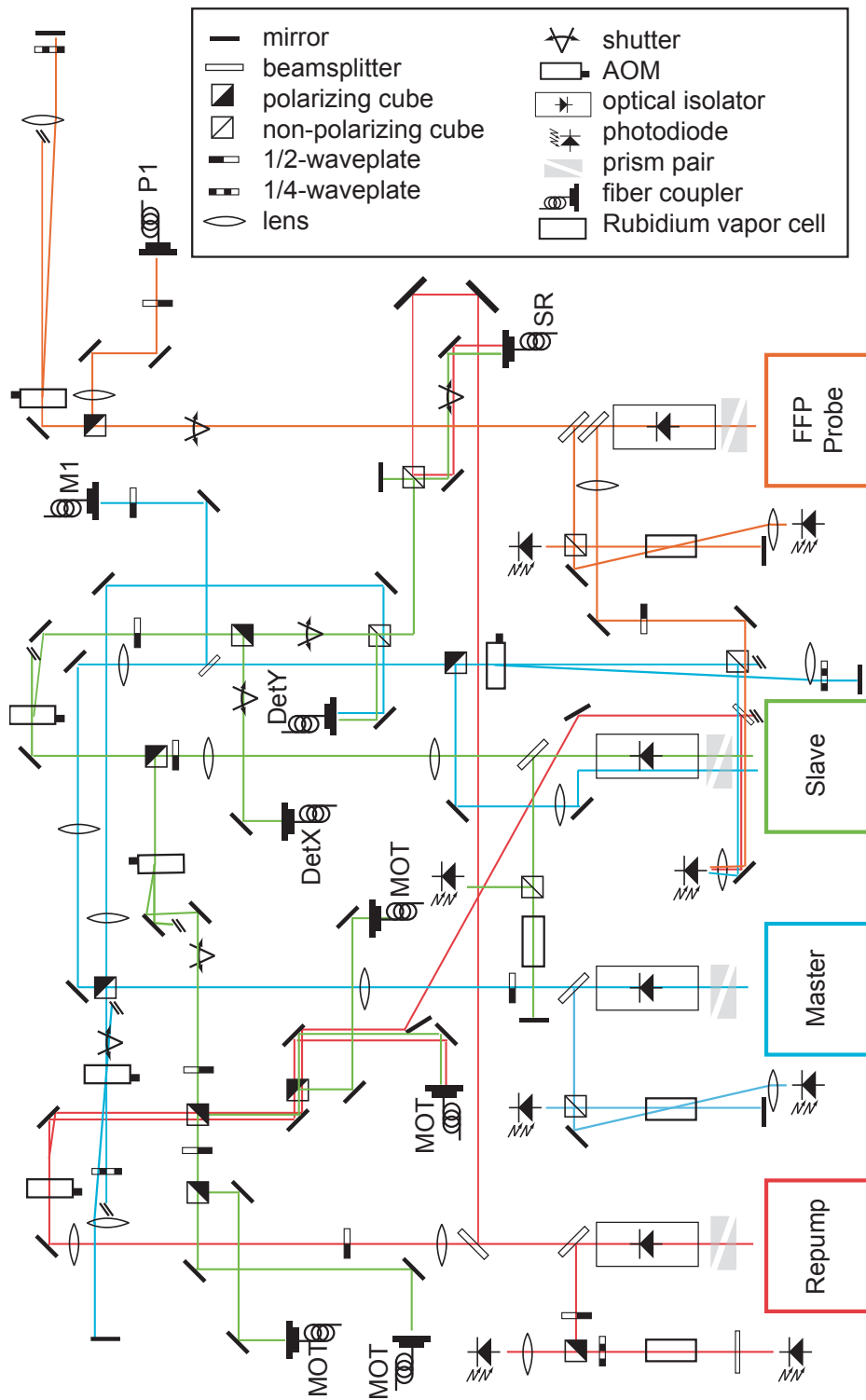


Figure 2.5.: Setup of optical components on the optical table 1, used mainly for the laser cooling setup.

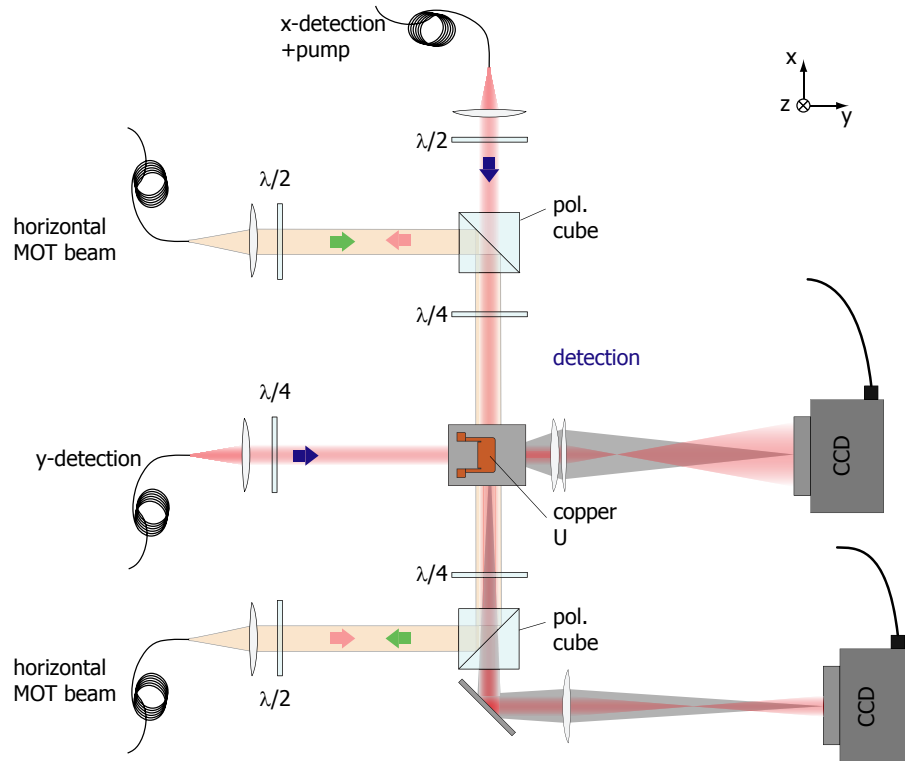


Figure 2.6.: Optical setup around the vacuum chamber in top view. Two of the four mirror MOT beams are shown. The additional two are directed at a 45° towards the chip, where they are reflected by a dielectric mirror on the chip surface. Two detection setups allow absorption imaging in the MOT region (y-detection) and in the cavity region (x-detection). Adapted from [70]

FFP cavity however uses the end facets of optical fibers as substrate for the reflective coatings, rather than finely polished blocks of glass. Replacing relatively cumbersome mirror substrates with fibers results in a number of advantages. In particular, cavity probe light is easily accessible since the cavity output is contained in a single mode fiber. Additionally, the fiber design enables relatively easy integrability on an atom chip. The magnetic traps generated by atom chips typically are at a distance of a few tens to hundreds of micrometers from the chip surface, and the trap frequency scales inversely to the chip-trap distance. If one wishes to couple atoms in these traps to a cavity in a well controlled manner, the cavity mode axis should not be more than around $100 \mu\text{m}$ away from the chip surface. Using bulk substrates with diameters on the order of many millimeters, this is only possible when placing the mirrors around the chip rather than on top of it. This however leads to a large cavity length and large cavity mode volume, strongly limiting the atom-cavity coupling strength. The fibers used here have a diameter of $125 \mu\text{m}$, allowing to mount the cavity directly onto the atom chip. Therefore, a FFP system is not subject to these constraints and allows to achieve a very small cavity length. The small cavity length also means that small radii of curvature

can be used for the mirror surfaces¹, reducing the mode waist and enabling even smaller mode volumes.

The fiber based construction of the cavity also makes the system scalable in the sense that many cavities can be mounted next to each other on one and the same single chip. In our setup, there are two cavities parallel to each other.

The production process of the cavities is presented in detail in reference [69], and we only give an overview here. The end facets of two fibers are shaped into a concave structure by CO₂-laser machining. The CO₂-laser is focused on the fiber end facet and a short pulse abruptly heats the fiber endfacet. A combination of evaporation from and material flow on the surface leads to the formation of a concave structure with very low surface roughness (≤ 0.2 nm). The structure shape can be made close to circular. The radius of curvature at the bottom of the structure and the structure size can be fine-tuned by adjusting pulse length, pulse energy, CO₂ laser beam waist and thermal contact between the fiber and its holder. After the CO₂-laser machining, the fiber end facets are coated in a commercial coating facility.

To mount the cavities on the atom chip, V-groove holders are used. Each fiber is glued into one groove of a holder itself glued onto a shear piezo. The piezos allow to adjust the cavity length by approximately $1 \mu\text{m}$ over a voltage range of ± 400 V. No other degree of freedom is adjustable once the fibers are glued to the V-groove. The shear piezos are mounted on a ceramic bridge which is glued to the atom chip at one end. Figure 2.7 shows a picture of the two mounted cavities. The fibers are positioned such that the cavity mode center lies above a crossing of microwires on the chip. A magnetic dimple trap can therefore be generated inside the cavity mode, allowing optimal control over the position and extension of the atomic cloud. A hole in the ceramic bridge enables optical access transversally to the cavity mode along the vertical z-axis.

Cavity parameters

Both cavities in the experiment consist of a non-polarization maintaining single mode fiber used as input port and a multi mode fiber used as output port. The multi mode fiber on the output side was chosen to make alignment of the two fibers forming the cavity less critical. For the experiments described in this thesis, only one cavity (called science cavity) was used for measurements, with the second cavity supporting the cavity lock (see chapter 2.3.2).

Table 2.1 lists the most important cavity parameters for both cavities. The science cavity has mirrors with radii of curvature of $450 \mu\text{m}$ on the single mode fiber and $150 \mu\text{m}$ on the multimode fiber. Note that these radii are estimates based on profilometer measurements and are prone to errors. They are of importance especially in their role of defining the cavity mode volume, and therefore g_0 . The coupling constant $g_0/2\pi = 240$ MHz given in the table however is the measured g_0 (see chapter 3.5).

¹For symmetric cavities, the region of stable configurations is given by $\infty < r < d/2$, where r is the radius of curvature of the mirrors and d the cavity length [83].

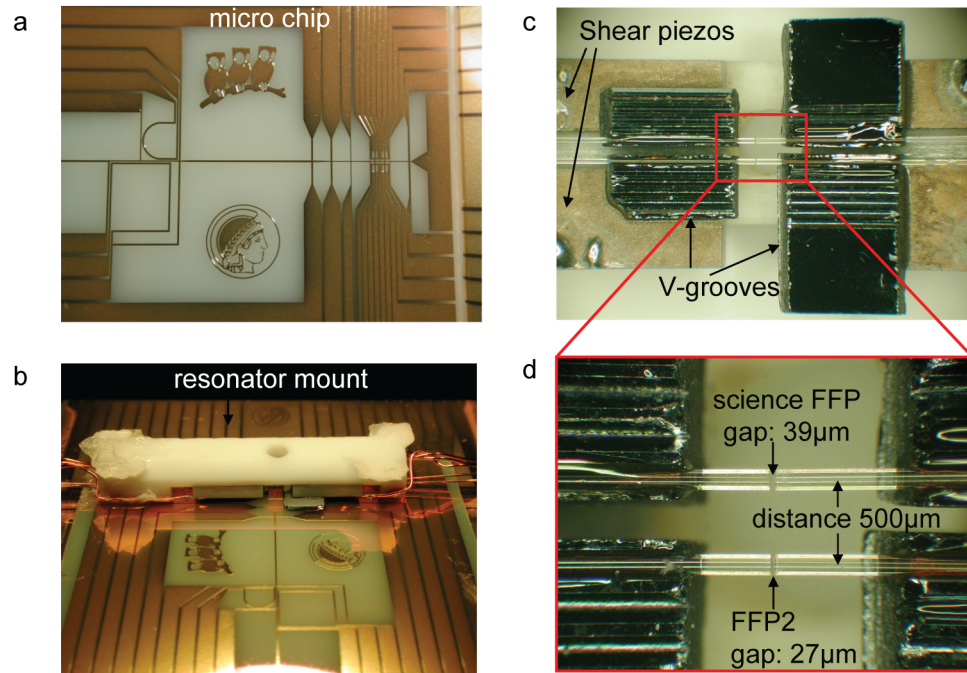


Figure 2.7.: Photographs of the atom chip and the fiber cavities. a) The science layer of the atom chip. b) The chip with mounted cavities. The cavities are between the ceramic bridge and the chip. The hole in the ceramic bridge enables optical access perpendicular to the chip surface. Electrical wires contacting the cavity piezos can be seen. c) Top-view of the fiber cavities mounted on the ceramic bridge, before gluing the bridge to the chip. V-grooves, shear piezos and the optical fibers are shown. d) Close-up view of the cavities.

2.3.2. FFP laser system and locking scheme

The FFP probe laser

The laser used to probe the atom-cavity system needs to fulfill a few specific requirements. A variety of experimental situations call for a flexibility of the locking scheme. The atom-probe detuning $|\Delta_{ap}|$ may vary from zero to up to 60 GHz depending on the experimental regime. Also, the atomic reference frequency might be any transition of the D2 multiplet starting in either $|F = 1\rangle$ or $|F = 2\rangle$, separated by 6.8 GHz. Little power is required, typically on the order of picowatts. A laser diode with antireflection coating in a setup identical to the master and repump laser sources is used. Frequency locking is achieved with a beat lock, in which a beam picked up from either the repump or master beam is used as reference. A chain of voltage controlled oscillators (VCO) and mixers allow detunings from either repump or master frequency of up to 4 GHz. After the double pass AOM, the beam is coupled into an optical fiber. The beam is coupled out of the fiber on the second optical table and frequency shifted in a single pass AOM. It then passes an optional neutral density filter before being coupled to the optical fiber

resonator parameter	science cavity	auxiliary cavity
r_1 : radius of curvature single mode fiber	450 μm	350 μm
r_2 : radius of curvature multi mode fiber	150 μm	97 μm
d: effective resonator length	39.01 μm	$\approx 27 \mu\text{m}$
parameters for 780 nm		
FWHM	106 MHz	156 MHz
F : finesse	38000	35600
Δ_{bi} : birefringent mode splitting	540 MHz	730 MHz
T: mirror transmission	31×10^{-6}	31×10^{-6}
L: mirror losses	56×10^{-6}	56×10^{-6}
T_0 : total transmission	7.5%	n.a.
R_0 : total reflection	42%	n.a.
n_{780} : longitudinal mode number	100	n.a.
ω_0 : mode waist	3.48 μm	3.18 μm
$\kappa/2\pi$: decay constant	53 MHz	78 MHz
$g_0/2\pi$: coupling constant	240 MHz	313 MHz
C_0 : cooperativity	181	210
parameters for 830 nm		
FWHM	260 MHz	390 MHz
Finesse	14000	13100
n_{830} : longitudinal mode number	94	n.a.

Table 2.1.: Parameters of both the science fiber Fabry-Perot cavity and the auxiliary FFP cavity

connected to the main experimental table.

For experiments in which a large detuning larger than the 4 GHz enabled by the offset lock is required, the fiber after the double pass AOM can easily be replaced by a fiber integrated electro-optical modulator (EOM). This allows phase-modulation of up to 20 GHz, with a significant amount of power in the second and third sidebands at 40 GHz and 60 GHz respectively. Using a sideband instead of the carrier as cavity probe allows for experiments with a total detuning of ± 60 GHz.

On the main experimental table, the probe laser is superposed with the dipole trap laser (see figure 2.5) before being coupled into the FFP cavity input fiber. The polarization of the probe is adjusted so as to excite only of the two cavity polarization eigen modes.

Cavity locking chain

The science cavity needs to have a well defined length in order to remain resonant at the same frequency throughout the experimental cycle. An active stabilization of the cavity length is therefore required. The stabilization needs to accommodate some key requirements. It has to be fast enough to correct for vibrational as well as thermal

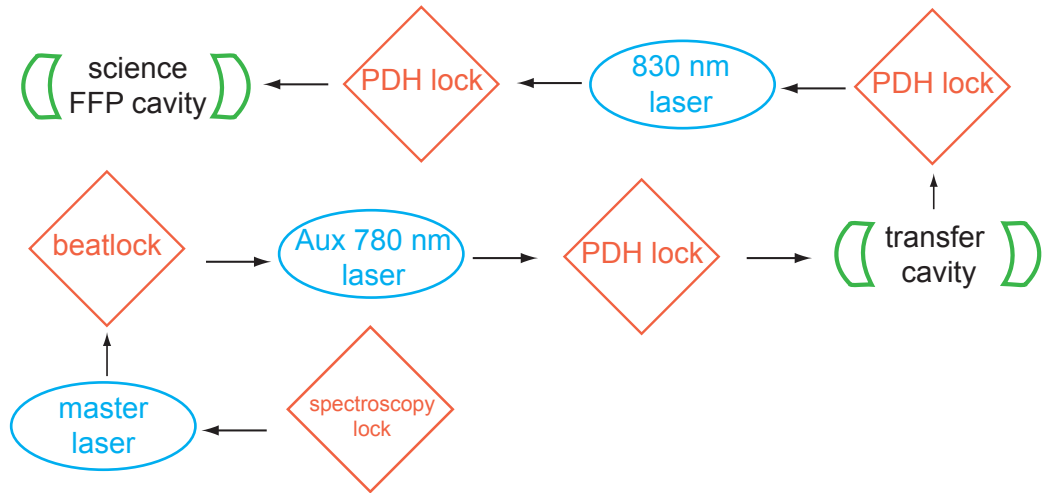


Figure 2.8.: The science cavity lock chain. The science cavity is stabilized using a PDH locking scheme, stabilizing the cavity on a resonance of a TEM_{00} mode of an 830 nm locking laser. The locking laser itself is frequency stabilized on a macroscopic cavity, called transfer cavity, using a PDH setup. The transfer cavity length is stabilized using a third PDH setup which stabilizes the cavity length to be resonant with a 780 nm laser, here called auxiliary laser. This auxiliary laser itself is frequency stabilized using a beat lock setup which stabilizes its frequency at a given offset frequency to the master laser. The master is locked relative to a ^{87}Rb transition.

disturbances. A large range of possible set points is required: the detuning between cavity and atomic resonance can vary from 0 to many tens of gigahertz. The lock point should be independent of the probe laser frequency. Finally, the cavity needs to remain locked throughout the experimental sequence. Figure 2.8 conceptually shows the chain of lock systems implemented to stabilize the science cavity length. The science cavity is stabilized using a Pound-Drever-Hall (PDH) locking scheme, stabilizing the cavity on a resonance of a TEM_{00} mode of the 830 nm locking laser. The laser itself is frequency stabilized on a macroscopic cavity, called transfer cavity, using another PDH setup. Using a third PDH setup, we stabilize the transfer cavity length to be resonant with a 780 nm laser, here called auxiliary laser. This auxiliary laser itself is frequency stabilized to a given offset frequency to the master laser using a beat lock setup. As seen above (page 34), the master is locked relative to a ^{87}Rb transition, thereby giving a fixed frequency anchor to the whole locking chain.

In the following, a more detailed description of this lock chain is given.

Figure 2.9 shows a schematic of the science cavity lock. The main contribution to the lock comes from the 830 nm PDH setup. This scheme is used to lock the cavity length to $d=L_c/2$, where

$$L_c = n_{830}2c\pi/\omega_{830}. \quad (2.1)$$

Here, n_{830} is the longitudinal mode number of the dipole trap laser, and L_c the effective

cavity length. For the implementation of the PDH lock, the locking light at 830 nm is phase modulated at 1.3 GHz by a fiber-integrated EOM, before being coupled to the FFP input fiber. The reflection of the locking light from the cavity is separated from the probe reflection using an interference filter and detected by a fast photodiode². After amplification and demodulation, a PDH error signal is obtained and used as input for a PI-lock with feedback on the science cavity shear piezo.

A second contribution to the science cavity lock comes from the second fiber cavity. Since the two cavities are separated by just 500 μm and mounted on the same ceramic bridge, they are subject to the same thermally induced drifts. This effect is used to enhance the science cavity lock by locking the second fiber cavity and adding the resulting correction signal to the shear piezo of the science cavity.

The lock of the second fiber cavity relies on a mechanism similar to the tilt-locking-scheme [84], where the reflection of a non-TEM₀₀ mode provides a dispersion-like profile. This effect is used to lock the cavity without modulating either the probe frequency or cavity length. To obtain the error signal, it suffices to couple a part of the 830 nm laser to the second cavity input fiber and detect the reflection signal on a photodiode. The resulting error signal is processed in a PI-circuit and the correction signal is fed to both the shear piezo of the second cavity and the science cavity. While the science cavity could be locked by the PDH-lock alone, this additional lock provides some advantages. It leads to an enhanced stability of the science cavity lock; it gives a correction signal even when the locking light in the science cavity has to be switched off (see chapter 2.4.1); and it enables locking when a very shallow intracavity dipole trap (and therefore low locking light power for the science cavity) is required. This last point is important since the lock laser also serves as intracavity dipole trap.

The third contribution to the science cavity lock is used during times in which locking light switched off completely, i.e. before the loading of the intracavity dipole trap (see chapter 2.4.1). Due to the slightly different thermal drifts between the two cavities, the correction signal from the second cavity is not sufficient to keep the science cavity within κ from its lock point for more than a few milliseconds. However, the necessary additional correction to the science cavity shear piezo is identical in each run. A computer generated signal (called feedforward signal) is therefore used to compensate for this drift. With a correctly adjusted feedforward correction, the science cavity does not noticeably drift from its lock point during up to 100 ms even with its PDH-lock completely disabled.

2.3.3. Transfer cavity

The frequency of the locking laser ω_{830} determines the science cavity length as given by equation 2.1. The value for ω_{830} is chosen such that the cavity resonance frequency is at a detuning Δ_{cp} with respect to the TEM₀₀ mode of the probe laser at frequency ω_{780} :

$$L_c = n_{780} 2\pi c / (\omega_{780} - \Delta_{cp}), \quad (2.2)$$

In the special case $\Delta_{cp} = 0$, the cavity is therefore doubly resonant to the locking laser and the probe laser. Equations 2.1 and 2.2 constrain the locking laser frequency to a

²Hamamatsu MSM G4176-03

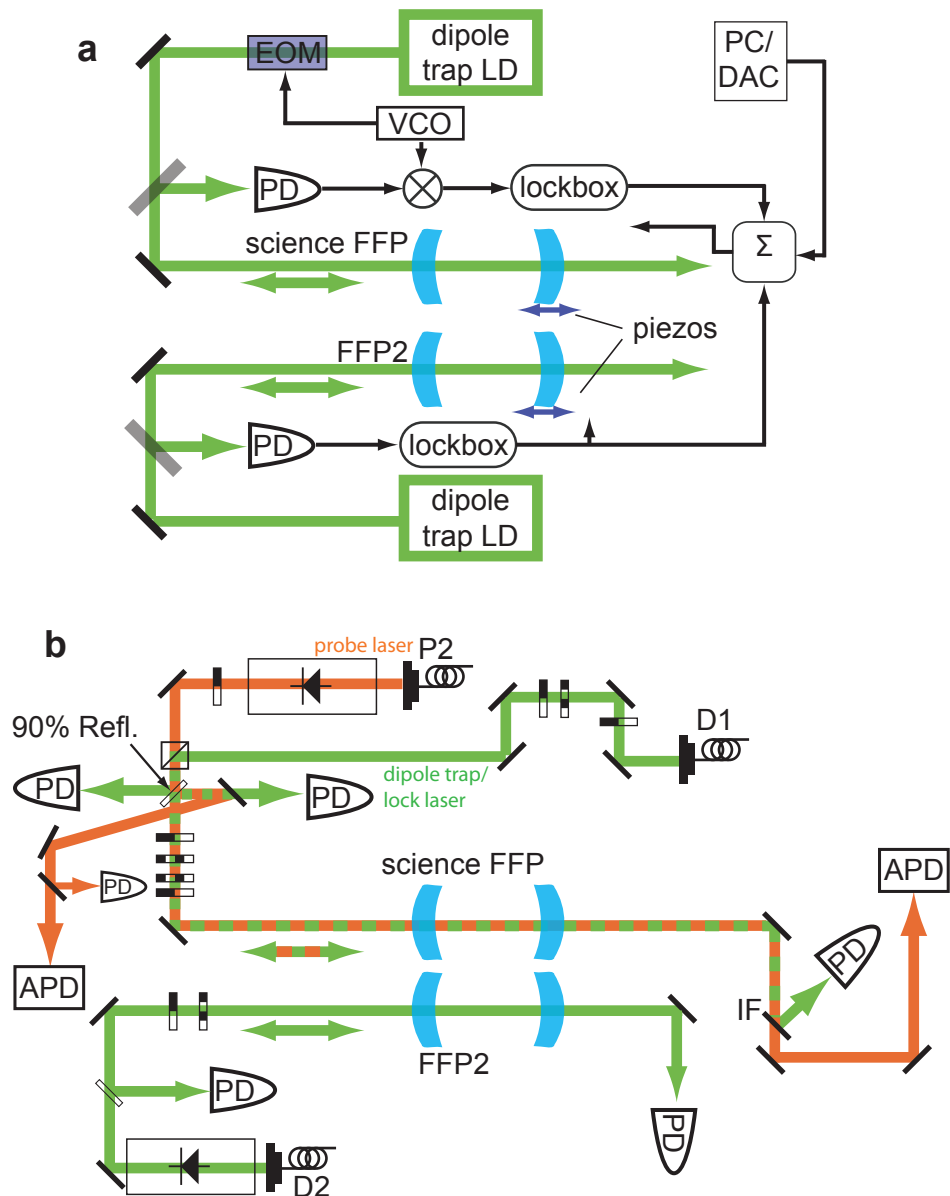


Figure 2.9.: a) Scheme of the components used for the science FFP lock. The three contributions to the feedback on the science FFP are shown: A PDH setup on the science FFP, the correction signal originating from the second FFP as well as the computer generated feedforward. b) The optical setup around the fiber cavities, including the locking laser and the probe laser components. D1, P1 and P2 refer to the optical fiber inputs in figure 2.11

single possible value ω_{830} . The locking laser needs to be stabilized at this frequency. This is achieved by using the transfer cavity as shown in figure 2.10. A part of the 830 nm laser is phase modulated at 17 MHz by an EOM and coupled to the transfer cavity. The reflection from the cavity is recorded on a fast photodiode. The photodiode signal is

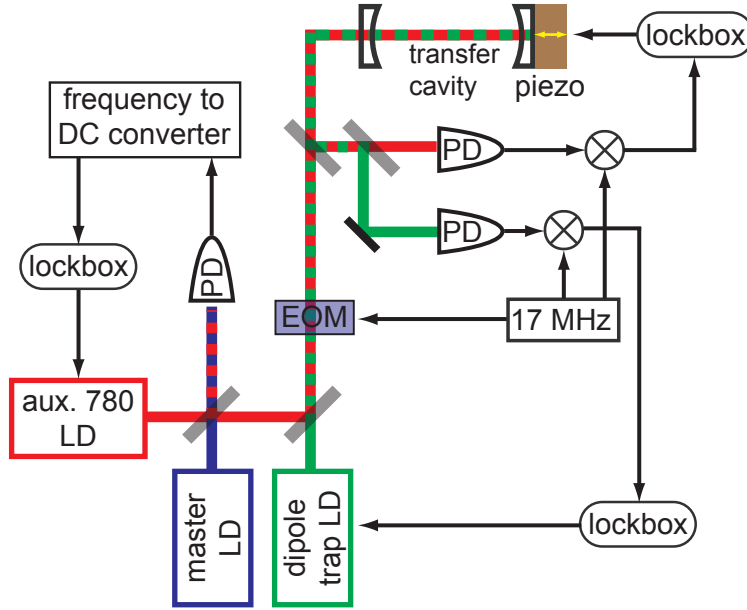


Figure 2.10.: Sketch of the transfer cavity setup. A PDH setup locks the 830 nm laser frequency. The transfer cavity’s length is stabilized on the auxiliary laser frequency, itself locked via a beat lock to the master frequency.

demodulated, resulting in a PDH error signal which is used as input in a PI circuit. The resulting correction signal is fed back to the piezo regulating the external cavity length of the 830 nm diode laser.

To stabilize the transfer cavity length, the auxiliary laser is used. Part of its beam is coupled to the transfer cavity, and its frequency ω_{aux} is chosen such that it is resonant to the cavity. A PDH setup analogous to the one for the 830 nm laser is employed, see figure 2.10. However, the correction signal is fed back not to the auxiliary laser but to the piezo regulating the cavity length.

The auxiliary laser’s frequency is stabilized at ω_{aux} by means of a beat lock. Part of the auxiliary laser beam is superposed with a part of the master laser beam. The resulting beat frequency is converted into a direct current signal by digital electronics³ and used to stabilize the external cavity length of the auxiliary laser via a PI loop.

2.4. Experimental sequence

A dual system is used to control the experimental sequence.. A computer equipped with analog and digital output PCI-cards⁴ controls all standard steps that do not require reaction on feedback from experimental events. Parallel to this system, a dedicated real-

³Home built by the atom chip clock team at SYRTE

⁴PCI-3360 and PCI-4820, from National Instruments

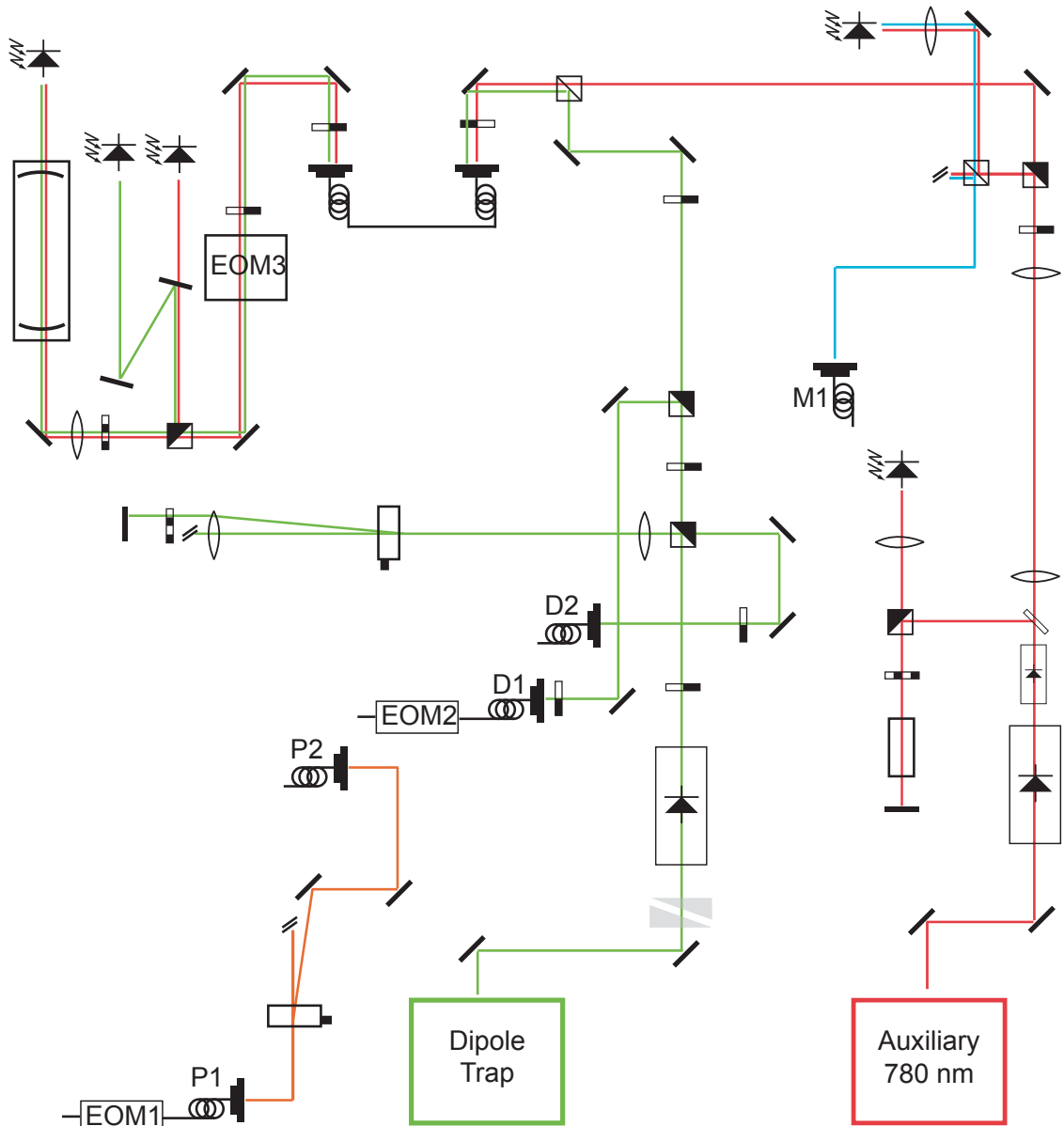


Figure 2.11.: Setup of optical components on the optical table 2, used mainly for the transfer cavity setup.

time system ⁵ controls those part of the experimental sequence that require feedback enabled reactions. In particular, ADWin reads in APD counts during cavity detection phases of each run and proceeds according to a pre-established set of rules depending on the cavity transmission and reflection signals.

⁵Jaeger Electronics, ADWin light

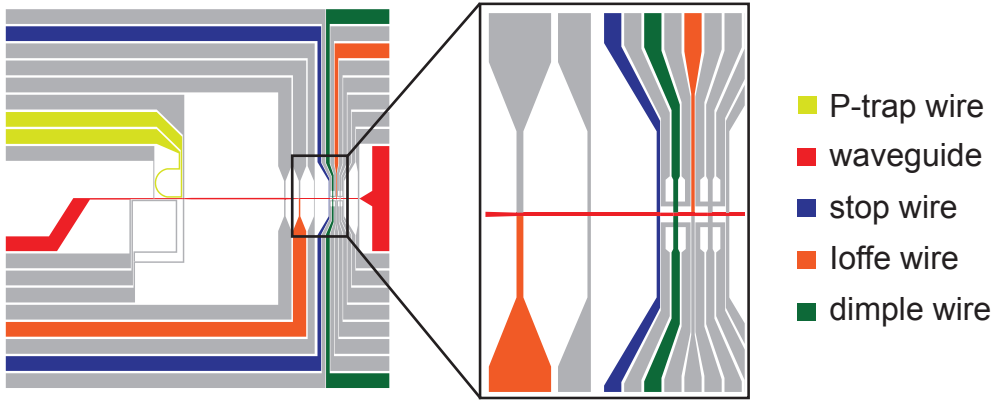


Figure 2.12.: A sketch of important wires on the chip and the names given to them.

2.4.1. From the magneto-optical trap to a BEC in the cavity

All experiments described in this thesis require a sample of ultracold atoms, usually a BEC, as a starting point. A standardized procedure common to all experiments is therefore used for the generation of a BEC. Here, a description of the steps required to obtain the BEC and loading it into the intracavity dipole trap is given. Figure 2.12 gives the names of the most important wires on the chip used during the sequence.

In a first step, atoms are collected, trapped and cooled in a mirror MOT. The MOT quadrupole magnetic field is generated by a current of 57 A through the macroscopic copper U and an external homogeneous magnetic field of $B_y = 9$ G. In a loading time of about 6 s around 2×10^7 atoms are obtained, trapped at a distance of about 4 mm from the chip surface.

The atoms are then transferred into a MOT whose spatially dependent magnetic field is generated by a U-wire of the chip basis layer. A simultaneous ramp of the current through this U (5 A \rightarrow 3.5 A) together with a ramp in the bias magnetic field ($B_y = 2$ G \rightarrow 4.2 G) leads to the compression of the MOT and the approach of the center of the MOT to the chip surface to about 0.8 mm. The temperature of the atoms in this final MOT is 70 μ K.

In the next step, the atomic cloud is cooled below the Doppler temperature using Sisyphus cooling [85] in an optical molasses phase of 3 ms. This step leads to a cloud of typically 1.3×10^7 atoms at a temperature of 14 μ K, as measured by absorption imaging after 10 ms time of flight. After molasses cooling, a short pump pulse of 0.7 ms is used to optically pump the atoms into the low field seeking state $|F = 2; m_F = 2\rangle$. This concludes the laser cooling cycle and the atoms are transferred to the first of a series of magnetic traps. In the following, each of the 12 traps used until the atoms are loaded into the intracavity dipole trap is described.

- Trap 1: For the first magnetic trap, the P-wire (see figure 2.13) on the science layer together with a bias field along the \hat{x} direction is used to generate a magnetic trap whose center precisely overlaps with the position of the atoms in the preceding

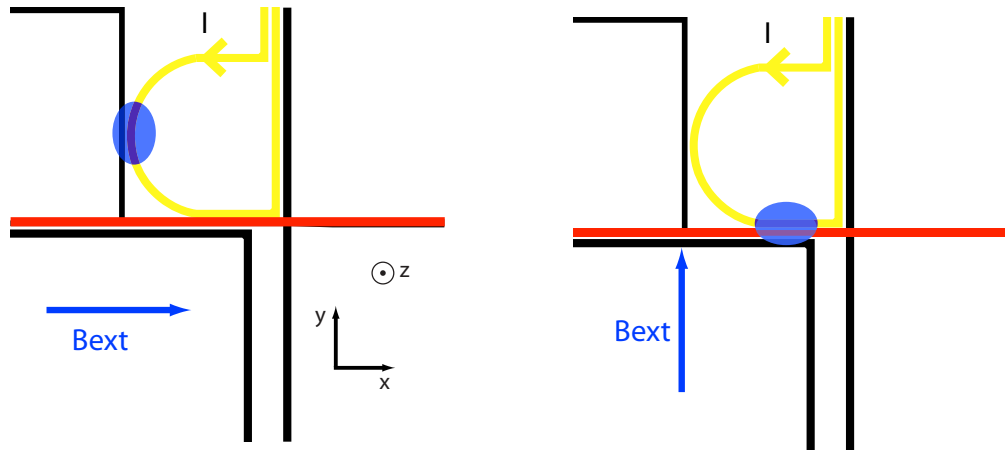


Figure 2.13.: Geometry of the rotatable P-Trap. The position of the atomic cloud is depicted in blue. Adapted from [66]

optical molasses. The transfer efficiency from the optical molasses to this first magnetic trap is over 90%.

- Trap 2: The bias field used in conjunction with the P-wire is continuously rotated from \hat{x} -direction to \hat{y} -direction. The minimum of the magnetic field accordingly moves to the position shown in figure 2.13, directly above the central wire of the science layer of the chip.
- Trap 3: The atoms are transferred to a trap in the form of a waveguide formed by a current through the waveguide wire and a bias field along \hat{y} . The confinement along the x-Axis is provided by an externally generated quadrupole field added to a bias field along \hat{x} .
- Trap 4: To transport the atoms toward the FFP cavity, it suffices to gradually change the bias field B_x , thereby moving the magnetic field minimum along \hat{x} in direction of the cavity. Moving the atoms directly into the FFP-cavity region would lead to collisions with the fibers and consequently atom losses. The transport is therefore stopped at a distance of about 1 mm from the cavity.
- Trap 5: The atoms are transferred to a Z-type trap, with the bias magnetic field along \hat{y} . An additional current through the stopwire (blue in figure 2.12) results in a potential barrier preventing collisions of atoms with the cavity fibers. Traps 5-8 are depicted in figure 2.14.
- Trap 6: Subsequently, the bias field B_y is increased, leading to a steeper trap closer to the chip surface. Simultaneously, a current through the dimple wire along the cavity axis leads to the formation of a second local minimum of the magnetic field, which however is not yet accessible to the atoms due to the barrier generated by the stop wire.

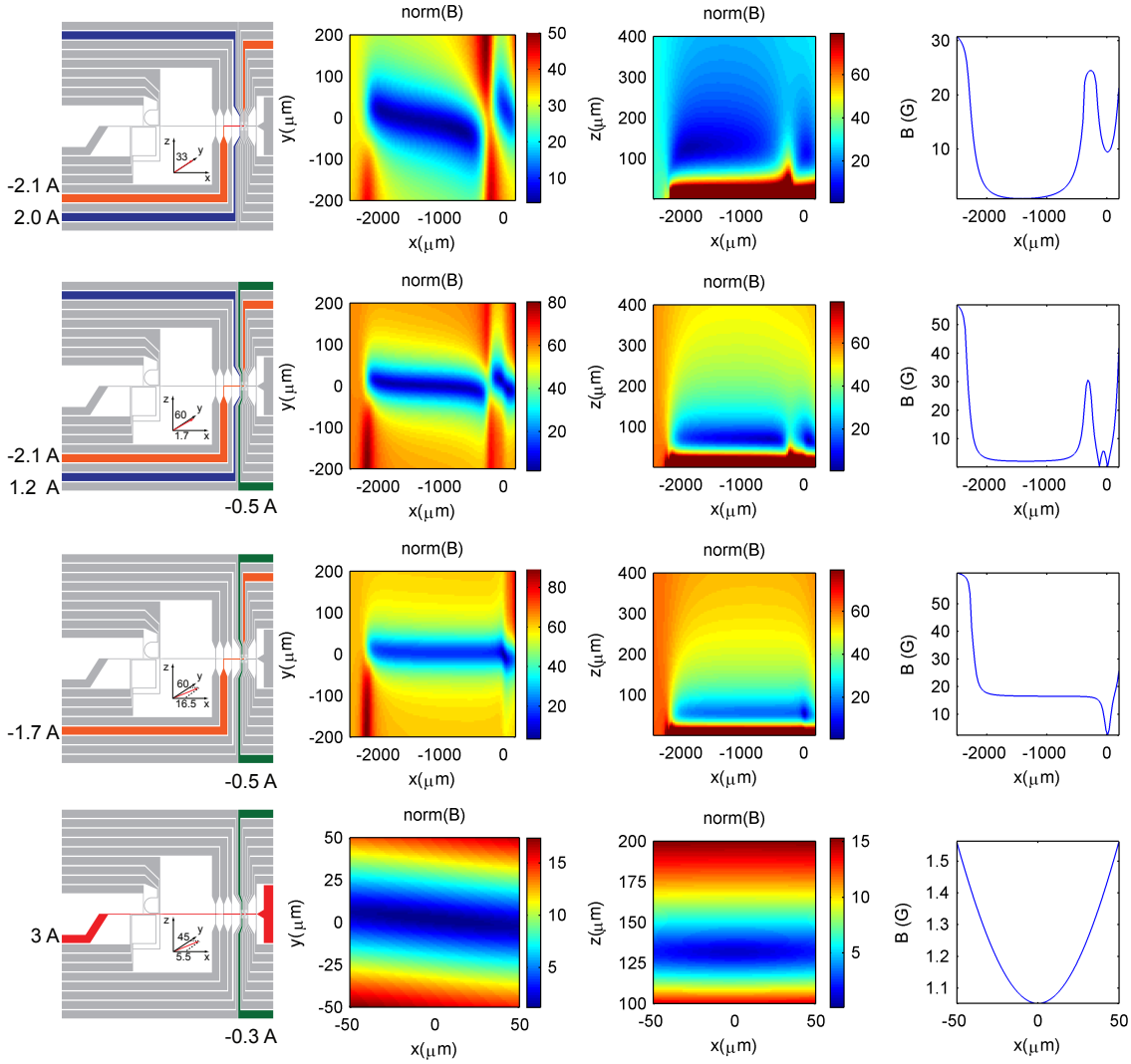


Figure 2.14.: Chip wires and the magnetic traps they create. From top to bottom, trap numbers five to eight are depicted. The insets on the wire configurations (leftmost graphs) give the magnetic bias field (red vector). All magnetic field scales are in Gauss.

- Trap 7: This barrier is now removed by turning off the current through the stop wire. At the same time, radio frequency induced evaporation is applied during about 500 ms, leading to a drastic increase of the phase-space density of the cloud. The dimple trap, just above the cavity, is filled with ultra-low temperature atoms.
- Trap 8: For a second phase of evaporative cooling, the atoms are transferred into a pure dimple trap formed by currents in the waveguide and dimple wires, with a bias field predominantly in \hat{y} direction. The resulting trap is at a calculated distance of $131 \mu\text{m}$ from the chip. Bose-Einstein condensation is achieved with a second step of evaporative cooling (duration: 50 ms), resulting in an almost pure

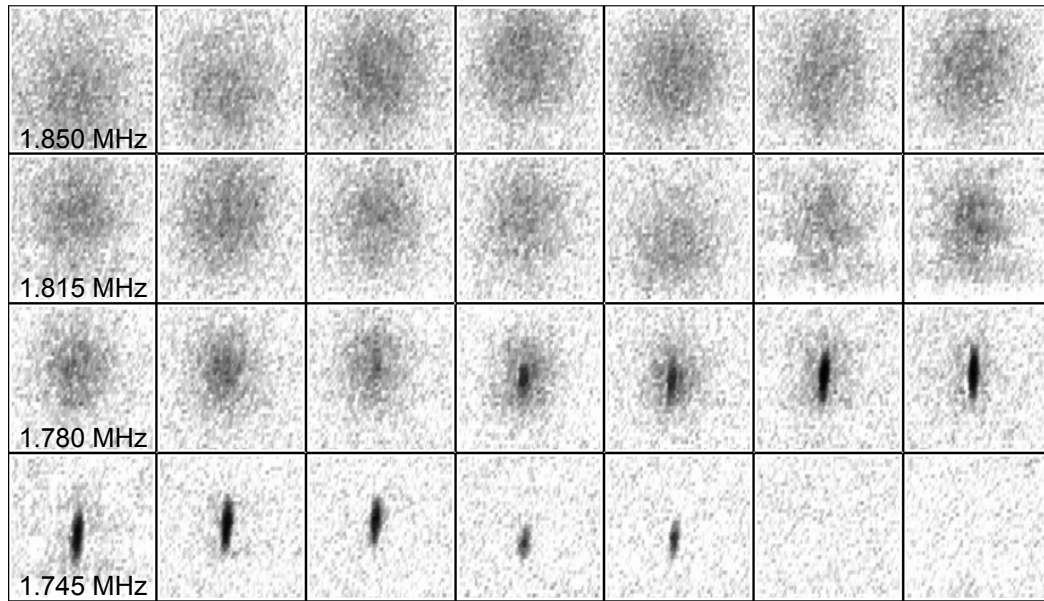


Figure 2.15.: Time of flight images of the atomic cloud after RF-evaporation in trap 8. The final frequency of the evaporation ramp is changed in steps of 5 kHz from the picture in the upper left to the picture in the lower right. The characteristic change from the symmetric expansion of a thermal cloud to the elliptical expansion of a BEC is clearly visible. The population of the ground state can be seen to become macroscopic at an RF-end frequency of about 1.77 MHz. At 1.75 MHz, an almost pure BEC of about 1000 atoms is obtained. Continuing evaporation even further, all atoms are lost at the trap bottom of around 1.725 MHz.

BEC of typically around 1000 atoms (see figure 2.15).

Many of the experiments presented in this thesis require an atom number much smaller than the typical condensed atom number after radio frequency evaporation. An effective way to reduce the atom number without heating is the process of surface evaporation. By bringing the trapped atoms close to the fiber surface, hotter atoms are removed from the trap by surface interactions. It was shown before [70] that this process can be used instead of radio frequency evaporation to obtain a BEC. Similarly, it can be used to reduce the atom number in the BEC. This is done in the next three traps. Surface evaporation is used because it is less sensitive to magnetic field fluctuations than RF-evaporation.

- Trap 9: First, the dimple trap is adiabatically moved closer to the fiber surface.
- Trap 10: In a second step, where the cooling takes place, the trap approaches the fiber surface further until atoms are lost. The resulting atom number can be tuned by changing the final distance between trap minimum and fiber surface.

-
- Trap 11: In the last step, the magnetic trap is positioned at the exact center of the cavity mode. This is the first time the atoms are moved to within the cavity mode. The intracavity dipole trap has to be switched off during this time.
 - Trap 12: In the next and final step of the generic experimental preparation, the atoms are transferred to the intracavity dipole trap. The intracavity dipole trap is ramped up, and all magnetic fields are ramped down. The time constants of both ramps (around 5 ms) are chosen to result in an adiabatic transfer from the magnetic trap to the dipole trap.

3. Coupling single atoms to the cavity

This chapter presents the experimental results concerning the preparation of a single atom trapped at a well-controlled position of maximum coupling to the mode of the cavity. The preparation process is described in detail. The obtained coupled atom-cavity system is characterized. In particular, measurements of the normal-mode spectrum are presented. The spectrum is measured by pumping either the cavity mode or the atom, with consistent results which clearly demonstrate the strong coupling realized in the system.

3.1. Introduction

Coupling of single atoms to high-finesse cavities in the strong-coupling regime requires the positioning of the atom inside a cavity with low mode-volume. In the first successful experiments, this was done by letting atoms fall from a MOT above the cavity [86], or by ejecting them from an atomic fountain below the cavity [53]. Little control over the atomic position inside the resonator was possible in these experiments. More recent experiments use optical conveyor belts to transport single atoms from a MOT to the cavity mode volume [55, 87, 88]. While this method increases the precision of the atom delivery, the positioning along the cavity axis is limited by the beam waist of the standing wave dipole trap and the temperature of the atoms, leading to variations in the coupling strength [67, 89]. Here, we present a single atom preparation in a high-finesse cavity that delivers ultracold single atoms with well-defined coupling to the cavity.

3.2. Coupling of single atoms in a waveguide to the cavity

This section presents results obtained by magnetically guiding atoms through the cavity. The cavity is shown to be well capable of detecting single atoms. Issues related to the imperfectly controlled positioning of the atoms are pointed out and motivate the single-atom preparation introduced in the following sections.

For this experiment, the initial BEC is prepared in a dimple trap at an intersection of two wires 1.25 mm away from the cavity 3.1. From here, the atoms are released into a trap in the shape of a two-dimensional waveguide, oriented perpendicularly to the cavity axis. The magnetic potential in this waveguide provides a steep potential along \hat{y} and \hat{z}

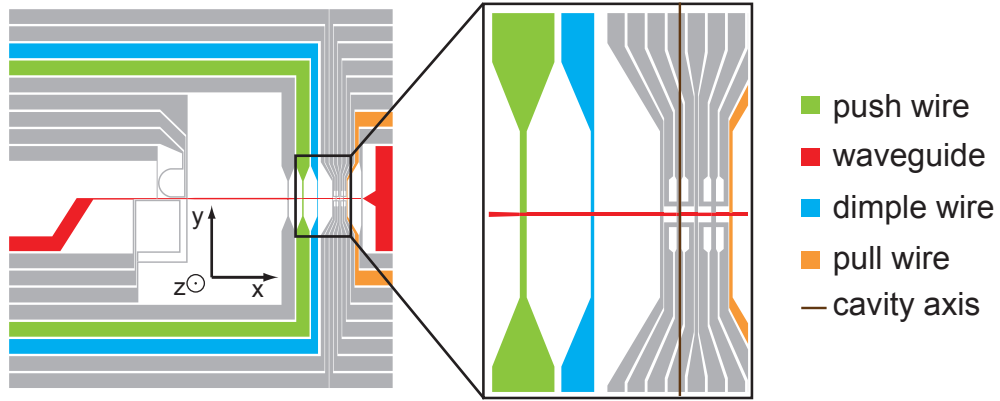


Figure 3.1.: The wires used for the waveguide experiments. The initial BEC is prepared in the dimple trap at the intersection between the waveguide wire and the dimple wire. The push and pull wire respectively create a potential hill and valley, and therefore a potential gradient along \hat{x} , giving a preferred direction for the movement of expansion of the atomic cloud in the waveguide when turning off the dimple trap.

directions, and a weak gradient along \hat{x} lets the atom cloud fly through the center of the cavity mode while continuously expanding. The waveguide trap is created by a current through the waveguide wire together with a bias field along \hat{y} and an offset field along \hat{x} . The small gradient along \hat{x} is created by currents through the push and pull wires (see figure 3.1), creating a potential valley behind the cavity, and a potential hill before it.

The absorption images in figure 3.2 shows the expansion in \hat{x} -direction of a cloud of atoms in the waveguide potential through the cavity. The detection of atoms by the cavity is achieved with a probe laser near-resonant to the atomic frequency $\Delta_{pa} = -7\gamma$. The small negative detuning is chosen to provide an attractive potential for the atoms, such that they are drawn to positions of strong intracavity field and therefore strong coupling. The cavity is locked resonant to the probe laser. Figure 3.3 shows the cavity transmission dips as the atoms fall through the cavity.

A histogram of the cavity transmission during the atomic transit is shown in figure 3.4 a). A maximum of the distribution at 58 counts/ $20\ \mu\text{s}$ corresponds to the empty cavity transmission. A second maximum at 4 counts/ $20\ \mu\text{s}$ is due to the presence of atoms. The count distribution of all counts shows that the two peaks are not clearly separated, due to the finite slope of the dips. We therefore use a threshold-based method to find the distribution of dip minima. The result is shown in figure 3.4 b) in the form of a histogram of the dip depths distribution. Here, a clear difference between the distributions derived from runs with atoms and runs without atoms is visible. Only runs with atoms have dips below 20 counts/ $20\ \mu\text{s}$. The distributions prove that our cavity-based detector can detect single atoms. Using a threshold method, the cavity transmission allows to establish the presence of a single atom in $20\ \mu\text{s}$ with high confidence.

However, it is not straightforward to deduce the detection efficiency of the detector

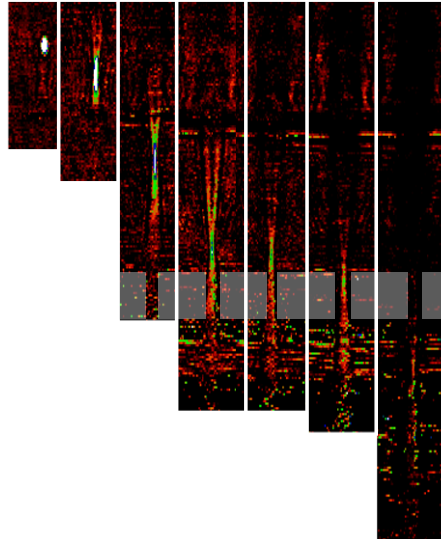


Figure 3.2.: Absorption images of a large cloud of atoms expanding in the waveguide and traversing the cavity mode. The images are taken after a time of expansion increasing from 1 ms for the image at the left to 80 ms for the last image on the left. The position of the optical fibers forming the cavity is shown in shaded gray. Note that the limited depth of field and aberrations of the imaging system leads to the distortion of the shape of the atomic cloud in horizontal direction.

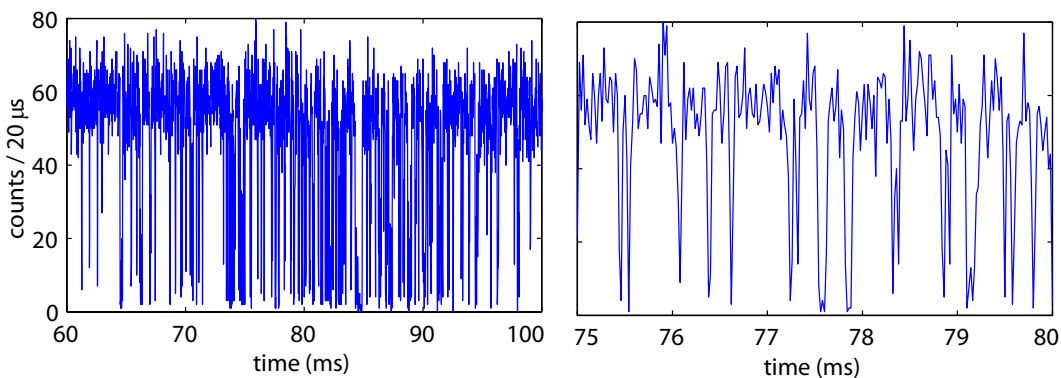


Figure 3.3.: Telegraph signal observed on the cavity transmission when the atomic cloud traverses the cavity mode. To the right, an expanded view of the transit of a few atoms is shown. Clear dips of duration on the order of $100 \mu\text{s}$ and good contrast are visible.

from the distribution. In the strictest sense of the term, the detection efficiency is the fraction of atoms detected among all atoms falling through the cavity. Some atoms might cross the cavity mode at a position of a node of the cavity field, leading to no

visible transmission drop. Furthermore, while entering the cavity mode, atoms start to scatter and have a non-negligible probability to be pumped into the $F = 1$ hyperfine state, a state that is not detected by the cavity transmission, or heated out of the waveguide potential. Furthermore, each single atom might cause several dips. This can happen when it oscillates strongly along the cavity axis while it crosses the cavity mode. Reference [66] investigates all of these effects in detail, and puts a conservative estimate of the detection efficiency at 50%.

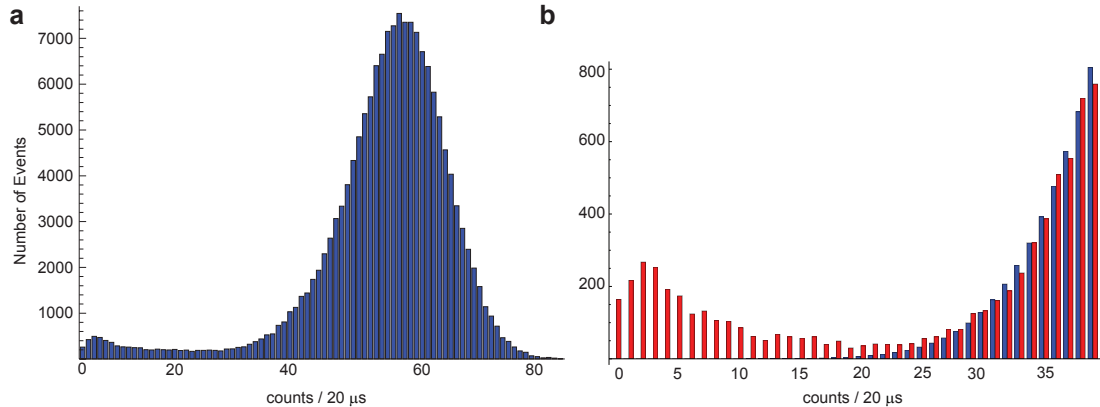


Figure 3.4.: a) Histogram of the cavity transmission during the transit of an atomic cloud. A large poissonian contribution due to the high cavity transmission when no atom is present leads to a large peak around 58 counts/ $20\mu\text{s}$. Atom transits lead to the much smaller peak around 4 counts/ $20\mu\text{s}$. b) A histogram showing the distribution of dip depths of the same experimental traces as used in a). The blue histogram is recorded for an empty cavity, the red histogram is measured with atoms traversing the mode. The histograms are clearly distinct, with a minimum in the distribution at around 20 counts/ $20\mu\text{s}$. This value can be used for the detection of single atoms using a threshold method. Such a method could ascertain the presence of an atom with high certainty.

Despite these problems, we can claim that those atoms that cross the cavity mode at positions that provide strong coupling are detected by our detector. The next sections discuss how we proceed to achieve a better control of the system by trapping single atoms exclusively at positions of strong coupling.

3.3. Microwave based single atom extraction

3.3.1. Heralded preparation of single atoms

The method developed to obtain trapped single atoms strongly coupled to the cavity in our experiment is probabilistic but heralded. The principle of the preparation method is illustrated in figure 3.5. As a starting point to the scheme, a small ensemble of a few

atoms in state $|F = 1, m_F = 1\rangle$ is trapped in the dipole trap at a position of maximum coupling to the cavity. The cavity is resonant to the $|F = 2\rangle \rightarrow |F' = 3\rangle$ transition, such that the few atoms in $F=1$ act as a small dispersive element inside the cavity, with negligible effect on the cavity effective length. A weak MW-pulse resonant to the $|F = 1, m_F = 1\rangle \rightarrow |F = 2, m_F = 0\rangle$ transition is applied. The MW pulse has a single atom transfer probability $p_t \ll 1$. It is followed by a measurement of the cavity transmission by a probe beam resonant to the empty cavity, $\omega_p = \omega_c$. This measurement gives a signal of the internal state of the atoms: High transmission signals that all atoms are in $F = 1$, whereas low transmission signals that at least one atom was transferred to $F = 2$. This sequence of MW-pulse/transmission measurement is repeated until low transmission is observed as shown in figure 3.5 b).

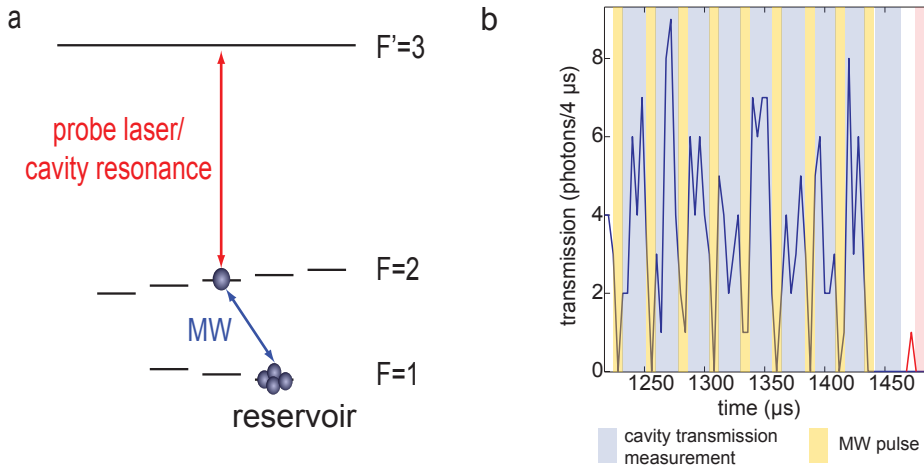


Figure 3.5.: a) Illustration of the single atom preparation method. A weak MW-pulse is applied to a small reservoir of atoms in $|F = 1, m_F = 1\rangle$ coupled to the cavity. The cavity transmission is then probed with the probe laser frequency resonant to the empty cavity, itself resonant to the $|F = 1, m_F = 1\rangle \rightarrow |F = 2, m_F = 0\rangle$ transition. b) Cavity transmission during the single atom preparation cycle. In this example, the ninth MW-pulse led to a transfer of an atom to $F=2$, as heralded in the subsequent low cavity transmission.

3.3.2. The reservoir and single atom extraction

The starting point for the single atom experiment is a BEC prepared in a dimple trap above the cavity mode, as described in chapter 2.4.1. The dimple trap is cigar shaped with its long axis perpendicular to the cavity axis and trap frequencies $(\omega_y/2\pi; \omega_\perp/2\pi) = (270; 4100)$ Hz. Radiofrequency evaporation is performed within 500 ms to a final RF-frequency of about 1 MHz, resulting in an almost pure BEC of around 500 atoms in state $|F = 2, m_F = 2\rangle$. While it is possible to cut farther into the BEC with the RF-knife and thereby further reduce the atom number, this method has not proven practical to

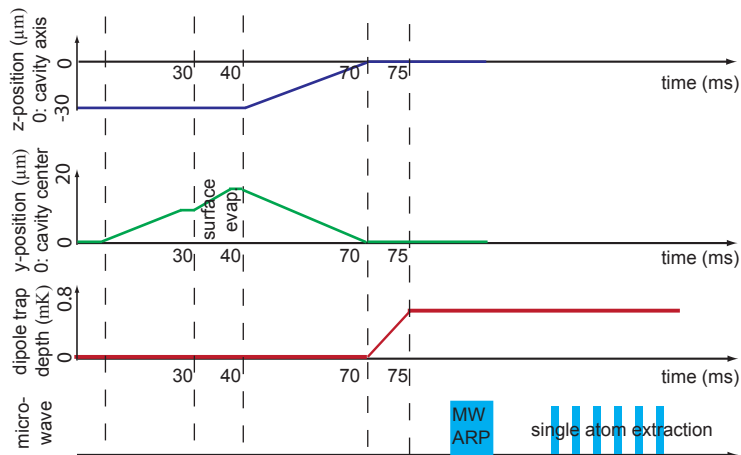


Figure 3.6.: Time line of the surface preparation and dipole trap loading. A BEC is initially trapped outside the cavity mode volume. It is brought towards one fiber end facet for surface evaporation (between 30 ms and 40 ms). The magnetic trap is then moved to the exact cavity mode center (at 70 ms), and the dipole trap is ramped up. The magnetic trap is then switched off, and a microwave adiabatic rapid passage (ARP) transfers the reservoir into $F = 1, m_F = 0$, from where the single atom extraction starts.

obtain ensembles of only a few atoms. In particular, relative atom number fluctuations become increasingly large when reducing the atom number in this way, preventing a reliable preparation of a determinate number of atoms. We think that magnetic field fluctuations are the cause of this problem.

The alternative method of surface evaporation has proven a more reliable way to reduce the atom number in our experiment. Surface evaporation has already been shown to be an alternative way to achieve BEC, and is a method particularly well suited for atom chips ([58, 70]). On an atom chip, magnetic traps can easily be brought close to surfaces, in our case the fiber end facets. At distances of less than about $1 \mu\text{m}$, the magnetic trap potential is disturbed by a combination of Casimir-Polder and Van der Waals-London forces due to interactions with the mirror surface and adsorbed atoms. The deformation of the trapping potential leads to a decrease in trap frequencies [90] and to the opening of a loss channel towards the approached surface.

Figure 3.6 shows a time line of the steps from surface evaporation to the loading of the dipole trap. To achieve surface evaporation in our experiment, the BEC is moved to within $5 \mu\text{m}$ of the fiber surface in 30 ms, a position where surface forces have no effect. A further ramp of the magnetic bias field by 800 mG during 10 ms moves the atom closer to the surface, leading to evaporation. The final number of atoms can be fine-tuned by changing the final bias field amplitude. The final position is held for a short time of around 1 ms, after which the atoms are moved to the center of the cavity mode in 30 ms. During this last transport, the atoms enter the cavity mode for the first time. The dipole trap light has to be switched off during this time to not interfere with

the magnetic potential. A feedforward is therefore used to stabilize the cavity length.

The atoms are now transferred into the intracavity dipole trap in two steps. First, the dipole trap is ramped up in 5 ms to a trap depth of 800 μK . The magnetic trap is then ramped down within 1 ms. A bias magnetic field of $B_0 = 3.7$ Gauss is applied to lift the degeneracy of the Zeeman levels. The small ensemble of atoms in state $|F = 2, m_F = 2\rangle$ is transferred to state $|F = 1, m_F = 1\rangle$ by means of a MW adiabatic rapid passage (ARP)[91]. Our MW-frequency generator does not allow sweeps of the MW frequency as required for an ARP. The ARP is therefore done by sweeping the bias field by 0.4 G around its nominal value B_0 with MW radiation resonant to the $|F = 2, m_F = 2\rangle \rightarrow |F = 1, m_F = 1\rangle$ transition frequency (Zeeman-shifted by B_0) turned on. The effective, Zeeman-shifted transition frequency is thereby swept across resonance with the MW, and a population transfer with efficiency $>99\%$ is achieved.

The atoms in $|F = 1, m_F = 1\rangle$ act as a dispersive medium for the cavity. The shift of the effective cavity resonance per atom can be calculated as

$$\delta_c = g_{|1,1\rangle}^2 / \Delta_{\text{HFS}} = 6.1 \text{ MHz}, \quad (3.1)$$

where $\Delta_{\text{HFS}}/2\pi = 6.8$ GHz is the ground state hyperfine splitting. The cavity shift induced by the atomic reservoir can be detected by measuring the cavity transmission. We measure cavity transmission during 150 μs to estimate the number of atoms in the reservoir. In postselection, we discard runs with more than 5 atoms in the reservoir to reduce the probability to accidentally extract more than one atom from the reservoir. We now apply a 1.9 μs MW pulse resonant to the $|F = 1, m_F = 1\rangle \rightarrow |F = 2, m_F = 0\rangle$ transition. The Rabi-frequency on this transition is $\Omega/2\pi = 34.6$ kHz, leading to a transfer probability per atom of $p_t = \sin(\Omega/2 \cdot 1.9 \mu\text{s})^2 = 4.2\%$. In order to detect whether the MW pulse has led to the transfer of an atom to $F = 2$, we measure the cavity transmission during 20 μs . Figure 3.7 shows a histogram of detected counts in 20 μs on the transmission APD following the MW pulse.

The measured probability distribution is well approximated by the sum of two Poissonian distributions of mean values 0.3 and 22, respectively. The low transmission peak corresponds to the presence of at least one $F = 2$ atom, whereas high transmission signals that no atom was transferred. The distribution drops to close to zero between the two peaks. This is of importance for the single atom preparation, since it justifies the choice of a threshold to determine whether an atom was transferred (in this case, the threshold is at 5 counts). The probability of a false positive event, i.e. a drop of cavity transmission below threshold although no atom is in $F = 2$, is given by $\sum_{i=0}^5 \lambda(i, 22) \approx 10^{-5}$, where $\lambda(i, \mu)$ is the poissonian probability distribution with mean μ .

We repeatedly apply this preparation cycle until a transmission level below threshold signals a successful transfer. Figure 3.8 shows the number of pulses required to prepare an atom. For a given number of atoms N_a in the reservoir, the probability that n_p MW pulses are needed before an atom is transferred is given by the geometric distribution, $P(n_p) = (1 - N_a p_t)^{n_p - 1} N_a p_t$. The distribution of n_p for an initial atom number distribution in the reservoir can be calculated, and the line in figure 3.8 shows the resulting fit assuming a Poissonian distribution with fitted mean of $\bar{N}_a = 1.5$.

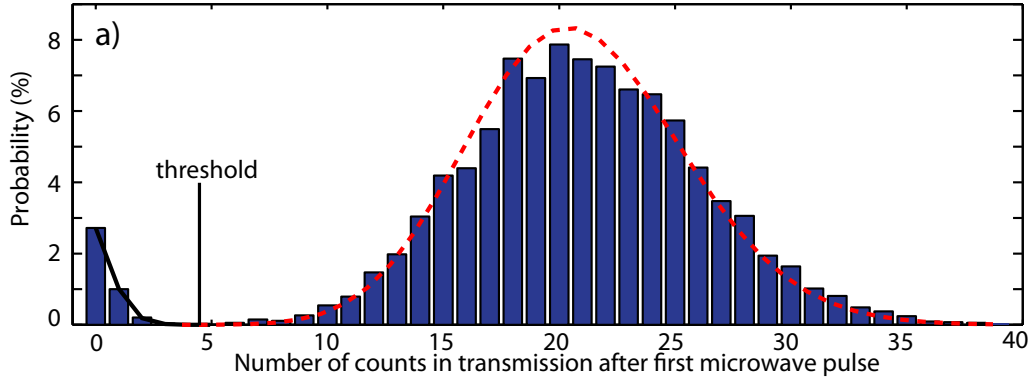


Figure 3.7.: Histogram of counts in transmission during $20\mu\text{s}$ after the first MW pulse during single atom preparation. The black and red lines are Poissonian fits with expectation values of 0.3 and 22 respectively. There is a clear dip between the two peaks, allowing us to use a thresholding technique to signal the preparation of a single atom. Compare this to the situation of atoms in the waveguide depicted in figure 3.4 a), where there is no clear-cut separation between the two maxima.

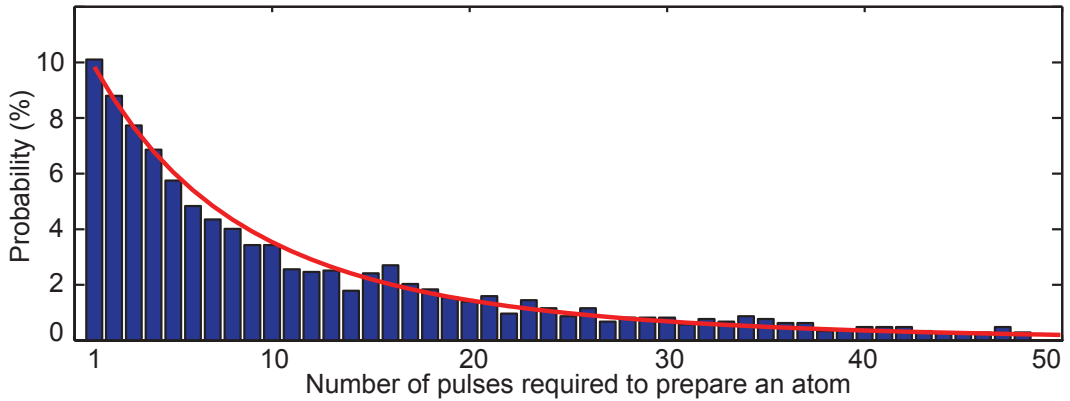


Figure 3.8.: Distribution of the number of required MW pulses to prepare an atom. The line is a fit assuming a reservoir with a Poisson distribution.

3.3.3. Reservoir removal

An experiment with the single extracted atom can now be started. However, for some experiments, and especially when the atom is to be used as a qubit, the reservoir should be removed from the dipole trap. This is achieved by first preparing the single atom in $F = 2$ in the $m_F = 0$ Zeeman state (see below). After this, the dipole trap is lowered to a depth of $25\mu\text{K}$ (corresponding to $\approx 500\text{ kHz}$), while at the same time applying a strong magnetic field gradient of 2.7 kG/cm . The field gradient is produced by a current of 3 A through the waveguide wire at a distance of $150\mu\text{m}$ from the atoms. The magnetic field gradient creates a strong force on the reservoir atoms in the magnetic-field sensitive

state $|F = 1, m_F = 1\rangle$, while the atom in $|F = 2, m_F = 0\rangle$ remains unaffected. The $|F = 1, m_F = 1\rangle$ state being a high-field seeker, the reservoir atoms feel a strong energy gradient along the z -axis of ≈ 1.9 GHz/cm. This gradient is slightly stronger than the one from the dipole trap, which is $500 \text{ kHz} \cdot \frac{d}{dz} e^{-2z^2/\omega_0^2}$ with a maximum of 1.5 GHz/cm. The magnetic field gradient is left on during 30 ms.

Figure 3.9 shows the successful removal of atoms when the dipole trap depth is lowered below the critical depth. Here, a large number of about 200 atoms in $|F = 2, m_F = 0\rangle$ was used to measure the efficiency of the push-out sequence. The probability that at least one atom is left in the dipole trap after the push-out sequence can be seen (blue points). As a comparison, the red points show the fraction of runs in which at least one atom remains in the trap when no push-out current is applied. This probability is limited by cavity length fluctuations leading to variations in the dipole trap depth.

In order not to remove the single atom in $F = 2$ during the push-out, it has to be in the magnetic field insensitive state $m_F = 0$. In the next section, we explain how we prepare the single atom in this state before switching on the magnetic field gradient.

3.3.4. Zeeman-state preparation

Cavity transmission is a good signal for the measurement of the atom's hyperfine state. However, it does not yield information concerning the Zeeman state. The different Zeeman states have comparable coupling strengths and are detuned from one another by much less than g_0 , such that cavity transmission does not depend on m_F . In order to prepare and detect well defined Zeeman states, we therefore use a slightly more elaborate scheme involving MW radiation, which selectively couples pairs of Zeeman states in the two hyperfine ground states. While the scheme described here may be used for any of the Zeeman states, we will focus on the states of the clock transition $|F = 1, m_F = 0\rangle \leftrightarrow |F = 2, m_F = 0\rangle$. The state $|F = 2, m_F = 0\rangle$ is of particular interest because we prepare it before the push-out of the reservoir. The state $|F = 1, m_F = 0\rangle$ will be used in chapter 5.

For the preparation of either clock state, we use the following protocol. We start by preparing a single atom in $F = 2$, as described above. We then apply a "preparation" MW π -pulse resonant to the clock transition. The Rabi frequency of the pulse is chosen low enough to have negligible transfer probability if the atom is not in a clock state. Typically, a bias magnetic field leading to Zeeman splittings on the order of $\Delta/2\pi = 1$ MHz is used, whereas the MW Rabi frequency on the clock transition is on the order of $\Omega_{MW}/2\pi = 30$ kHz. For atoms in a non-resonant Zeeman state, the transfer probability is $\Omega_{MW}^2/\Delta^2 \approx 10^{-3}$. The π -pulse efficiency for the resonant transition is $\approx 99\%$.

The "preparation" π -pulse is succeeded by a measurement of cavity transmission to determine the hyperfine state. If the atom is found to be in $F = 1$, we can conclude that the MW π -pulse was successful. We therefore know that the atom was in state $F = 2, m_F = 0$ before the π -pulse, and now is in $|F = 1, m_F = 0\rangle$. This state is unperturbed by the hyperfine state measurement, since the scattering rate of the atom in state $F = 1$ is on the order of 100 Hz, such that it is negligible compared to the measurement time. The preparation of $|F = 1, m_F = 0\rangle$ is thereby complete.

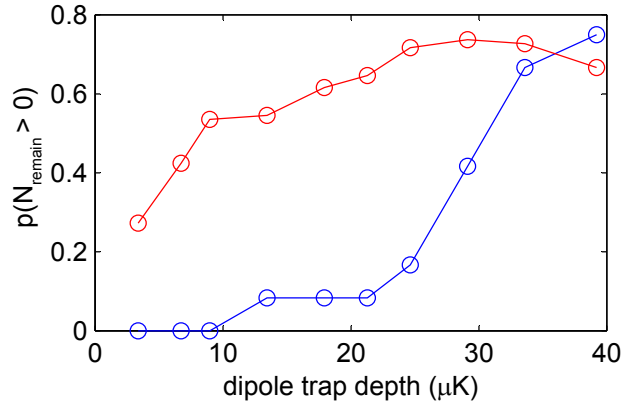


Figure 3.9.: Determination of the critical dipole trap depth for the push-out of the reservoir. For the measurement, an ensemble of ≈ 200 atoms in state $|F = 2, m_F = 2\rangle$ is trapped in a weak dipole trap. A current of 1.5 A through the waveguide wire is turned on during 30 ms, creating a strong force on the ensemble. After this push-out, cavity transmission is measured and a thresholding method used to determine whether at least one atom has remained trapped. Plotted is the fraction of runs in which at least one atom remains trapped after the push-out (called $p(N_{\text{remain}} > 0)$), versus the dipole trap depth on the x-axis (blue points). The red points are a reference measurement, where no push-out is performed in an otherwise identical measurement. Below a critical dipole trap depth of $25 \mu\text{K}$, atoms are removed from the dipole trap when the current is turned on, whereas the trap is strong enough to keep atoms trapped in the absence of the push-out current in 75% of the runs. The missing 25% are partially explained by dipole trap depth fluctuations due to cavity length variations during the waiting time. Note that the magnetic force on the atoms in this measurement is identical to the one experienced by $|F = 1, m_F = 1\rangle$ atoms with a waveguide current of 3 A.

If the atom was not in $|F = 2, m_F = 0\rangle$ before the preparation π -pulse, the atom remains in $F = 2$. In this case, we repeat the π -pulse / hyperfine state measurement procedure until the atom is transferred to $|F = 1, m_F = 0\rangle$. Note that each hyperfine state measurement redistributes the atom among the $F = 2$ Zeeman states due to scattering, such that the scheme eventually is successful in producing an atom in $|F = 1, m_F = 0\rangle$. A further π -pulse on the clock transition can be used to prepare $|F = 2, m_F = 0\rangle$.

This preparation scheme relies on two requirements. First, the probability of optically pumping an atom from $F = 2$ to $F = 1$ during the hyperfine state detection must be small. This condition is fulfilled since the $F = 2$ hyperfine state lifetime (≈ 50 ms, see section 3.4.2) is three orders of magnitude larger than the measurement time of $60 \mu\text{s}$.

Second, since the measurement of a $F = 1$ atom can not be distinguished from an atom lost from the dipole trap, the atom loss rate from the trap has to be much smaller than the preparation time. This condition is fulfilled as well, since the atomic life time in the dipole trap is on the order of hundreds of milliseconds (see section 3.4.1). We can additionally check for the presence of the atom at the end of the experiment to postselect only runs where the atom was present.

3.3.5. Two atom probability

The sequence of short microwave pulses used to transfer an atom into $F = 2$ from the reservoir can potentially transfer more than one atom. While we use the cavity transmission signal to verify the presence of an $F = 2$ atom after the short MW preparation pulse, we can not use the signal to differentiate between different atom numbers. This is because a single atom already leads to a very low transmission, which is not measurably lowered by additional atoms. We use two alternative methods to obtain the probability to prepare more than one atom.

First, knowing the atom number distribution in the reservoir (see figure 3.8) allows us to calculate the probability that the MW-pulse transfers more than one atom, given the event that it transferred at least one atom. Under the assumption of a Poissonian reservoir with the measured mean $\bar{N}_a = 1.5$, this probability is 2.6%.

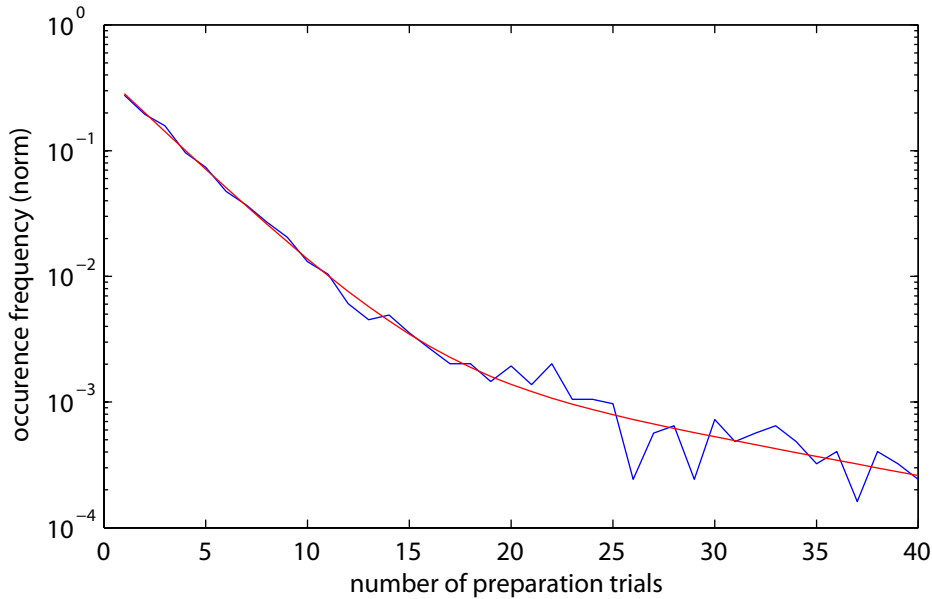


Figure 3.10.: Normalized histogram of the number of probe light pulses n_p required until only the $F = 2, m_F = 0$ state is populated. A sum of two functions with different mean number of pulses \bar{n}_p , corresponding to runs with one and two prepared atoms, fit the data well.

Second, we directly measure the probability of two atoms remaining in the dipole trap after the push-out sequence using the following method. We repeatedly attempt to pump the (single or more) atoms into $F = 2, m_F = 0$ by using probe light pulses. If there is only a single atom present, we expect it to be pumped into $m_F = 0$ after a mean number of probe pulses $\bar{n}_p = \bar{n}_{p,1}$ given by the inverse of the steady-state population in $m_F = 0$. If two atoms are present, the mean number of required pump pulses to pump both atoms into $m_F = 0$ is $\bar{n}_p = \bar{n}_{p,2}$. Assuming that the atoms are independent, $\bar{n}_{p,2} = \bar{n}_{p,1}^2$. Figure 3.10 shows the distribution of n_p obtained from around 15000 runs. The distribution is fitted by the weighted sum of the two functions expected for single atom runs and two atoms runs. Each is characterized by a mean number of pulses \bar{n}_p . We obtain $\bar{n}_{p,1} = 3.3 \pm 0.2$ and $\bar{n}_{p,2} = 14 \pm 2.5$. $\bar{n}_{p,1}$ and $\bar{n}_{p,2}$ correspond well to the calculated $m_F = 0$ steady state population of 0.32 obtained from the full master equation. The fitted weights give the fraction of runs with single atoms and two atoms prepared. They are (in percent) 94.2 ± 0.6 for the single atom function and 5.8 ± 0.6 for the two atom function.

The difference between the two-atom probability of 5.8% measured here and the 2.6% calculated above is probably due to errors in the measurement of the mean atom number in the reservoir as well as to an imperfect push-out of $F = 1$ atoms. In conclusion, the single atom preparation succeeds in the large majority of runs. In less than 6% of runs, two atoms are prepared instead. This number could be lowered by using even weaker MW pulses for the extraction of single atoms from the reservoir.

3.4. Characterisation of the single atom-cavity system

3.4.1. Dipole trap lifetime

An experimentally important parameter of the system is the time the single atom remains trapped in the dipole trap. Three possible loss processes exist. Collisions with the background gas (measured loss time constant in a magnetic trap: $\tau_{\text{bg}} = 1.4$ s), parametric heating at twice the trap frequency (we did not measure the noise spectral density at the relevant frequencies and therefore can not estimate the expected heating rate), and momentum diffusion due to off-resonant scattering and photon redistribution [92] (expected lifetime from momentum diffusion $\tau_{\text{md}} \approx 2$ s).

The experimental measurement of the dipole trap lifetime is straightforward. After the single atom preparation in a dipole trap of 3 mK depth, we switch off the detection light during a variable time t , and we then perform a further short transmission measurement to determine whether the atom is still trapped. Before the second measurement, we apply a short pulse on the repumper transition $|F = 1\rangle \rightarrow |F = 2\rangle$, perpendicular to the cavity axis. This pulse is required because dipole trap light can induce hyperfine state changing, off-resonant absorption-emission processes (the estimated rate of this process is at least an order of magnitude smaller than the expected dipole trap lifetime). Figure 3.11 shows the probability of the atom to still be trapped after time t . An exponential

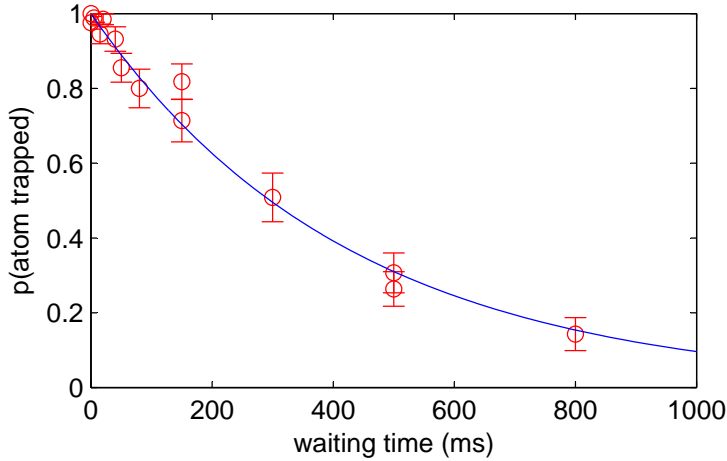


Figure 3.11.: Measurement of the dipole trap lifetime. The graph shows the fraction of atoms that remain trapped after a holding time t in a dipole trap of 3 mK depth. Data points of two different measurements are shown along with an exponential fit with decay constant 427 ms.

decay function with a fitted decay constant of 427 ± 15 ms fits the data well. Whilst we can not pinpoint the dominant heating mechanism, 427 ms is long compared to relevant experimental timescales such as our typical Rabi-frequencies (on the order of 30 kHz) and time necessary for atom detection (typically on the order of $100 \mu\text{s}$).

3.4.2. Single atom internal state dynamics

Information about the coupled atom-cavity system is obtained by transmission measurements of the probe laser. Figure 3.12 shows an experimental trace of cavity transmission with a single atom coupled to the cavity. Sudden changes in the transmission signal is observed. They are due to quantum jumps of the atom between the resonant $F = 2$ and the non-resonant $F = 1$ state. Transmission is low when the atom is in $F = 2$, due to the vacuum-Rabi splitting. An atom in $F = 1$ on the other hand has negligible effect to cavity transmission compared to an empty cavity. The atoms jumps between the hyperfine states due to non-resonant excitation to the $D2$ multiplet. An atom in $F = 2$ is resonantly excited to $F' = 3$ by the weak, but non-zero intracavity probe intensity, from where only the transition back to $F = 2$ is allowed. Off-resonant excitations to $F' = 2, 1$ however lead to a possible decay into $F = 1$. $F = 1$ atoms on the other hand are exposed to a much higher light intensity, since they have a negligible effect on the cavity resonance. However, they are 6.8 GHz off-resonant to the probe light and are only excited with weak rates to $F' = 0, 1, 2$, leading to the eventual decay to $F = 2$.

A large number of traces like the one shown in figure 3.12 allow us to directly measure the lifetimes of the hyperfine states under the action of probe light. To measure the distribution of lifetimes, we use a thresholding method to determine when a quantum jump happens. The detected signal in transmission, a flux of counts on the APD with

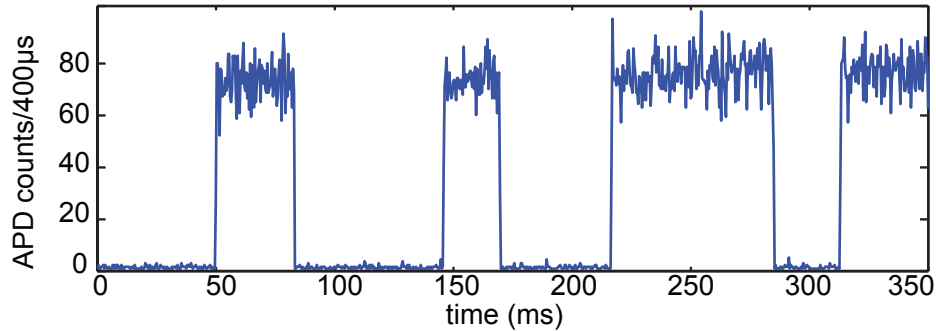


Figure 3.12.: Typical experimental trace of cavity transmission with a single atom coupled to the cavity. Sudden changes in the transmission signal are observed. They are due to quantum jumps of the atom between the resonant $F = 2$ and non-resonant $F = 1$ hyperfine state.

rate $\Phi_t(t)$ is integrated during a signal integration time t_{int} . We determine that the atom underwent a hyperfine changing scattering event at time τ if the integrated signal $N = \int_{\tau}^{\tau+t_{int}} \Phi_t(t) dt$ becomes larger (or smaller) than a threshold value N_{crit} . N_{crit} is typically chosen at about $N_{F=1}/2$, where $N_{F=1}$ is the number of counts expected during t_{int} if the atom is in $F = 1$. The integration time is chosen such that $N_{F=1} \approx 15$, so that photonic shot noise does not contribute to the observed quantum jumps. Figure

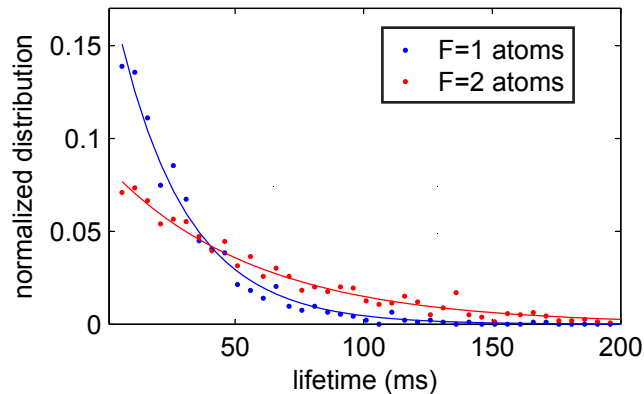


Figure 3.13.: Single atom hyperfine state lifetimes under the action of probe light. A total of 1594 events with an atom in $F = 2$ and 937 events with an atom in $F = 1$ are shown in the form of a histogram. The lines are exponential fits with decay times of 26 ms ($F = 1$) and 52 ms ($F = 2$).

3.13 shows histograms of the duration the atom spends in either $F = 1$ or $F = 2$ before a quantum jump happens. Both histograms show an exponential decay with decay constants of 26 ms for $F = 1$ atoms and 52 ms for $F = 2$ atoms. Probe power for this

measurement corresponded to $\Phi_0 = 1.9 \cdot 10^5 \text{ s}^{-1}$ for the empty cavity, and integration time was chosen as $t_{int} = 15/\Phi_0 \approx 79 \mu\text{s}$.

The same traces allow to determine the count rates in both transmission and reflection. The count rate in transmission for an atom in $F = 1$ is equal to the empty cavity transmission of $\Phi_0 = 1.9 \cdot 10^5 \text{ s}^{-1}$, with an atom in $F = 2$ it is reduced to $1.4 \cdot 10^3 \text{ s}^{-1}$ or $0.0074 \cdot \Phi_0$. The count rates in reflection are $4.4 \cdot 10^5 \text{ s}^{-1}$ with an atom in $F = 1$ and $1.9 \cdot 10^5 \text{ s}^{-1}$ with an atom in $F = 2$.

A noteworthy feature of the transmission traces as shown in figure 3.12 is the absence of any sign of an increase of the count rate with time when the atom is in $F = 2$. Indeed, one might expect this count rate to increase as the atom heats due to spontaneous scattering. Heating of the atom has two effects. First, it leads to a decrease in its coupling strength to the cavity. Second, it decreases the light shift due to the dipole trap, shifting the atomic resonance away from the probe laser frequency. Both effects lead to an increase in cavity transmission. The absence of this observation leads us to conclude that the atom remains at a position of strong coupling until it is lost from the dipole trap.

3.5. Vacuum Rabi splitting

To show that all single atoms we prepare couple to the cavity with similar strength, we measure the normal-mode spectrum of the atom-cavity system. The theory of the vacuum Rabi splitting for our system was presented in chapter 1. Here, we use a transmission measurement by pumping the cavity to obtain the spectrum. Alternatively, we excite the atom perpendicularly to the cavity axis, and collect fluorescence through the cavity fibers.

3.5.1. Spectroscopy of the strongly coupled system

We use the following experimental sequence to measure the spectrum of the atom-cavity system. After preparing a single atom, we probe cavity transmission at a given probe-cavity detuning $\Delta_{pc} = \Delta_{pc,i}$ during $8 \mu\text{s}$. To ensure that the atoms has remained trapped during the probe pulse, we then apply a short repump pulse transversally to the cavity axis and check that the on-resonance cavity transmission is below the preparation threshold. For this, we change the probe frequency to cavity resonance. If this measurement confirms that the atom still couples to the cavity, we set the probe laser frequency back to $\Delta_{pc,i}$ and again measure transmission. This measurement-control cycle is repeated until the atom is lost. For each probe detuning $\Delta_{pc,i}$, the transmission signals of approximately 20 atoms are averaged.

Both dipole trap light and probe light are linearly polarized along axis $\hat{e}_{c,b}$ corresponding to the blue cavity eigenpolarization with resonance frequency $\omega_{c,b}$. (The second cavity eigenpolarization axis $\hat{e}_{c,r}$ has resonance frequency $\omega_{c,r}$ such that $\omega_{c,b} = \omega_{c,r} + \Delta_{bi}$.) The bias magnetic field of 3.7 G is also polarized along $\hat{e}_{c,b}$. The dipole trap gives rise to a light shift of -60 MHz to the $F = 2$ multiplet, and an m_F -dependent light shift to the

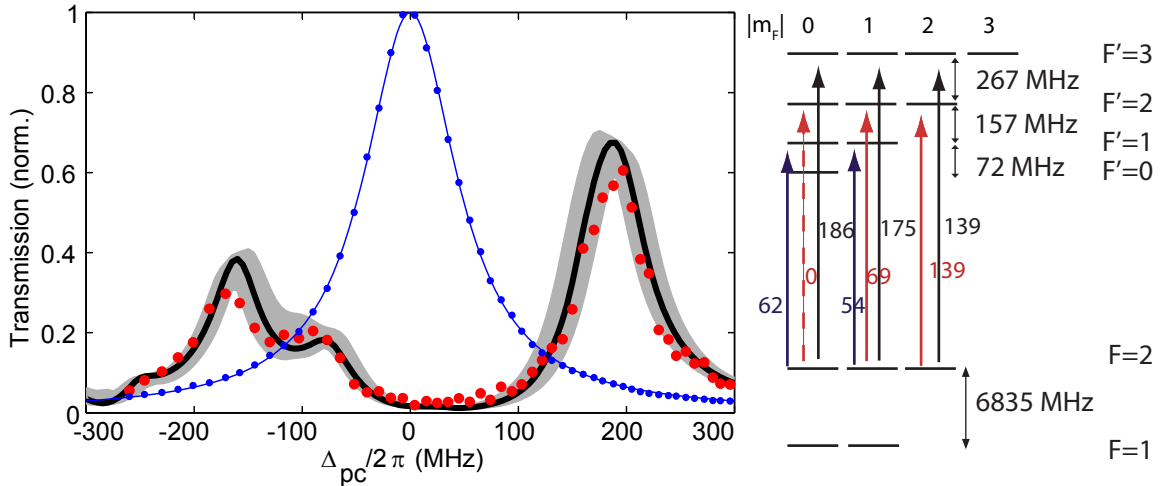


Figure 3.14.: a) Normal-mode spectrum of a single atom coupled to the cavity. Red points are the measured transmission. The black line is the steady-state solution of the master equation for $g_0/2\pi=240$ MHz and $\Delta_{ac}=0$. The gray area bounds the solutions when varying $g_0/2\pi$ by ± 10 MHz and $\Delta_{ac}/2\pi$ by ± 10 MHz. The blue dots are the measured empty cavity transmission. The blue line is a Lorentzian fit to the measured cavity transmission, giving a fitted width of 53 MHz. b) Level scheme including coupling strengths (in MHz) for different transitions connecting Zeeman sublevels of $F = 2$ to the excited states. Note that coupling strengths do not depend on the sign of m_F . The difference in coupling strengths explains the asymmetric normal-mode spectrum, as described in the text.

excited states in multiplet $F' = 3$. In first order calculations, taking into account contributions only from the $D2$ and $D1$ transitions, the lightshift in this multiplet is 33 MHz for $m_F = 0$, 29 MHz for $m_F = \pm 1$, 18 MHz for $m_F = \pm 2$ and 0 for $m_F = \pm 3$.

The measured normal-mode spectrum is shown in figure 3.14. The multilevel atomic structure coupled to the two-mode cavity leads to a rich structure in the observed spectrum. Especially striking is the asymmetry between the two-peak structure observed for $\Delta_{pc} < 0$ and the single peak for $\Delta_{pc} > 0$, which can be understood qualitatively as follows. Depending on the probe laser frequency, optical pumping leads to different steady state populations in the $F = 2$ multiplet. Only the state $F = 2, m_F = 0$ approximates a two-level atom coupled to the cavity, since it has no allowed π transitions to $F' = 3$ (see figure 3.14). Population in this state leads to the dominant peak on the left (red detuned) side of the spectrum at -190 MHz, and also contributes to the peak on the blue detuned side of the spectrum. The population in $m_F = \pm 1, 2$ is also coupled to $F' = 3$, but with smaller coupling strengths due to smaller Clebsch-Gordan coefficients. These levels however have additional allowed transitions to $F' = 2$ and $F' = 1$, red detuned to the probe laser and cavity. The combined effect of a smaller coupling strength plus

the additional coupling to a red-detuned transition leads to a second peak for $\Delta_{pc} < 0$, whereas the two effects lead to opposite and almost equal shifts compared to the $m_F = 0$ population for $\Delta_{pc} > 0$, leading to a single peak on the blue side of the spectrum.

Along with the measurement, figure 3.14 shows the steady-state solution of the master equation taking into account the coupling of the atom to both cavity polarization eigenmodes, dipole trap light shifts, magnetic field and the excited state multiplets $F' = 1, 2, 3$. The coupling strength g_0 was used as only adjustable parameter in the model. The value extracted from the fit is $g_0 = 240 \pm 10$ MHz, 12% higher than the value calculated from the mode volume given by mirror curvatures (see [70]). Since the mirror curvatures underlying this calculations are not known with good precision, this measured value of g_0 is well within the error bar of the calculation.

The high value of the observed coupling and the absence of broadening of the peaks compared to the master equation (which assumes a point-like atom positioned at exactly an anti-node of the probe light) is a strong indication that a large fraction of the prepared single atoms are indeed trapped close to the maximum of the cavity field. This is in agreement with the observed binary transmission level during preparation (see figure 3.7), where no intermediate levels of transmission are observed.

In order to observe a Rabi-spectrum more closely resembling the ideal case of a two-level atom, we measured the normal-mode spectrum for single atoms prepared in state $|F = 2, m_F = 0\rangle$ (see chapter 3.3.4 for the preparation of this state). Figure 3.15 shows the time-resolved spectrum observed for atoms initially in $|F = 2, m_F = 0\rangle$. When measuring the transmission only during a time smaller than the optical pumping time, the spectrum is almost symmetrical, as expected for a two-level atom. With continuous probing, the system evolves towards the steady state and the spectrum reaches the associated asymmetrical shape.

3.5.2. Fluorescence single atom vacuum Rabi spectrum

For the results presented so far, measurements were performed by pumping a cavity mode and observing cavity transmission. The Jaynes-Cummings hamiltonian however is symmetric with respect to the atomic and photonic operators, and the atom-cavity system can equivalently be probed by driving the atom, using a pump beam perpendicular to the cavity axis. An excitation in the cavity mode builds up due to the strong coupling of the atom to the mode. The excitation of the cavity mode decays with rate κ into the cavity fibers, such that the number of photons in the cavity can be measured on the APD's.

The experimental procedure is similar to the one used in chapter 3.5.1 to measure the vacuum Rabi splitting via the cavity transmission. With the lower-frequency cavity mode resonant to the $|F = 2, m_F = 0\rangle \rightarrow |F' = 3, m_F = 0\rangle$ transition, a single atom is prepared in the cavity using cavity transmission to signal a successful preparation. The side excitation beam, polarized perpendicular to the cavity axis and parallel to the chip surface (\hat{x}), is then turned on during 5 ms. We use the APD on the single-mode fiber output to measure the number of photons in the cavity during the side excitation pulse. The frequency of the side excitation beam $\omega_p/2\pi$ is changed from run to run over

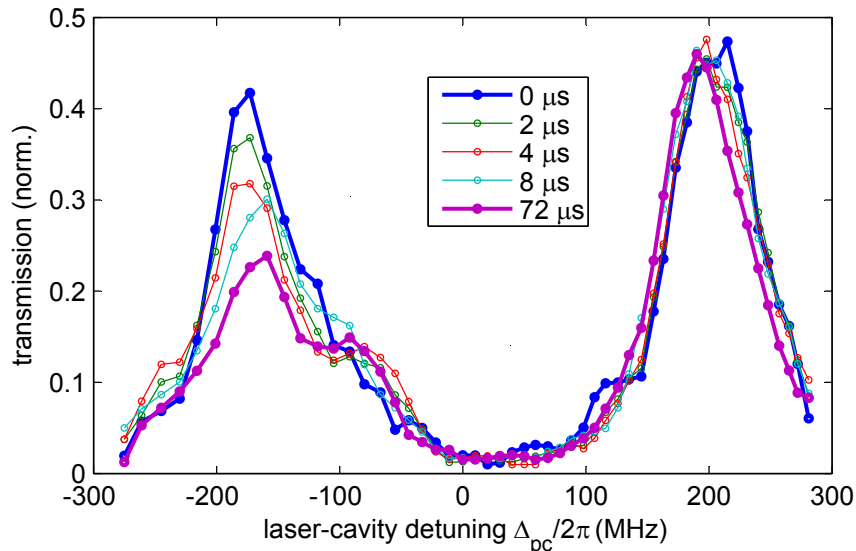


Figure 3.15.: Time-resolved normal-mode spectrum of a single atom coupled to the cavity. The atom is initially prepared in $m_F = 0$. For each curve, the transmission is integrated over $2 \mu\text{s}$ after a variable time of probing. The normal-mode spectrum changes as the atom is optically pumped. After $72 \mu\text{s}$, the asymmetric normal-mode spectrum closely resembling the steady state as shown in figure 3.14 is reached.

a range of ± 800 MHz.

Figure 3.16 shows the observed count rates during the first $400 \mu\text{s}$ of the pump interval as a function of the probe frequency. Four distinct peaks can be distinguished. As in the transmission measurement, the normal-mode spectrum is asymmetric, around $\Delta_{pc} = 0$, with two peaks on the red-detuned side. Due to the different pumping process, the weight of the three peaks is different however, see figure 3.16 b). A broadening of the peaks is also observable, and the peaks are closer to resonance. We attribute this to heating of the atom during the measurement due to the pump beam. Heating of the atom leads to higher amplitude oscillations in the dipole trap, and therefore simultaneously to a decrease in coupling strength and increase in detuning of the atom due to a decrease in the average light shift. Both effects lead to a broadening of the peaks.

The measured frequency range is large enough to observe the coupling to the second, higher frequency cavity mode. Corresponding to the birefringent splitting of $\Delta_{bi}/2\pi = 540$ MHz, the cavity-like peak of the second mode leads to an increased count rate between $\Delta_{pc}/2\pi = 500$ MHz – 600 MHz.

The total count rate with the side excitation beam on, but without atom coupled to the cavity, is on the order of 1 kHz, much lower than the observed signal on the peaks of the spectrum.

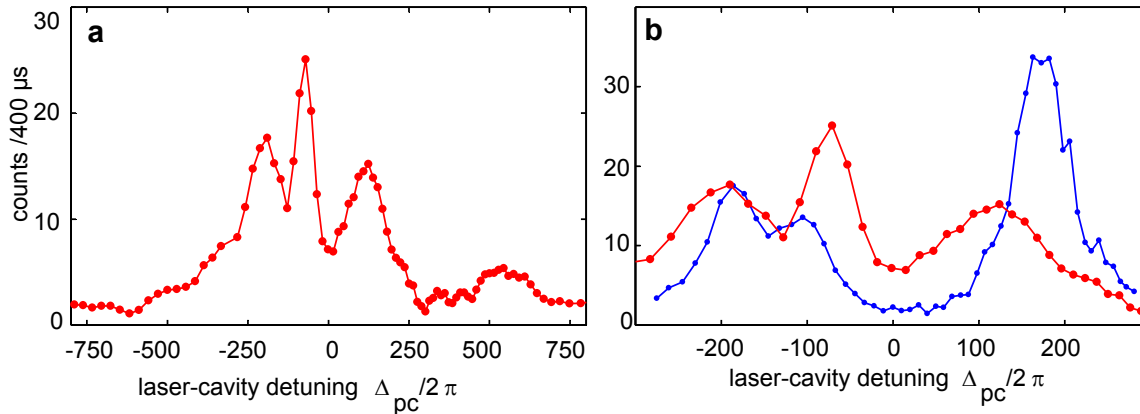


Figure 3.16.: Fluorescence measurements of the normal-mode spectrum. A single atom coupled to the cavity is driven by a pump laser perpendicular to the cavity axis, and photons leaking out of the cavity are detected. a) Full spectrum showing the normal mode spectrum of the resonant mode as well as the off-resonant second cavity mode at 540 MHz. Each data point is an average of about 5 runs. b) Same data as in a) (red), compared to the normal mode spectrum measured in transmission (blue). The y-axis for the blue curve was changed to enable an easy comparison.

3.6. Conclusion

This chapter discussed the preparation of single atoms to an FFP cavity on an atom chip. A BEC is the starting point of the single atom preparation. Thanks to the magnetic potentials available on the atom chip, the BEC can be positioned with high precision at the center of the cavity mode volume. The single atom is extracted from the BEC and is therefore in a well-defined antinode of the intra-cavity dipole trap. A high degree of control over the coupling strength between the cavity and the single atom is therefore achieved. The coupling strength was directly measured in the form of the normal-mode spectrum of the coupled system. The measured spectrum corresponds very well to the solution of the full master equation. The measured coupling strength corresponds to the maximum coupling strength expected when the atom is at the exact maximum of the cavity field, giving an indication that the single atom is cold and close to its motional ground state.

4. Detection of a single atom hyperfine state

This chapter discusses the characteristics of the FFP cavity when used as a state-dependent detector for single atoms. An introduction to existing methods for detecting single atoms is presented, and their advantages and disadvantages discussed. Our cavity-based detection scheme is introduced together with two different methods enabling us to access the hyperfine state from cavity transmission and reflection. Experimental results quantifying the detection fidelity are presented. Finally, the time-dependency of the detection fidelity is investigated to achieve detection times in the microseconds range.

4.1. Introduction

The read-out of the internal state of neutral atoms or ions is of importance for many experiments in quantum optics and atomic physics. In quantum information applications for example, the internal states of atoms represent an ideal carrier of information due to long coherence times and the well-defined transition frequencies. The qubits are typically encoded into hyperfine states of single atoms (or ions), or are mapped onto them before detection [93]. Detection of the hyperfine state then constitutes the last step to obtain the result of an experiment (e.g. a gate operation), and as such is a crucial component in determining the overall fidelity of the experiment.

The most important characteristics of any internal state read-out are detection error, detection time and destructiveness or repeatability [94]. The requirements for detection error vary with the application at hand. In general, it would be desirable to have a detection error that is not a limiting factor for the experiment. With single ions, two qubit quantum gates reach fidelities of up to 99.3% [95]. For fault-tolerant quantum computation, the error requirements is thought to lie around 10^{-4} [96, 97], and computational overhead varies inversely with the required gate fidelity. A detection error in the range of 10^{-4} is therefore required for this kind of application.

Detection time should as a minimum requirement be much faster than the qubit's decoherence time. For hyperfine qubits in neutral atoms, this requirement is not overly stringent, since coherence times can be in the range of seconds [98]. For quantum information processing proposes, detection time however can easily become a limiting factor to the repetition rate. With two qubit gate times on the order of microseconds or less [99–102], minimizing the detection time with concurring low detection error is of high relevance.

Similarly, repeatability and non-destructiveness in the sense that the atom or ion not

be lost due to the detection is relevant to the repetition rate of the experiment. For neutral atoms, single atom preparation (or loading) times typically are on the order of many milliseconds or seconds, such that experiment repetition rates are greatly reduced if the detection is destructive.

4.1.1. Single atom state detection methods

Hyperfine state read-out for neutral atoms has proven to be a challenging task. While many methods have been devised and implemented, many of them face drawbacks. In many cases, they are intrinsically destructive [103–107]. Others lack efficiency, such that only a small part of the read-out attempt lead to a definite result [108, 109]. In all of these schemes, as well in those that circumvent these drawbacks [89, 110–114], read-out error has not reached the values of down to 6×10^{-4} achieved in the best hyperfine state detections with single ions [59, 93].

The dominant quantum state read-out method implemented in ion traps is state-selective fluorescence [115–118]. The method relies on a close transition to scatter many thousands of photons. Since each scattering event leads to the heating of the atoms by an amount around the recoil temperature $T_{\text{recoil}} = \hbar^2 k^2 / mk_B$, quite large trap depths are required in order not to lose the atom before successfully detecting it. Ion traps are many thousand of Kelvin deep and fulfill this requirement. Impressive detection fidelities of up to 99.99% (for an optical qubit) are possible as a result [59]. Since traps for neutral atoms typically have a depth of only a millidegree Kelvin, the heating caused by many thousand recoils easily pushes the atom out of the trap. Only recently have two groups been able to overcome this problem by using high numerical aperture optics for fluorescence detection, demonstrating the possibility to adapt fluorescence detection for neutral atoms [113, 114]. Fuhrmanek et al. reached 98.6% detection efficiency without losing the atom.

Another widely used method is the so-called push-out detection. Here, the atom is state-selectively removed from the trap by a resonant laser [103–106, 119, 120]. This method leads to detection errors on the order of 1%, and is destructive by definition.

State-dependent ionization of atoms is another destructive detection scheme [13, 107, 121]. A static electric field is used for ionization, and the resulting charged particles are detected on multi-channel plates. Detection speeds are quite high ($1 \mu\text{s}$), and detection errors are around 5%.

To aid optical detection schemes, cavities can be used. Cavities can help increase detection fidelity in two ways. One is by increasing the collection efficiency in a fluorescence measurement ([108, 112]). When coupling the atom to a cavity, the Purcell effect leads to an increased spontaneous emission rate into the cavity mode when exciting the atom perpendicularly to the cavity axis. Most of the fluorescence emission can therefore be collected. This scheme is most suited to the "bad cavity" regime of cavity QED. A detection fidelity of 99.4% was reached in $85 \mu\text{s}$ by Bochmann et al ([112]).

The method we have chosen to pursue is to measure the state dependent cavity transmission and reflection to read out the hyperfine state ([89, 110]). The most important parameter in this scheme is the cooperativity of the system, since a high cooperativity

leads to a large state-dependent transmission ratio and a low scattering rate. Our cavity is therefore uniquely suited for this detection method. In the following, we describe the detection process in detail.

4.1.2. Detection error and fidelity

We start by clarifying the fundamental concepts of detection error and detection fidelity. Consider a system that can be in one of two quantum states $|0\rangle$ or $|1\rangle$. A measurement device is used to determine in which of the states the system is. After each measurement, the device is supposed to yield measurement result "0" (or "1") if the system was in state $|0\rangle$ (or $|1\rangle$) just before the measurement. For a non-perfect measurement device, two detection errors ϵ_0 and ϵ_1 can then be defined. The error ϵ_0 is given by the probability that the device gives out "1" even though the system was in $|0\rangle$, and ϵ_1 is the corresponding error if the system was in $|1\rangle$. If we suppose that the system has equal probability to be in either state, the mean detection error is defined as

$$\epsilon = \frac{\epsilon_0 + \epsilon_1}{2}. \quad (4.1)$$

We define the fidelity \mathcal{F} as

$$\mathcal{F} \equiv 1 - \epsilon. \quad (4.2)$$

This is a definition that is widely used in quantum computing literature. It gives the expected fraction of correct read-outs when many measurements are performed. An alternatively employed, slightly more conservative, definition is $\mathcal{F} = 1 - \max\{\epsilon_0, \epsilon_1\}$ (e.g. in [112]). Note that it is critical for either definition to make sense that the efficiency of the device be 100%, meaning that the device gives a definite read-out of either 0 or 1 after each measurement.

4.2. Accessing the quantum state from photon counts

4.2.1. Counts thresholding in two dimensions

Consider the situation depicted in figure 4.1 a). A ^{87}Rb atom is strongly coupled to a high-finesse cavity. The cavity and probe laser are tuned to resonance to the optical transition between the $F = 2 \rightarrow F' = 3$ states, such that both cavity reflection and transmission strongly depend on the internal (hyperfine) state of the atom: an atom in the resonant state $F = 2$ blocks cavity transmission due to the vacuum Rabi splitting, whereas an atom in state $F = 1$ has no effect on cavity transmission since it is very far detuned from the probe frequency. The reflection signal is inverse to the transmission, it is high for an atom in $F = 2$ and low for an atom in $F = 1$. An experimental of both cavity transmission and reflection is shown in figure 4.1 b).

The count rate measured by the APD in transmission is Φ_{F1}^T (Φ_{F2}^T) for an atom in $F = 1$ ($F = 2$), whereas the count rate in reflection is Φ_{F1}^R (Φ_{F1}^R). In this situation,

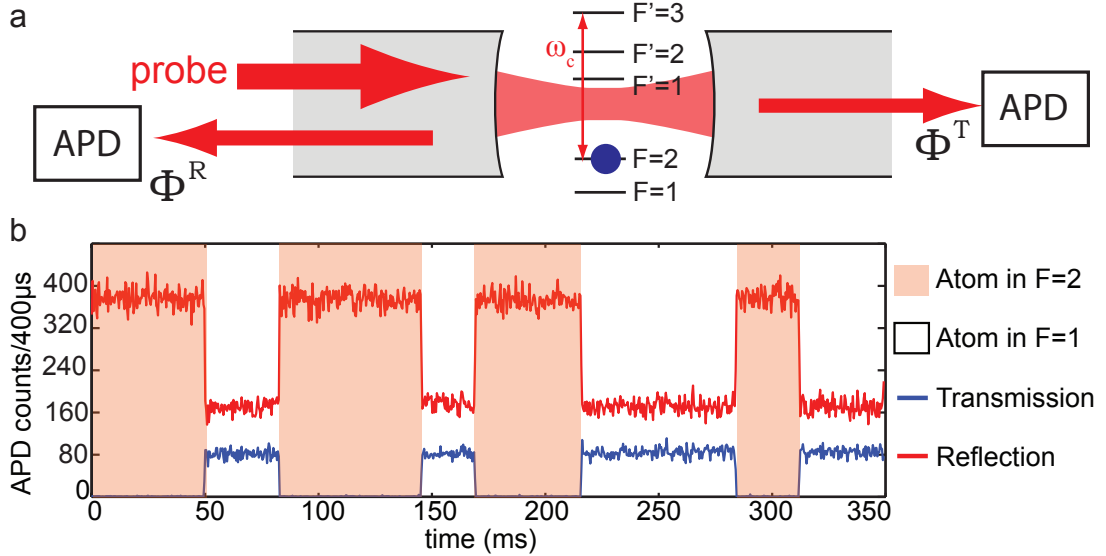


Figure 4.1.: a) Principle of cavity based state detection. Cavity reflection and transmission depend on the hyperfine state of the atom coupled to the cavity. APD's detect the photon fluxes Φ^R and Φ^T . b) Experimental trace of cavity reflection and transmission with an atom coupled to the cavity. Both signals depend on the hyperfine state of the atom, as can be observed when the atoms changes its hyperfine state under the action of probe light.

a hyperfine state detection can be realized by integrating the photon counts during a detection time T . The probability distribution to observe $(c_R = T \cdot \Phi^R, c_T = T \cdot \Phi^T)$ counts in reflection and transmission will be different for an atom initially in $F = 1$ or $F = 2$. We call $p_{F2}(c_R, c_T)$ ($p_{F1}(c_R, c_T)$) the probability distribution obtained for an atom initially in $F = 2$ (resp. $F = 1$).

The two-dimensional threshold method consists in taking outcomes in subspace \mathcal{C}_2 defined by $p_{F2}(c_R, c_T) > p_{F1}(c_R, c_T)$ to signal an atom in $F = 2$ and an atom in $F = 1$ if the outcome is in \mathcal{C}_1 defined by $p_{F2}(c_R, c_T) \leq p_{F1}(c_R, c_T)$. Note that this is a straightforward extension of thresholding using a single (e.g. fluorescence) signal.

The detection errors ϵ_{F1} and ϵ_{F2} using this method are determined by the overlap between p_{F2} and p_{F1} . They are given by $\epsilon_{F1} = \sum_{\mathcal{C}_2} p_{F1}$ and $\epsilon_{F2} = \sum_{\mathcal{C}_1} p_{F2}$. This overlap, and therefore the detection errors, is determined by two factors. In general, the distributions p_{F1} and p_{F2} are Poisson distributions due to photon shot noise. The contribution of the overlap due to this noise can be made arbitrarily small by increasing the integration time, and therefore the mean number of counts detected in transmission and reflection. The second contribution to the overlap is due to depumping into the other hyperfine state during the detection time. This happens due to off-resonant excitation of the $F' = 2$ and $F' = 1$ states (see section 3.4.2). Since the probability of depumping increases with detection time, so does the contribution of this effect to the detection error. An optimum

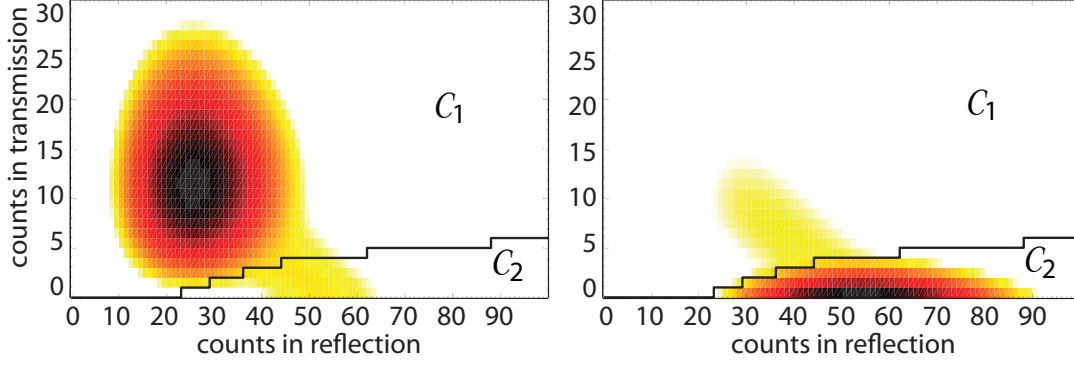


Figure 4.2.: Example of a two-dimensional distributions of counts expected with an atom prepared in $F = 1$ (left) and $F = 2$ (right). The solid black lines represent the threshold used to differentiate $F = 2$ from $F = 1$ atoms. The tail on the "wrong" side of the threshold is due to depumping during the detection time. The calculation is based on experimentally measured parameters ($\tau_{F1} = 26$ ms, $\tau_{F2} = 52$ ms, $\Phi_{F2}^R = 8.8 \times 10^5$ s $^{-1}$, $\Phi_{F1}^R = 4.3 \times 10^5$ s $^{-1}$, $\Phi_{F2}^T = 1.3 \times 10^3$ s $^{-1}$, $\Phi_{F1}^T = 1.8 \times 10^5$ s $^{-1}$, detection time 60 μ s).

detection time can be determined that minimizes the detection error.

Assuming poissonian count distributions and exponential distributions of hyperfine state lifetimes (with time constants τ_{F1} and τ_{F2}), we calculate $p_{F2}(c_R, c_T)$ and $p_{F1}(c_R, c_T)$ as

$$\begin{aligned}
 p_{F2} &= e^{-T/\tau_{F2}} \lambda(c_R, T \cdot \Phi_{F2}^R) \lambda(c_T, T \cdot \Phi_{F2}^T) + \dots \\
 &\quad \int_0^T \frac{e^{-t_d/\tau_{F2}}}{\tau_{F2}} \lambda(c_R, (T - t_d) \cdot \Phi_{F1}^R + t_d \cdot \Phi_{F2}^R) \lambda(c_T, (T - t_d) \cdot \Phi_{F1}^T + t_d \cdot \Phi_{F2}^T) dt_d \\
 p_{F1} &= e^{-T/\tau_{F1}} \lambda(c_R, T \cdot \Phi_{F1}^R) \lambda(c_T, T \cdot \Phi_{F1}^T) + \dots \\
 &\quad \int_0^T \frac{e^{-t_d/\tau_{F1}}}{\tau_{F1}} \lambda(c_R, (T - t_d) \cdot \Phi_{F2}^R + t_d \cdot \Phi_{F1}^R) \lambda(c_T, (T - t_d) \cdot \Phi_{F2}^T + t_d \cdot \Phi_{F1}^T) dt_d,
 \end{aligned} \tag{4.3}$$

where $\lambda(k, \mu)$ is the Poisson distribution with mean μ . The first term in p_{F2} and p_{F1} is the purely poissonian count distribution arising when the atom does not change its hyperfine state during readout, multiplied by the probability that the atom is not depumped. The count rate in transmission and reflection stays constant and is integrated over detection time T . The probability that the atom is not depumped during T is $e^{-T/\tau_{F1}}$ (resp. $e^{-T/\tau_{F2}}$) when it is in $F = 1$ (resp. $F = 2$). The second term in p_{F2} and p_{F1} is the count distribution arising when the atom changes its hyperfine state within T . The probability of depumping at time t_d is $\frac{e^{-t_d/\tau_{F1}}}{\tau_{F1}} dt_d$ (resp. $\frac{e^{-t_d/\tau_{F2}}}{\tau_{F2}} dt_d$). This probability multiplied by the count distribution arising when the atoms is depumped at t_d , integrated over all possible depumping times, gives the second terms in p_{F2} and p_{F1} . An example of a calculated distribution for an atom in either $F = 2$ or $F = 1$ is shown in figure

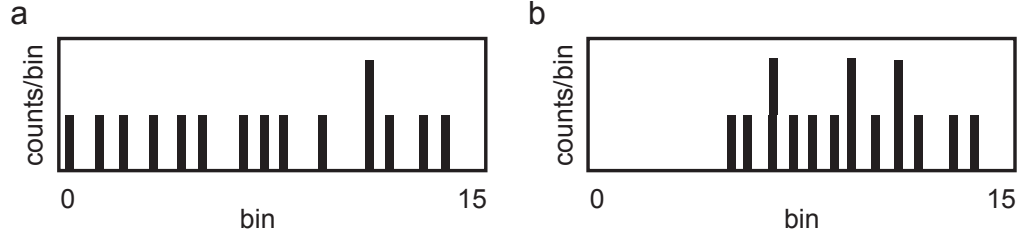


Figure 4.3.: Sketch of time resolved counts in transmission for two possible detection events of 15 photons each. Supposing an $F = 1$ atom would lead to one count per bin on average, both traces would lead to the detection result $F = 1$ when using a simple thresholding. The maximum likelihood method on the other hand accesses the time resolved data and would lead to the (probably correct) result that the atom in trace b) initially was in $F = 2$. In our experiment, we additionally use reflected counts to access the state for both threshold and maximum likelihood method.

4.2. The contributions of the two terms are clearly visible. The main components of the distributions are Poisson distributed. They are accompanied by a tail caused by depumping. The border between the two subspaces \mathcal{C}_1 and \mathcal{C}_2 is made explicit by the two-dimensional threshold shown as a thick black line.

4.2.2. Maximum likelihood method

The simple count thresholding method discards the useful information encoded in the temporal evolution of the count signals. Consider a situation where the qubit under measurement is depumped from $F = 2$ to $F = 1$ during the measurement time τ_{meas} . The transmission signal may then contain a significant amount of counts (bigger than the optimal threshold), such that the threshold method would lead to the wrong identification of the initial atomic state as $F = 1$. The counts are clustered near the end of the detection time, after the scattering event leading to depumping has occurred, but the count histogram does not reveal this. In these cases, the use of a time-resolved measurement and associated analysis method leads to an improvement in the detection error[122]. Here, we make use of the maximum likelihood method (MLM) [59].

To apply the MLM, we divide the detection pulse into N time bins of length T_{bin} . T_{bin} is chosen much smaller than the expected measurement time (in our case, the lower limit is given by the counter clock rate, leading to $T_{bin}=4\mu s$). The transmission and reflection counts for every bin constitute a set $M = \{c_R^i, c_T^i\}$, where $i=1 \dots N$ refers to the bin number. We calculate the probability q_{F2} that a given set M was generated by an atom initially in $F = 2$ as well as the probability q_{F1} that the same set was generated by an atom initially in $F = 1$. The criterion for discrimination between $F = 2$ and $F = 1$ atoms is simple: If $q_{F2}(M) > q_{F1}(M)$, we infer that the atom was in $F = 2$, and

vice versa. The maximum number of bins N is chosen such that a further increase in detection time does not significantly alter the outcome of the measurement.

We use a recursive calculation over M to obtain q_{F2} and q_{F1} . To this end, we define p_a^k and p_b^k , the probability that the atom initially (i.e. before the detection pulse) was in state $F = a$ ($F = b$) and that its state after bin k is $F = b$ ($F = a$), given the observed trace $M = \{c_R^i, c_T^i\}$, $i = 1 \dots k$. It follows that

$$q_{F2} = p_{22}^k + p_{21}^k \quad (4.4)$$

$$q_{F1} = p_{11}^k + p_{12}^k. \quad (4.5)$$

We use a recursive calculation to find $p_{a,b}^N$:

$$p_{11}^i = p_{11}^{i-1} f_{11}(c_R^i, c_T^i) + p_{12}^{i-1} f_{21}(c_R^i, c_T^i) \quad (4.6)$$

$$p_{12}^i = p_{12}^{i-1} f_{22}(c_R^i, c_T^i) + p_{11}^{i-1} f_{12}(c_R^i, c_T^i) \quad (4.7)$$

$$p_{21}^i = p_{21}^{i-1} f_{11}(c_R^i, c_T^i) + p_{22}^{i-1} f_{21}(c_R^i, c_T^i) \quad (4.8)$$

$$p_{22}^i = p_{21}^{i-1} f_{12}(c_R^i, c_T^i) + p_{22}^{i-1} f_{22}(c_R^i, c_T^i), \quad (4.9)$$

where the base case is given as

$$p_{11}^0 = p_{22}^0 = 1 \quad (4.10)$$

$$p_{12}^0 = p_{21}^0 = 0. \quad (4.11)$$

Here, the distributions $f_a(c_R^i, c_T^i)$ and $f_b(c_R^i, c_T^i)$ are closely related to the count probability distributions used in the thresholding method. Indeed, f_{22} is nothing but the first term of p_{F2} in equation 4.3, when the detection time T is replaced by the binning time T_{bin} :

$$f_{22}(c_R, c_T) = e^{-T_{\text{bin}}/\tau_{F2}} \lambda(c_R, T_{\text{bin}} \cdot \Phi_{F2}^R) \lambda(c_T, T_{\text{bin}} \cdot \Phi_{F2}^T) \quad (4.12)$$

Equally, f_{21} corresponds to the second term in p_{F2} :

$$f_{21}(c_R, c_T) = \int_0^{T_{\text{bin}}} \frac{e^{-t_d/\tau_{F2}}}{\tau_{F2}} \lambda(c_R, (T_{\text{bin}} - t_d) \cdot \Phi_{F1}^R + t_d \cdot \Phi_{F2}^R) \dots \lambda(c_T, (T_{\text{bin}} - t_d) \cdot \Phi_{F1}^T + t_d \cdot \Phi_{F2}^T) dt_d \quad (4.13)$$

The equivalent holds for f_{11} and f_{12} with respect to p_{F1} .

The recursion is continued until bin N , where N is defined such that the stopping condition

$$\left| \log_{10} \left(\frac{p_{11}^N + p_{12}^N}{p_{21}^N + p_{22}^N} \right) \right| < \delta \quad (4.14)$$

holds. This condition is a measure of the certainty with which the recursion has led to the correct result. δ is chosen such that $10^{-\delta}$ is much smaller than the expected detection error. In our case, $\delta = 6$ is suitable, since we expect a detection error on the order of 10^{-4} . Additionally, a maximum number of bins N_{max} is defined, and the recursion is stopped if the stopping condition is not reached after N_{max} bins.

The detection time necessary for the maximum likelihood method varies, since the number of bins N necessary to reach the stopping condition varies with each individual trace. It is therefore possible in principle to define an effective mean detection time (see [59]) which can be shorter than the optimum detection time for the thresholding method. Here however, we define the detection time as given by N_{max} , since for many practical applications a fixed detection time is advantageous for timing purposes.

4.3. Experimental results

4.3.1. Measurement of the detection efficiency

The detection error of both the thresholding and maximum likelihood detection methods depend on hyperfine state lifetimes and mean count rates. The measurement of these parameters was presented in section 3.4.2. The probe pump power is chosen to be low enough to not saturate either the APDs or the atom. Under these conditions, count rates in transmission are $\Phi_{F1}^T = 1.8 \times 10^5$ counts per second for an atom in $F = 1$, and $\Phi_{F2}^T = 1.3 \times 10^3$ counts per second for an atom in $F = 2$. The count rates in reflection are $\Phi_{F=1}^R = 4.3 \times 10^5 \text{ s}^{-1}$ and $\Phi_{F2}^R = 8.8 \times 10^5 \text{ s}^{-1}$. Both APD's are read-out with a binning time of $4 \mu\text{s}$. The hyperfine state lifetimes are $\tau_{F2} = 52 \text{ ms}$ and $\tau_{F1} = 26 \text{ ms}$. With these numbers, we calculate the overlap of the expected count distributions, and thereby the detection error of the thresholding method according to equation 4.3. We obtain $\epsilon_{F1} = 7.0 \times 10^{-4}$ and $\epsilon_{F2} = 9.1 \times 10^{-4}$, and the total detection error is $\epsilon = 8.0 \times 10^{-4}$ at the optimum detection time of $60 \mu\text{s}$. The associated expected count distributions are shown in figure 4.4 (left panels).

To obtain the detection error expected from the maximum likelihood method, we use a Monte-Carlo algorithm to generate artificial "detection traces" on which we then apply the maximum likelihood recursive algorithm. The resulting detection errors are $\epsilon_{F1,ML} = 4.8 \times 10^{-4}$, $\epsilon_{F2,ML} = 4.9 \times 10^{-4}$ and $\epsilon_{ML} = 4.9 \times 10^{-4}$. We set the maximum number of bins N_{max} to 25, since a larger N_{max} does not further decrease the detection error. The detection time for this method is therefore $100 \mu\text{s}$. At the cost of a longer detection time, the maximum likelihood method is able to reduce the detection error by approximately 40%.

In order to experimentally confirm the errors of both readout methods, we have to prepare a single atom in a well-defined hyperfine state before applying either detection method. For this, we load a single atom into the dipole trap and continuously monitor cavity transmission until the atom is lost. The observation of transmission below a lower (above a higher) threshold signals a successful preparation in $F = 2$ ($F = 1$). Two different thresholds are used to minimize preparation error: To signal the preparation of an atom in $F = 2$, we integrate over $72 \mu\text{s}$ and use threshold 1, for $F = 1$ we integrate over $24 \mu\text{s}$ and use a lower threshold of 2 counts. The choice of integration times T_{prep} and threshold is made to minimize preparation errors while maximizing the probability of successful preparation. With the chosen parameters, 85% of the preparation attempts lead to a successful state preparation.

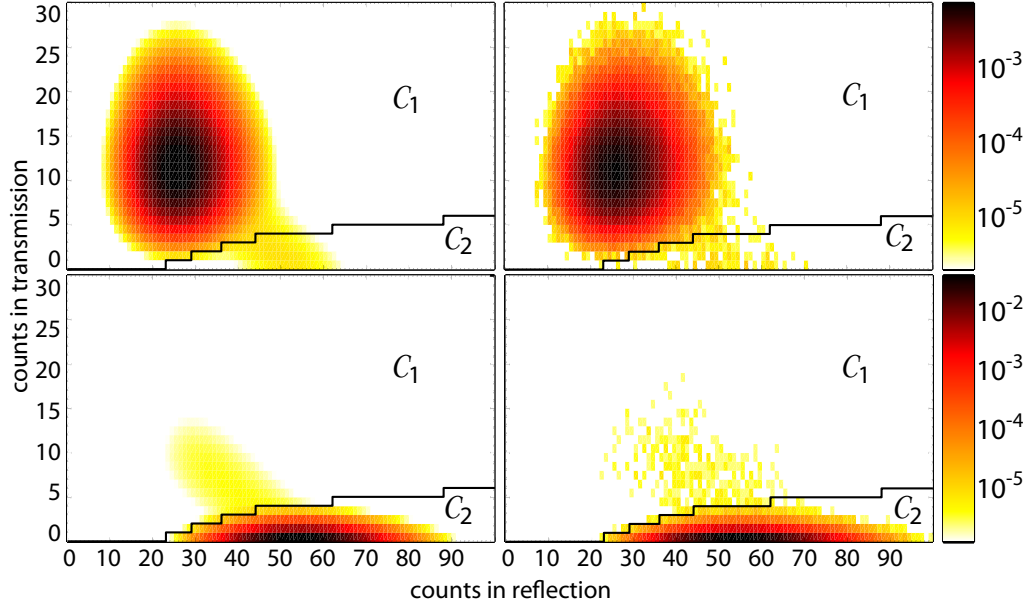


Figure 4.4.: Two-dimensional distributions of counts registered during $60 \mu\text{s}$ in reflection and transmission with an atom prepared in $F = 1$ (upper graphs) and $F = 2$ (lower graphs). The left graphs are calculated distributions. The right graphs show the experimentally measured distributions. Note that the data are plotted on a logarithmic scale. The solid black lines represents the threshold used to differentiate $F = 2$ from $F = 1$ atoms.

Preparation error arises due to photon shot noise and depumping. The contribution due to shot noise for the preparation of the $F = 2$ state is given by $\lambda(0, 72 \mu\text{s} \cdot \Phi_{F1}^T) = 2.0 \times 10^{-6}$, for the preparation of the $F = 1$ state by $\sum_{i>3} \lambda(i, 24 \mu\text{s} \cdot \Phi_{F2}^T) = 4.3 \times 10^{-8}$. Both of these are negligible.

The contribution due to depumping during the preparation time is calculated similarly. The count distribution in transmission for the case that an atom initially in state $F = 2$ ($F = 1$) is depumped during the preparation time is given by $p_{F2}(c_T)$ (resp. $p_{F1}(c_T)$):

$$p_{F2}(c_T) = \int_0^{T_{\text{prep},F2}} \frac{e^{-t/\tau_{F2}}}{\tau_{F2}} \lambda(c_T, (T_{\text{prep},F2} - t) \cdot \Phi_{F1}^T + t \cdot \Phi_{F2}^T) dt \quad (4.15)$$

$$p_{F1}(c_T) = \int_0^{T_{\text{prep},F2}} \frac{e^{-t/\tau_{F1}}}{\tau_{F1}} \lambda(c_T, (T_{\text{prep},F2} - t) \cdot \Phi_{F2}^T + t \cdot \Phi_{F1}^T) dt, \quad (4.16)$$

similarly to equation 4.3. The preparation error for the $F = 1$ state is therefore dominated by depumping and given by $\sum_{i>3} p_{F1}(i) = 3.5 \times 10^{-4}$. For the $F = 2$ state, this term is given by $p_{F1}(0) = 2.0 \times 10^{-6}$.

We can repeat the preparation-detection cycle many times on each single atom prepared in the dipole trap. On average, more than 1000 preparation-detection cycles are performed on each atom. Table 4.1 shows the measured and calculated detection errors. As expected, the maximum likelihood method gives the best detection fidelity of 99.93%.

	threshold calculated	threshold measured	maximum likelihood calculated	maximum likelihood measured	prepa- ration
ϵ_{F1}	7.0	11.4 ± 0.6	4.8	9.1 ± 0.6	3.5
ϵ_{F2}	9.1	9.0 ± 0.5	4.9	5.7 ± 0.4	≈ 0
ϵ	8.0	10.2 ± 0.4	4.9	7.4 ± 0.3	

Table 4.1.: Calculated and measured hyperfine state readout errors for the thresholding method and the maximum likelihood method. All numbers have to be multiplied by 10^{-4} . Uncertainties are statistical. The last column gives preparation errors.

The measured thresholding fidelity is 99.9%, close to the prediction of the model. The difference between the calculated and measured fidelities is mostly accounted for by the state preparation error. The runs in which more than one error were prepared affect the error only at the level of 10^{-5} .

Figure 4.4 shows the comparison between the calculated and measured probability distributions of counts from which we extract the errors for the thresholding method. The tails that make up the dominant contribution to the detection error are clearly visible on both the measured data and the calculation. Figure 4.5 shows the same data as one-dimensional histograms, with transmission and reflection shown in separate panels. Again, a very good agreement between theory and measurements is found. In the reflection signal, it can be seen that the measured count distributions are slightly super-poissonian. We attribute this to long-term probe power fluctuations of around 5%. These fluctuations lead to a larger measured detection error when compared to the error calculated from the ideal distributions. The same probe power fluctuations of course are present in the transmission measurements, however they are not resolved there since their effect is smaller than shot noise. Since the hyperfine state preparation is based solely on transmission counts, it is not affected by the fluctuations.

4.3.2. Time dependency of the detection efficiency

The detection times of our scheme of $60 \mu\text{s}$ - $100 \mu\text{s}$ are smaller than typical fluorescence detection times, which are upwards from $400 \mu\text{s}$ [59]. Many experiments could benefit from even faster detection rates. In quantum information experiments with single ions, gate times are usually faster than the time required for detection [123], such that the cycling time could be increased by a faster detection. Detection times in the sub- μs range are also desirable for the realization of loophole-free Bell test ([107]). To close both the "locality loophole" and the "detection loophole", fast and high-finesse detectors are necessary.

For constant probe power, simply decreasing the integration time leads to a rapidly increasing detection error, which quickly becomes dominated by photon shot noise. The time dependence of the detection error for our parameters is shown in figure 4.6. As expected, the detection error increases when detection time is lower than the optimum.

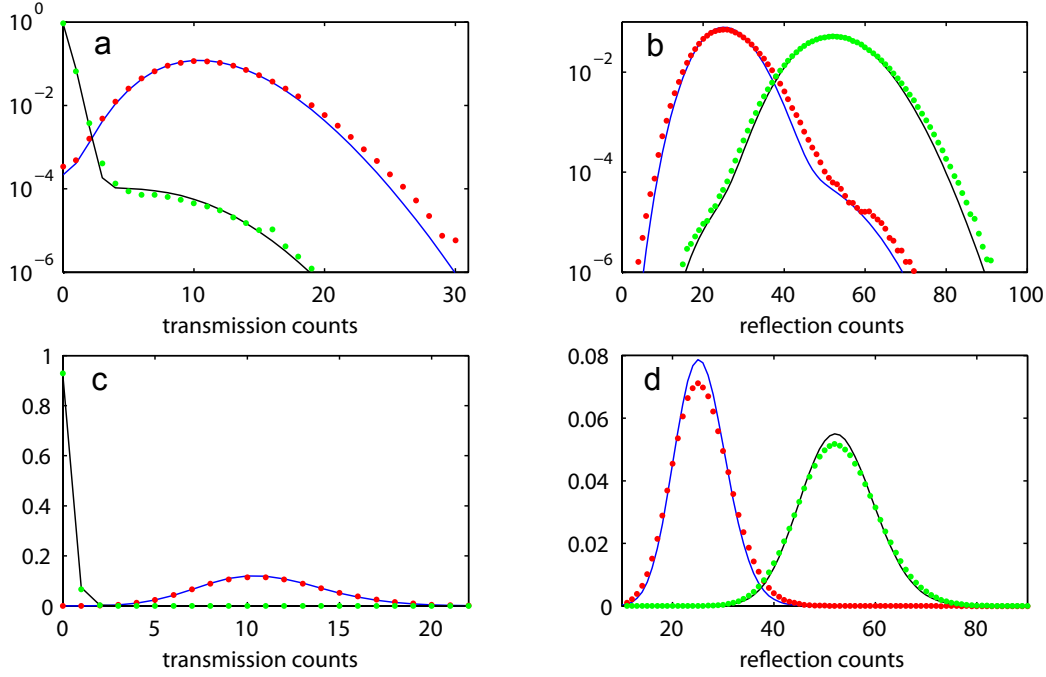


Figure 4.5.: Count distributions in transmission (a and c) and in reflection (b and d), with logarithmic y-axis (a and b) and linear y-axis (c and d), obtained from the data in 4.4. Measurement time is $60 \mu\text{s}$. Red (green) circles are measured distributions for an atom initially in hyperfine state $F = 2$ ($F = 1$). Lines are theoretical curves, constituted by a Poisson distribution with a tail caused by depumping. Parameters used for the theoretical curves are measured mean count rates and lifetimes. The measured distributions follow theory closely. In the reflection signals, the measured distributions are seen to be slightly broader than Poissonian. The difference is mainly due to light power fluctuations in the probe laser. This effect is less visible in transmission due to the lower mean count rates and consequently larger relative shot noise.

The largest deviation between theory and measurements is in the time range where the count distribution broadening due to probe power fluctuations lead to an increase in the measured detection error. Overall, the agreement between theory and measurement is good. However, for detection times on the order of microseconds, the error increases to above 10%.

To decrease detection time while avoiding large detection errors, probe power has to be increased. Figure 4.7 shows the calculated and measured count distributions for a detection time of $2 \mu\text{s}$. The detection time of $2 \mu\text{s}$ corresponds to the clock rate of the counter we use to read the APD clicks, and could easily be further reduced using faster electronics.

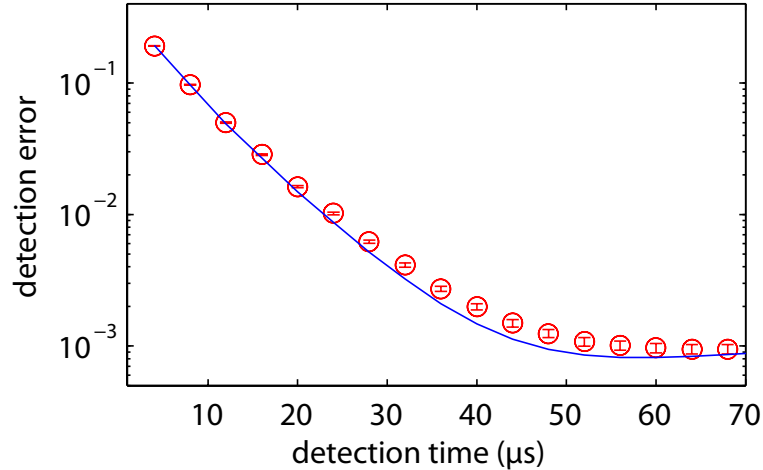


Figure 4.6.: Detection error versus detection time for the thresholding method, with constant probe power. The blue line is the result of the model, the red points are measured data with 1σ errorbars. An optimum detection time exists for which the detection error is minimized. For our parameters, this happens at $60 \mu\text{s}$. Integrating for less than this optimum time deteriorates the detection finesse.

While this detection time is 30 times shorter than before, we use a probe power increased by a factor of 60 to counteract saturation effects (see below). This leads to transmission count rates of $7.6 \times 10^6 \text{ s}^{-1}$ ($4.4 \times 10^5 \text{ s}^{-1}$) for an atom in $F = 1$ ($F = 2$) and reflection count rates of $9.2 \times 10^6 \text{ s}^{-1}$ ($1.3 \times 10^7 \text{ s}^{-1}$). Hyperfine state lifetimes are $\tau_{F1} = 460 \pm 50 \mu\text{s}$ and $\tau_{F2} = 205 \pm 50 \mu\text{s}$. The measured detection error is $\epsilon = 6.1 \pm 0.7 \times 10^{-3}$, in agreement with the prediction from the model of 5.7×10^{-3} .

The increase in detection error with higher probe power is due to various factors. First, our APD has a dead time of 53 ns. The APD detection efficiency therefore decreases with light power and saturates at 1.5×10^7 counts/s. Appendix A.2 gives the correction factor by which the detection efficiency decreases as a function of count rate. At the maximum count rate reached here ($1.3 \times 10^7 \text{ s}^{-1}$ on the reflection APD), the correction factor is 3.5. The overlap between the $F = 1$ and $F = 2$ detection histograms is increased by this effect.

Second, the extinction ratio of the cavity transmission Φ_{F2}^T/Φ_{F1}^T decreases with increasing probe power, even when correcting for the APD non-linearity. In this measurement, $\Phi_{F2}^T/\Phi_{F1}^T = 3.6\%$, compared to the value of 0.7% in the low-power measurement. The $F = 2$ lifetime decreases with the same non-linearity due to a higher scattering rate, further increasing the detection error. In spite of these negative effects, our result shows a high-fidelity read-out at a detection times orders of magnitude below previous results.

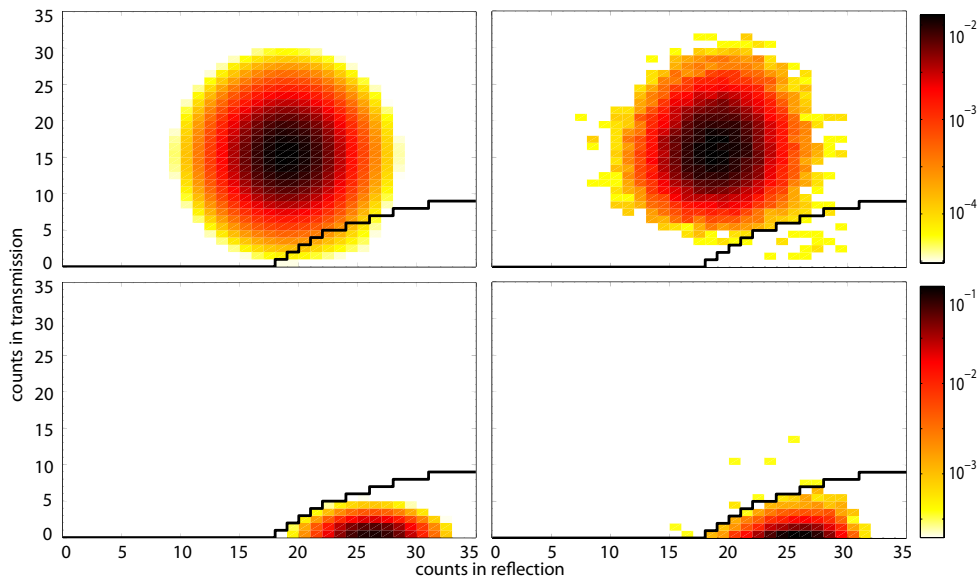


Figure 4.7.: Two-dimensional distributions of counts registered during $2 \mu\text{s}$ in reflection and transmission with an atom prepared in $F = 1$ (upper graphs) and $F = 2$ (lower graphs). The left graphs are calculated distributions. The right graphs show the experimentally measured distributions. Note that the data are plotted on a logarithmic scale. The solid black lines represents the threshold used to differentiate $F = 2$ from $F = 1$ atoms.

4.4. Conclusion

This chapter explored the capabilities of the FFP to act as a high-fidelity hyperfine state detector of single atoms. For detection times of $100 \mu\text{s}$, a detection fidelity of 99.93% was measured, making the detection scheme suitable for applications in quantum information processing with neutral atoms. Since the detection is not based on scattering, it is non-destructive and the atom remains trapped during the measurement. Additionally, the hyperfine state of the atom is preserved during the measurement, enabling the deterministic preparation of single atoms in the desired hyperfine state.

Shorter detection times are possible, potentially well below the microsecond range. In a detection time of $2 \mu\text{s}$, limited by the counter clock rate, the detection fidelity obtained is 99.4%. The fundamental limit for detection time is on the order of $1/\kappa$, which for our system is 3 ns.

5. Measurement backaction

So far we have shown that the FFP cavity is perfectly suited as a state-dependent atom detector with very high measurement fidelity. Fidelity is one of the most important characteristics of a measurement device, especially in the field of quantum computation. Another important aspect in measurements is backaction, the change caused by the measurement on the measured system. The study of backaction has merits due to it being one of the fundamental concepts in quantum mechanics, but it also has practical implications. Indeed, many quantum measurements cause a much stronger backaction than required by the laws of quantum mechanics. Irreversible energy exchange and heating typically results from this.

For the detection of single ions, the method most commonly used is the shelving technique. It is based on the collection of resonance fluorescence emitted by the atom excited by a laser. In this section, we will investigate the amount of scattering our detection method causes, and compare the result to the shelving technique, and more generally all free space detection methods using light. We give the factors that limit our system and show how these limits could be overcome. Furthermore, we demonstrate a quantum Zeno effect and show how it allows us to determine the minimum backaction a measurement causes and how strongly each photon incident on the cavity collapses the state of the atom.

5.1. Information gain and scattering in cavities and in free space

5.1.1. The minimum detection error

It will be useful for the rest of the chapter to introduce a framework that allows to determine the minimum error a certain measurement method is capable of, along with the backaction it causes. We will concentrate on the measurement of a single atomic qubit. It will become clear that what we consider to constitute a measurement is the establishment of a correlation between the qubit and the environment such that it becomes possible to deduce the qubit state with some accuracy when the state of the environment is known.

Note that what we are concerned with here is not the determination of the exact qubit state $\alpha|0\rangle + \beta|1\rangle$. Quantum mechanics tells us that in order to precisely measure $|\alpha|$ and $|\beta|$ (supposing we are only interested in populations of the states, we neglect the phase component), an infinite number of projective measurements are required, each of which provides the experimenter with a binary result of either 0 or 1. The mean of the measured values then gives an approximation to $|\alpha|$ resp. $|\beta|$. This argument assumes the

complete projection of the qubit onto the eigenstates $|0\rangle$ and $|1\rangle$ by each measurement. In actual experiments however, this projection in general is not perfect. Here, as in the previous chapter, we are concerned with the quantification of the measurement error in a single projective measurement, i.e. the error to measure the qubit in $|1\rangle$ even though it was in $|0\rangle$, and vice versa. This error is accompanied by a non-perfect projection by the measurement, as we will show in this section.

In the first step of a measurement, the qubit to be measured becomes entangled with another quantum object. This object is often called the 'meter', and we will use this nomenclature even though the meter here is not necessarily macroscopic. In our case for example, the meter is a photon field that may contain only a few photons. The entanglement between the qubit and the meter is created by an interaction between the two. We denote the meter state before the interaction as $|\Psi_{\text{in}}\rangle$, and its final state after interaction as either $|\Psi_0\rangle$ or $|\Psi_1\rangle$ (depending on whether the qubit is in state $|0\rangle$ or $|1\rangle$). An initial state $(\alpha|0\rangle + \beta|1\rangle) \otimes |\Psi_{\text{in}}\rangle$ evolves into $\alpha|0\rangle \otimes |\Psi_0\rangle + \beta|1\rangle \otimes |\Psi_1\rangle$. The readout of the qubit state therefore amounts to distinguishing the meter states $|\Psi_0\rangle$ and $|\Psi_1\rangle$. In general, these states are nonorthogonal, and can therefore only be distinguished with some detection error ϵ , where $\epsilon = (\epsilon_0 + \epsilon_1)/2$, defined as in chapter 4. Again, we assume no prior knowledge on the qubit state.

The minimum possible error ϵ_H when distinguishing two quantum states is given by the Helstrom bound ([124]), defined as

$$\epsilon_H = \frac{1}{2} \left(1 - \sqrt{1 - |\langle \Psi_0 | \Psi_1 \rangle|^2} \right) \quad (5.1)$$

Note that the Helstrom bound depends solely on the overlap of the two quantum states to be distinguished. For zero overlap, the error goes to zero, whereas for states with overlap approaching unity the minimum error approaches $1/2$. $\epsilon = 1/2$ is also the error one can obtain from guessing the state. Here, we are concerned with the measurement of a qubit by a coherent light pulse, such that $|\Psi_{\text{in}}\rangle$ is a coherent light pulse containing n photons on average. To good approximation, the two final states $|\Psi_0\rangle$ and $|\Psi_1\rangle$ then also consist of coherent states. As an example, consider the generic case of a qubit to be measured using an ideal fluorescence scheme (see figure 5.1 c). The qubit has one completely dark state $|0\rangle$ which does not interact with the incoming pulse $|\Psi_{\text{in}}\rangle$, and one bright state $|1\rangle$ which scatters all photons. The final states of the light field after interaction with the qubit therefore are $|\Psi_0\rangle = |0\rangle_S |n\rangle_T$ and $|\Psi_1\rangle = |\sqrt{n}\rangle_S |0\rangle_T$. We use the notation $|\sqrt{n}\rangle$ for a coherent pulse containing on average n photons, and subscripts S and T to denote the scattered and transmitted light modes. The overlap $|\langle \Psi_0 | \Psi_1 \rangle|^2$ is given by the formula valid for all coherent states $|\alpha\rangle$ and $|\beta\rangle$ (with mean photon number $|\alpha|^2$ and $|\beta|^2$)

$$\langle \beta | \alpha \rangle = e^{-\frac{1}{2}(|\alpha|^2 + |\beta|^2 - 2\alpha\beta^*)}, \quad (5.2)$$

and therefore

$$|\langle \Psi_0 | \Psi_1 \rangle|^2 = \exp(-2n). \quad (5.3)$$

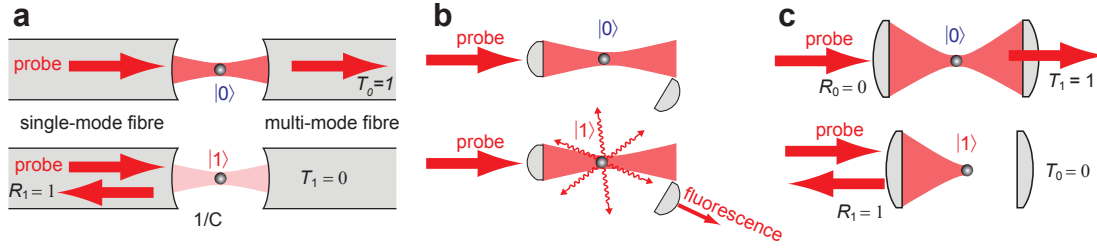


Figure 5.1.: Comparison of different qubit detection methods. a) The cavity detection, using transmitted and reflected light. b) Shelving technique or fluorescence imaging. When the atom is in the resonant state $|1\rangle$, some of the incoming photons are scattered. Due to a limited collection efficiency, only a part of the scattered photons are collected. c) Ideal shelving technique. Lenses with a collection solid angle of 2π are used on both sides of the atom. Under these circumstances, the atom acts as a mirror when it is in the resonant state. When the atom is in the off-resonant state, all light is transmitted.

The Helstrom bound for an ideal fluorescence measurement therefore is

$$\epsilon_H = \frac{1}{2} \left(1 - \sqrt{1 - e^{-2n}} \right) \stackrel{n \gg 1}{\approx} \frac{e^{-2n}}{4} \quad (5.4)$$

The minimum detection error decreases exponentially with the number of photons in the measurement pulse and quickly becomes small.

The exact same results holds true for a cavity based detection scheme with resonant light, as illustrated in figure 5.1 a). Here, photons reflected by the cavity take the role of the scattered photons in ideal fluorescence imaging. In an ideal version of cavity based detection, an atom in the non-resonant state $|0\rangle$ has negligible effect on the cavity, and all photons from the incident mode are transmitted, such that $|\Psi_0\rangle = |0\rangle_R |\sqrt{n}\rangle_T$. By contrast, an atom in the resonant state $|1\rangle$ detunes the cavity by more than its linewidth and all photons are reflected, such that $|\Psi_1\rangle = |\sqrt{n}\rangle_R |0\rangle_T$. Equations 5.2 and 5.4 therefore are valid also for ideal cavity based detection schemes, and the minimum detection error decreases exponentially with the number of photons.

This result is true not only for the ideal schemes considered so far. All schemes that use coherent probe pulses that are redistributed into different modes by the interaction with the atom show this exponential decrease in the Helstrom bound, albeit with different decay rates. In general, the outgoing light field can be approximated by the tensor product of coherent fields,

$$|\Psi_0\rangle = \bigotimes_m |\alpha_0^m \sqrt{n}\rangle \quad (5.5)$$

$$|\Psi_1\rangle = \bigotimes_m |\alpha_1^m \sqrt{n}\rangle, \quad (5.6)$$

where $|\alpha_i^m|^2$ is the fraction of photons redistributed into mode m after interaction with the qubit state i . In analogy to equation 5.2, the overlap of the outgoing light field then

is

$$|\langle \Psi_0 | \Psi_1 \rangle|^2 = e^{-\zeta n}, \quad \zeta = \sum_m (\alpha_0^m - \alpha_1^m)^2. \quad (5.7)$$

The Helstrom information

Equation 5.7 tells us that in general, the minimum error that is possible in a measurement decreases exponentially with the number of photons used for the measurement. This leads to a heuristic definition of a quantity defined as the logarithm of ϵ ,

$$I \equiv -\ln 2\epsilon. \quad (5.8)$$

We will refer to this quantity as "information", since it increases as the uncertainty about the measured state decreases. The maximum information I_{tot} (or equivalently, the minimum error) one can obtain from a measurement is related to the minimum detection error as

$$I_{\text{tot}} = I_H \equiv -\ln 2\epsilon_H. \quad (5.9)$$

This is the information that has leaked out of the system during the measurement as a function of the photons used for the measurement. I_{tot} constitutes an upper bound to the information I_{acc} that an experimenter can actually obtain. In order to achieve the detection error associated with I_{tot} , one would need to have a means to precisely measure the overlap of the final light state.

In the following, we use the notation of the "Helstrom information"

$$I_H(\zeta n) = -\ln \left(1 - \sqrt{1 - e^{-\zeta n}} \right) \stackrel{n \gg 1}{\approx} \zeta n. \quad (5.10)$$

to define the information a measurement system delivers whose final light states have an overlap of $e^{-\zeta n}$.

The word "information" is used in the sense common in binary hypothesis testing [125]. It has a value between zero and infinity. The meaning of the word here is therefore quite different from the more usual definition according to which there is exactly one classical bit of information in a qubit.

5.1.2. Backaction and scattering

In many situations an experimenter not only wants to maximize his information gain (or equivalently, his certainty about the state of the measured system), but also minimize the backaction of the measurement on the system. Quantum mechanics requires that the measured system becomes projected during the measurement, as can be seen easily on the example considered just above. The interaction between the meter and the qubit leads to an evolution of the total state as $(\alpha|0\rangle + \beta|1\rangle) \otimes |\Psi_{\text{in}}\rangle \rightarrow \alpha|0\rangle \otimes |\Psi_0\rangle + \beta|1\rangle \otimes |\Psi_1\rangle$. The effect on the qubit itself is obtained by tracing over the meter after the measurement interaction. The final state of the qubit described by its density matrix ρ_f then is

$$\rho_f = \begin{pmatrix} |\alpha|^2 & \alpha\beta^* \langle \Psi_0 | \Psi_1 \rangle \\ \alpha^*\beta \langle \Psi_1 | \Psi_0 \rangle & |\beta|^2 \end{pmatrix} \quad (5.11)$$

This decrease in the coherence of the qubit is what is called the quantum state projection. In an ideal measurement, $|\Psi_0\rangle$ and $|\Psi_1\rangle$ are orthogonal, and the measurement completely annihilates the qubit's coherence.

The Helstrom bound tells us that the total information extracted from the system is ultimately limited by the overlap of the two possible meter output states. Equation 5.11 shows that the projection of the system is given by the same overlap, and there is a direct relation between information obtainable by the experimenter, expressed by I_H in equation 5.9, and the projection of the qubit: The strength of the projection of the atom increases when the total information extracted from the system increases.

The state projection required by quantum mechanics does not affect the system in any way except by reducing its coherence. In particular, for a qubit encoded in the internal state of an atom, no external degrees of freedom of the atom are necessarily affected by the measurement. However, many experimental techniques actually lead to a much higher, and often undesirable, effect on the atom. Unlike the intrinsic state projection, this additional backaction is not limited to the degrees of freedom that are being measured. In the case of optical read-out schemes for atomic system, this additional backaction typically is due to spontaneous emission of photons and leads to heating.

Spontaneous emission is easily quantifiable in the example of the ideal fluorescence measurement considered above. By definition, each incident photon is scattered when the atom is in the bright state. We can restate the Helstrom bound in terms of scattered photons m by noting¹ that in this case, $n = m$ and therefore

$$I_{\text{tot}} = I_H(2m) \approx 2m \quad (5.12)$$

While this limit is no surprise for fluorescent detection, it also holds for a much larger class of measurements. A general lower bound for spontaneous emission during optical detection of atoms was shown to exist by Hope in [126]: The information obtained in either absorption or phase shift measurements are both equally limited by spontaneous emission, since no phase shift can be imprinted on the light without excited state population. According to this result, equation 5.12 holds true as long as the following conditions are fulfilled: The meter is a classical light source, and the light passes the atom only once. We will refer to this sort of measurements as "free-space measurements", as opposed to cavity measurements.

Scattering-free detection in a cavity

A cavity is not a single-pass device. In a simple picture of a Fabry-Pérot cavity, a photon passes an atom in the cavity \mathcal{F} times before it is lost through the cavity mirrors. This allows a cavity-based detection scheme to overcome the limit from equation 5.12. In the cavity-based scheme, an atom in the resonant state $|1\rangle$ prevents the light from entering the cavity. This reduces the intracavity intensity by a factor $1/4C^2$ compared to the

¹Since we neglect scattering from the off-resonant dark state, we quantify scattering in terms of photons scattered when the atom is in the bright state, the quantity we denote by m . Under the assumption that the qubit is with equal probability in $|0\rangle$ or $|1\rangle$, the average number of scattered photons in a measurement is $m/2$.

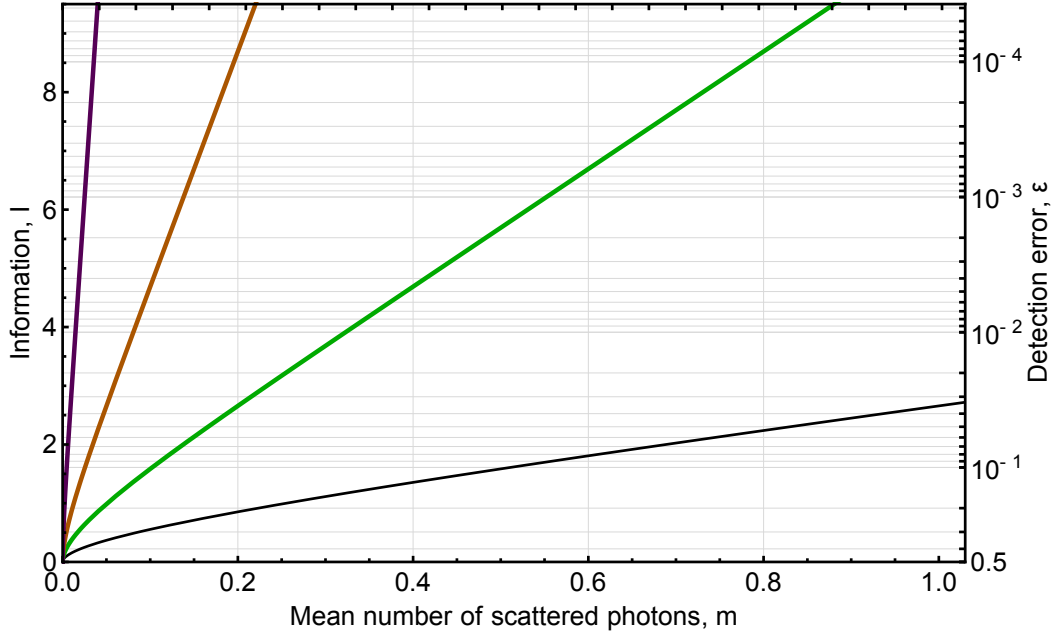


Figure 5.2.: The Helstrom bound of free-space and cavity based detection. The black curve is the Helstrom bound for free-space (e.g. fluorescence) detection. The green, orange and purple curves correspond to the Helstrom bound for a cavity-based scheme with varying cooperativity of $C = 5, 20, 110$. The left axis shows the total information extracted, the right axis is the associated detection error. Note the inverted axis for the detection error. All curves assume that the non-resonant dark state does not contribute to scattering.

empty cavity value, as we have calculated in the theory chapter (equation 1.28). This drastically reduces the scattering rate of the atom, a phenomenon already considered in the theory of optical bistability [65]. In the context of single atom detection, it was shown in [127] that an atom strongly coupled to a cavity scatters a fraction $1/C$ of the incident light power, a result also derived here (equation 1.30). In our terminology, we therefore have $m = n/C$. The total information per scattered photon is C times larger than in the free-space situation:

$$I_{\text{tot}} = I_H(2Cm) \approx 2Cm \quad (5.13)$$

The cooperativity C can become arbitrarily large, such that cavity based detection in principle can completely avoid spontaneous scattering. Figure 5.2 shows a comparison of the Helstrom bound for free-space and cavity qubit detection in terms of scattering probability.

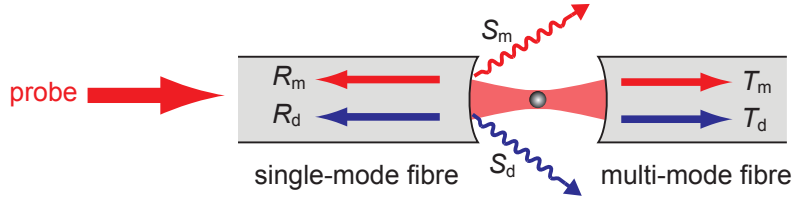


Figure 5.3.: The field modes into which the measurement light is redistributed. Due to the birefringence of the cavity mirrors, the field inside the cavity populates both the main (resonant) and the orthogonally polarized, detuned mode. Accordingly, the outgoing light is characterized by the coupling factors to the different modes, $\alpha \in \{T_m, R_m, S_m, T_d, R_d, S_d\}$, where α depends on the qubit state. Here, scattering by the atom is neglected.

5.2. Non-ideal cavities and measurements

The Helstrom bound determines the minimum backaction the measurement has on the qubit, and it gives a lower bound to the detection error an experimenter can hope to achieve. So far, we only considered idealized measurement situations that do not directly correspond to actual implementations. In the following, we address the different factors that lead to reductions in the total information due to the characteristics of our cavity. Furthermore, some of the information contained in the Helstrom bound is not accessible to the experimenter. The accessible information I_{acc} is smaller than I_{tot} , and we will characterize which factors limit I_{acc} .

5.2.1. Helstrom bound for our cavity

The total information I_{tot} is reduced when using realistic cavities due to finite intra-cavity intensities even when the qubit is in the resonant state $|1\rangle$, as well as due to non-perfect mirrors. In our cavity, the second polarization mode also has to be taken into account. Due to these effects, the outgoing field can be written as a tensor product of six coherent fields (see equation 5.5), accounting for the components of the loss channels and the second cavity mode. The outgoing fields have amplitudes $\alpha_i \sqrt{n}$, where the subscript i denotes the qubit state. $\alpha \in \{t_m, r_m, s_m, t_d, r_d, s_d\}$ completely identifies the outgoing mode. m and d designate the main (resonant) and detuned cavity mode, and t , r , and s are the mode coupling factors for transmitted, reflected and scattered light. Figure 5.3 gives an illustration of the outgoing field modes.

The overlap of the outgoing field then is calculated according to equation 5.7, leading to a total information $I_H(\zeta n)$. In our case, the phase shift between the states $|\Psi_1\rangle$ and $|\Psi_0\rangle$ can be neglected and the amplitude coupling factors $\{\alpha_i\}$ can be considered real.

The power coupling factors $\{\alpha_i^2\}$ in our case are (in percent) $\{\alpha_0^2\} = \{12.7, 41.4, 45.9, 0, 0, 0\}$ when the atom is in $|0\rangle$ and $\{\alpha_1^2\} = \{0.1, 99, 0.4, 0.1, 0.1, 0.4\}$ when it is in $|1\rangle$. The values for $\{\alpha_0^2\}$ are just the empty cavity transmission T_0 , reflection R_0 and losses L_0 . They are given by the mirror transmission $T_{\text{mir}} = 31$ ppm and scattering losses $L_{\text{mir}} = 56$

ppm by the formulas

$$T_0 = \frac{T_{mir}^2}{T_{mir}^2 + L_{mir}^2}, R_0 = \frac{L_{mir}^2}{T_{mir}^2 + L_{mir}^2}, S_0 = 1 - T_0 - R_0 \quad (5.14)$$

The power coupling factors $\{\alpha_1^2\}$ follow from the intracavity photon number in the two modes for an atom in $|1\rangle$. The total intracavity photon number is obtained from the measured cavity transmission for an atom in $|1\rangle$. The solution to the full master equation predicts an approximately equal population of the two cavity modes. Transmission and scattering of both modes are therefore equal and given by the mode population and T_{mir} L_{mir} .

From $\{\alpha_0\}$ and $\{\alpha_1\}$, we deduce $\zeta = 0.62$, such that we expect our cavity to extract a total information of $I_{tot} = I_H(0.62n) \approx 0.62n$. This corresponds to roughly one third of the ideal cavity case of $I_H(2n) \approx 2n$.

Of the total information I_{tot} , only a part is contained in the light modes that are accessible, i.e. in the optical fibers. The mode corresponding to scattering by the mirrors is lost. The accessible portion of the light is therefore characterized by $\alpha'_i \in \{t_m, r_m, t_d, r_d\}$, and the Helstrom bound corresponding to these outgoing light modes is $I_{acc} = I_H(0.23n) \approx 0.23n$. However, we can not obtain all of this information, since this would require to measure the complete quantum state of the outgoing fields.

5.2.2. Photon counting and the Chernoff information

We use photon counting on the transmitted and reflected light, which is not an optimal strategy to distinguish $|\Psi_0\rangle$ and $|\Psi_1\rangle$. I_{acc} is therefore reduced even further. The information accessible through photon counting is given by the overlap of the two (classical) probability distributions P_0 and P_1 , where P_0 (P_1) is the probability distribution of detected counts if the atom is in $|0\rangle$ (respectively $|1\rangle$). The detection error is then given by the distance between the two distributions

$$\epsilon_D = \frac{1}{2}(1 - \|P_0 - P_1\|_1) \quad (5.15)$$

where the distance $\|P_0 - P_1\|_1$ is defined as

$$\|P_0 - P_1\|_1 = \sum_{\mathbf{x} \in (c_R, c_T)} \frac{|P_0(\mathbf{x}) - P_1(\mathbf{x})|}{2}. \quad (5.16)$$

We would like to express ϵ_D (and I_{acc}) as a function of n in order to be able to compare it to ϵ_H (and I_{tot}). According to Chernoff([125]), the error ϵ_D decays exponentially with n in the limit of large n , such that

$$\epsilon_D \approx Q_C \equiv \exp(-\xi_{CB}n), \quad (5.17)$$

where Q_C is the Chernoff coefficient given by

$$Q_C = \min_{0 \leq s \leq 1} \left[\sum_{\mathbf{x} \in (c_R, c_T)} P_0(\mathbf{x})^s P_1(\mathbf{x})^{1-s} \right]. \quad (5.18)$$

For the double Poissonian distributions P_0 and P_1 ξ_{CB} can be calculated to be

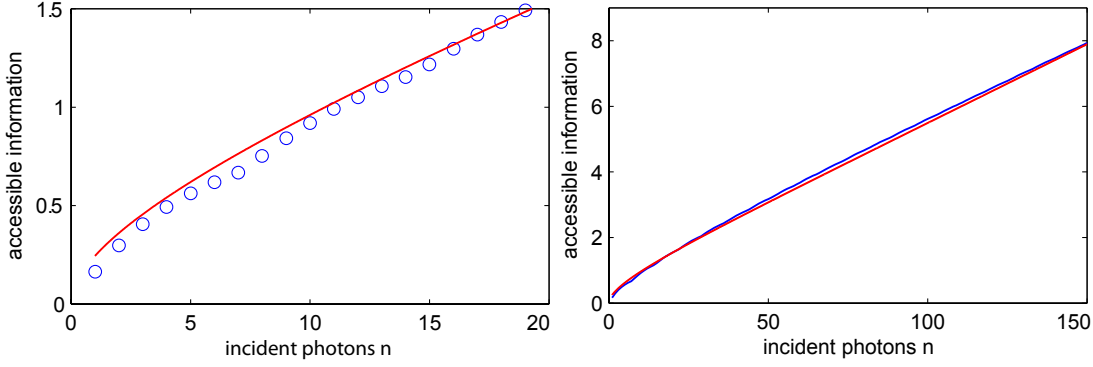


Figure 5.4.: The accessible information I_{acc} as a function of incident photon number n for two different ranges of incident photons. The blue circles (left) and blue line (right) show the numerical solution corresponding to Poisson count distributions in transmission and reflection. The red line is the approximation $I_{\text{acc}} = -\log(1 - (\sqrt{1 - \exp(-\xi_{CB}n)}))$ that asymptotically corresponds to the Chernoff bound $I_{\text{acc}} \approx \exp(-\xi_{CB}n)$. Note that the proposed function I_{acc} fits well also for small n .

$$\xi_{CB} = - \min_{0 \leq s \leq 1} [T_0^s T_1^{s-1} + R_0^s R_1^{1-s} - s(T_0 + R_0) - (1-s)(T_1 + R_1)]. \quad (5.19)$$

Chernoff's result shows that, in the limit of large n , the information accessible by photon counting increases linearly with the number of incident photons. This is identical to the behavior of I_{tot} obtained from the Helstrom bound.

What about the behavior for small n ? The distance $\|P_0 - P_1\|_1$ is well approximated by $\sqrt{1 - Q_C}$ even for small n . Figure 5.4 shows the numerically calculated I_{acc} alongside the function $I_H(\xi_{CB}n)$, and it shows good agreement between the two curves. To a good approximation, we can write

$$\epsilon_D = \frac{1}{2} \left(1 - \sqrt{1 - Q_C} \right). \quad (5.20)$$

Comparing this to equation 5.1, we see that in the case of photon counting, the Chernoff coefficient Q_C has the role of the state overlap in the Helstrom bound. We conclude that I_{acc} behaves the same way as I_{tot} as a function of n , allowing us to compare the two measures.

In the ideal case of no cavity losses and infinite cooperativity, $\xi_{CB} = 1$. Counting therefore allows to obtain at most half of the total information given by the Helstrom bound. The detection error can not be smaller than e^{-n} , which is just the probability that the coherent probe pulse does not contain a photon.

In our regime of parameters, the minimum in equation 5.19 is obtained for $s \approx 0.5$, leading to

$$\xi_{CB} = (T_0 + T_1 + R_0 + R_1)/2 - \sqrt{T_0 T_1} - \sqrt{R_0 R_1} = 0.11. \quad (5.21)$$

Using perfectly lossless optics and photodetectors in both transmission and reflection, we should thus be able to measure the qubit state with a detection error ϵ_D corresponding to the information $I_{\text{acc}} = I_H(0.11n)$. In our experiment, we have losses in optics and the APD's leading to total photon detection efficiencies of 47% in transmission and 31% in reflection. Taking these losses into account, we expect our detection method to yield $I_{\text{acc}} = I_H(4.6 \times 10^{-2}n)$.

5.2.3. Scattering in non-ideal cavities

Scattering of the resonant qubit state in our cavity differs from the ideal cavity due to two reasons: Losses due to imperfect cavity mirrors and mode-coupling, and the presence of the second cavity mode.

Mirror losses are accounted for in the empty cavity transmission T_0 . The resonant, empty intra-cavity power is reduced by the factor $\sqrt{T_0}$ (assuming the input and output mirrors are identical). In the weak-pumping limit, the same reduction applies to the intra-cavity power with the qubit present. The ratio of incoming to scattered photons, which is C in an ideal cavity, therefore increases to $n/m = C/\sqrt{T_0}$.

In order to determine the impact of the second cavity mode, we analyze the effect of the probe light on the atom. Pumping the system with π polarized detection light populates the excited state $|F' = 3, m_F = 0\rangle$. This state has two decay channels: spontaneous emission into free space with a rate Γ and emission into the second, orthogonally polarized cavity mode which is detuned by $\Delta_{bi} = 540$ MHz. The emission into the second cavity mode is enhanced by the Purcell effect and happens at a rate Γ_P . The effect of the second cavity mode is too strong to be treated as perturbation. We therefore numerically solve the full master equation to obtain the ratio of decay between the two decay channels. As result, we get $\Gamma_P = 2.6\Gamma$. The total scattering rate is therefore 3.6Γ , 3.6 times higher than in a single-mode cavity. The finally expected ratio of incoming to scattered photons therefore is $n/m = C/3.6\sqrt{T_0}$. Figure 5.5 presents an overview of the main differences between our cavity and an ideal cavity regarding I_{tot} and I_{acc} . Note that I_{tot} as a function of m for our cavity is limited primarily by the presence of the second mode. The accessible information on the other hand is reduced due to both optical losses and the second cavity mode compared to the ideal cavity case.

5.3. Experimental results: Scattering and accessible information

In this section, we experimentally measure the relation between the accessible information I_{acc} and the number of scattered photons m for a single atom coupled to the cavity. We start by showing how we experimentally implement a well-defined qubit in our system by achieving control over the Zeeman state of the atom. We then go on to measure the scattering rate of the atom under the action of probe light. Even though we have no access to the fluorescence photons, we can nevertheless measure the scattering rate by relating it to the rate of Zeeman state depumping. Finally, we are able to relate the

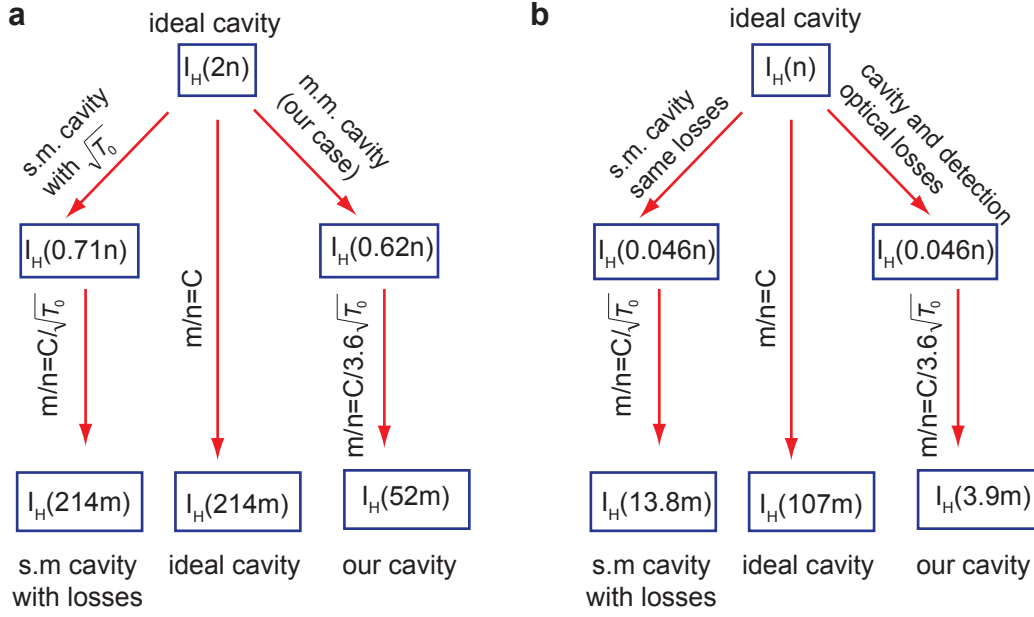


Figure 5.5.: I_{tot} (a) and I_{acc} (b) when APDs are used in ideal cavities and how losses and the second cavity mode influence the two quantities. The two top rows show results as a function of n , the bottom row as a function of m . All numbers are theoretical values.

detection fidelity of our qubit read-out, and therefore I_{acc} , to the number of scattered photons.

5.3.1. Experimental parameters

The qubit is implemented in the two states $|1\rangle = |F = 2, m_F = 0\rangle$ and $|0\rangle = |F = 1, m_F = 0\rangle$. The MW transition between the two states is insensitive to magnetic field fluctuations since neither state has a first-order Zeeman shift. For all measurements in this chapter, the higher frequency cavity polarization mode is tuned on resonance with the $|F = 2, m_F = 0\rangle \rightarrow |F' = 3, m_F = 0\rangle$ transition. A bias magnetic field on the order of 1 G is applied parallel to this polarization. Probe light is resonant to the cavity and atomic resonance, $\omega_p = \omega_c = \omega_a$. Both probe and dipole trap light are linearly polarized parallel to the resonant cavity mode's polarization. The probe light therefore resonantly drives π transitions between $|F = 2, m_F = 0\rangle$ and $|F' = 3, m_F = 0\rangle$ (see figure 5.6). The coupling constant of this transition is $g/2\pi = 185$ MHz. With $\kappa/2\pi = 53$ MHz and $\gamma/2\pi = 3$ MHz, this leads to a cooperativity of $C = 107$ for an atom in $|1\rangle$.

Unlike the experimental parameters used in chapter 4, these settings do not lead to an optimum hyperfine state detection error. Here, we use them because these settings allow us to measure the scattering rate of the atom via the depumping rate from $m_F = 0$, as shown in the next section. Additionally, the clock states are not subject to magnetic field fluctuations and therefore are an ideal candidate as a qubit.

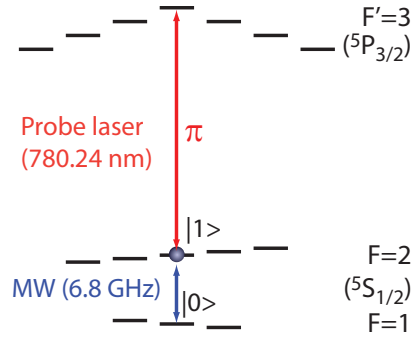


Figure 5.6.: Level scheme for the measurements presented in this chapter. The qubit is formed by the two clock states of the hyperfine ground state of ^{87}Rb . The qubit can be driven by resonant MW radiation. Both the cavity resonance and the π polarized probe laser are resonant to the $|F = 2, m_F = 0\rangle \rightarrow |F' = 3, m_F = 0\rangle$ transition.

5.3.2. Measurement of Zeeman state diffusion and scattering rate

A measurement of the scattering rate by collection of fluorescence photons would be difficult in our experiment since the atom is trapped at the center of the cavity mode, leaving only a small opening angle through which to collect light. Also, background contributions would be important due to the small expected fluorescence rate. We therefore measure the depumping rate from $|1\rangle$ caused by probe light, from which we can directly deduce the scattering rate.

We measure the rate of depumping from $|1\rangle$ as follows. After the preparation of a single atom in $|1\rangle$, we turn on a "depump pulse", i.e. probe light for a variable time. We then determine whether the atom has remained in $|1\rangle$ or has been depumped by using a Zeeman state sensitive detection. This uses the same principles as the Zeeman state preparation: We apply a π -pulse on the clock transition followed by a detection pulse. Only if the atom was in $|1\rangle$ before the π -pulse will the atom be found in $F = 1$ during the detection pulse. The transfer probability to $|0\rangle$ is therefore equal to the population remaining in $|1\rangle$ after the "depump" pulse.

We find that this survival probability decays exponentially with the number of incident photons at an initial rate ν , where $\nu^{-1} = 142 \pm 25$ photons (see figure 5.7). Note that the measured initial population of state $|1\rangle$ is 95%. The missing 5% arise from a combination of preparation and detection errors.

In order to determine the spontaneous scattering rate from the depumping rate, we analyze the effect of the probe light on the atom. We have discussed above the two decay channels of the state excited by the probe light, $|F' = 3, m_F = 0\rangle$: spontaneous emission into free space with a rate Γ and emission into the second, orthogonally ($\sigma^+ + \sigma^-$) polarized cavity mode which is detuned by $\Delta_{bi} = 540$ MHz, with a rate $\Gamma_P = 2.6\Gamma$. Spontaneous emission into free space is governed by the Clebsch-Gordan coefficients of

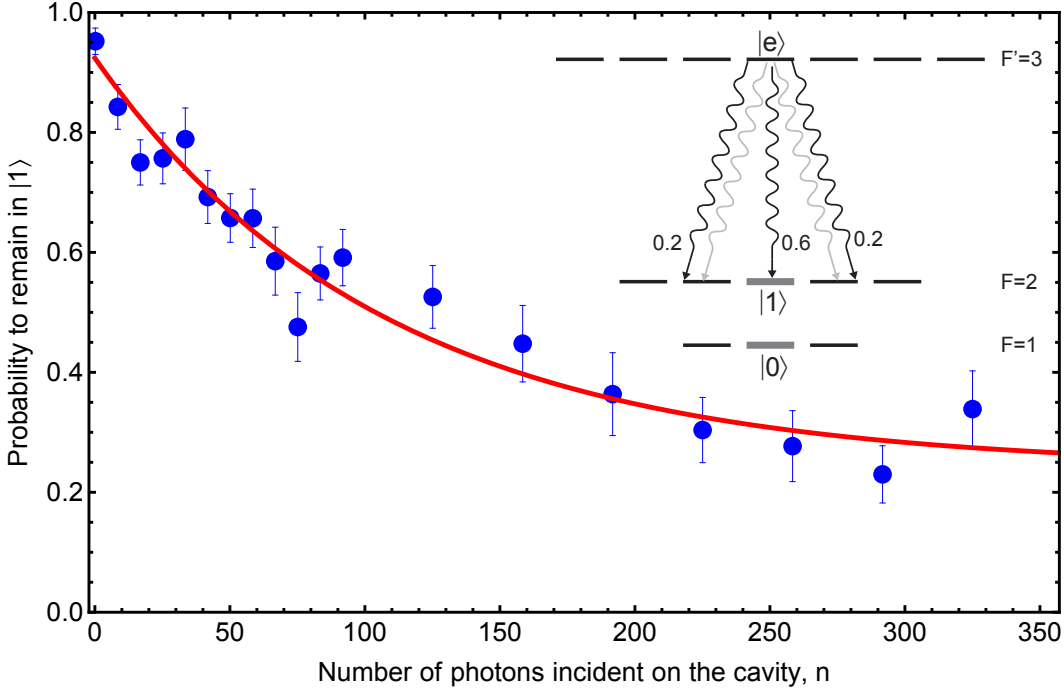


Figure 5.7.: Measurement of the Zeeman state diffusion rate out of state $|1\rangle = |F = 2, m_F = 0\rangle$ under the action of probe light. The probability to detect an atom in state $|1\rangle$ decays exponentially with the number of photons in the probe pulse with an initial rate ν , where $\nu^{-1} = 142 \pm 25$.

the respective transitions. The decay into the second cavity mode always leads to a change of the atomic Zeeman state, while for the decay into free space the probability to fall back into the original state $|1\rangle$ is $3/5$. Therefore, we obtain the ratio of incident photons to scattered photons as $n/m = \nu^{-1} \times (\Gamma_P + 2\Gamma_P/5)/(\Gamma_P + \Gamma) = 118 \pm 20$. This is compatible with the theoretical prediction of $m = n/83$ for our cavity system.

5.3.3. Detection error vs. scattering

We measure the detection error, and therefore I_{acc} , using the same thresholding method as discussed in chapter 4. Using different detection times at the same pump power, we determine the behavior of the detection error as a function of the number of incident photons. Using the measured scattering rate, we can then draw the detection error (or actually obtained information I_{acc}) as a function of the mean number of scattered photons. Figure 5.8 shows the measured I_{acc} alongside the curve expected from theory and the measured scattering rate, $I_H((5.4 \pm 0.9)m)$. Additionally, the information attainable in an ideal free-space measurement is shown. Unlike the theory curve, the measured detection error saturates for high n due to quantum jumps between the two hyperfine states which we neglected in the theory. The minimum detection error is around 9×10^{-3} ,

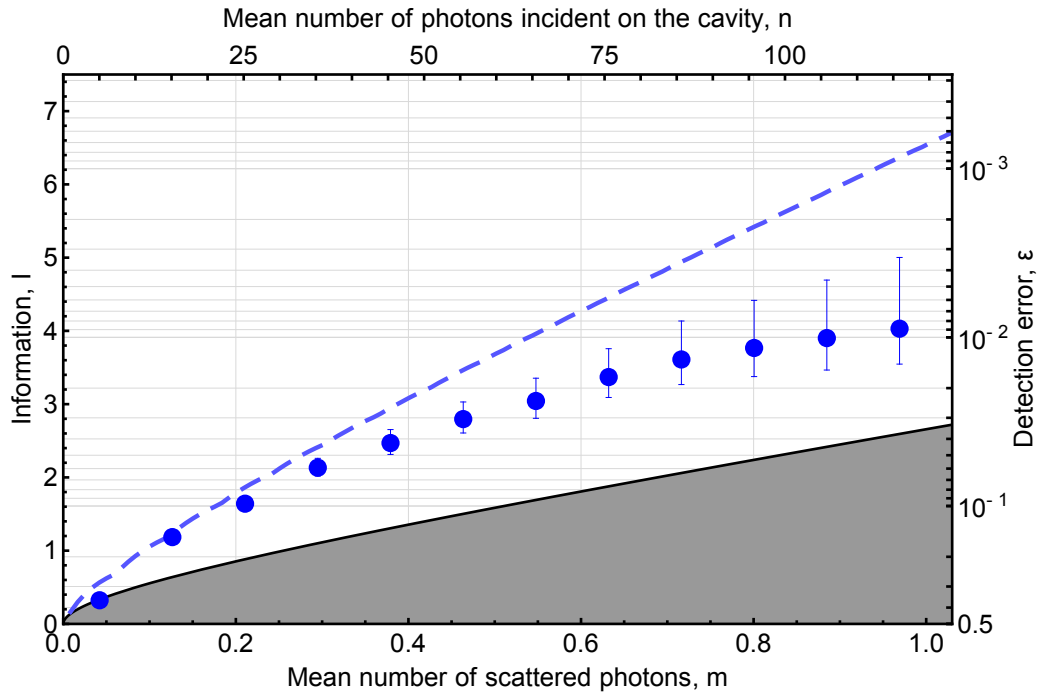


Figure 5.8.: The measured detection error and I_{acc} (blue circles), expected behavior of the accessible information as $I_{\text{acc}} = I_H(5.4m)$ (dashed blue line), and the detection error attainable for free-space measurements (grey area). The upper x-Axis shows the number of incident photons n , the lower x-Axis the number of scattered photons m . The deviation of the measured detection efficiencies from the theory curve is due to hyperfine changing scattering events.

larger than the one obtained in chapter 4. This is due to the non-optimum parameters used here, in particular the π polarized probe light and the magnetic field orientation along the probe light polarization.

In the regime $m \ll 1$, where the detection error is not limited by depumping, we find good agreement with the theoretical curve $I_H(5.4m)$. In spite of experimental imperfections, the information accessible to us is a factor of 2.7 higher than possible in an ideal fluorescence measurement. This translates to more than two orders of magnitudes compared to state of the art fluorescence experiments ([128]).

5.4. Measurement of the Helstrom bound of the atom-cavity system

In this section, we show how we measure the quantity of the total information extracted by the measurement. We present the relationship between the quantum Zeno effect and the Helstrom bound, and how we use this relation to measure I_{tot} .

5.4.1. The quantum Zeno effect

The quantum Zeno effect was first described by Sudarshan and Misra [129], under the title of quantum Zeno paradox. In the original form, it refers to the situation of an unstable particle under continuous observation. According to Misra and Sudarshan, the particle will never decay in these conditions, i.e. in the limit of infinitely frequent measurements. The resolution to the paradox that unstable particles do indeed decay when observed for example in a bubble chamber lies in the insufficiently frequent interactions between the particle and its environment.

The quantum Zeno effect has since enjoyed significant interest in both theoretical and experimental work. In experiments, the quantum Zeno effect is usually demonstrated not by inhibiting the decay of an unstable particle (since the quadratic part of the evolution ends prohibitively fast), but by preventing a Rabi oscillation imposed externally. As in a spontaneous decay, the state population dynamics in a Rabi oscillation is initially quadratic, such that the same formalism can be used. The first experimental observation of the Zeno effect was achieved on an ensemble of trapped ions ([130]), using the fluorescence detection method as measurement device. Since then, the effect has been observed on a number of systems, including single ions ([131]), neutral atoms ([132]), microwave photons in a cavity ([133]) and Bose-Einstein condensates ([134]). The experiment described in ([135]) is the only one achieved so far where the original proposition of Misra and Sudarshan of the Zeno effect on an unstable quantum state was observed.

5.4.2. Zeno effect on a single atom coupled to the cavity

Here, we are interested in the quantum Zeno effect on a single atom strongly coupled to our cavity. Consider the following situation: An atom in either $|0\rangle$ or $|1\rangle$ is prepared in the cavity. A MW pulse is then applied on the $|0\rangle \leftrightarrow |1\rangle$ transition. While the MW is turned on, we simultaneously apply detection light with variable pump strength η . The incident light measures the atomic state as described before. When the incident light power is strong enough, a significant Zeno effect occurs and prevents the Rabi oscillations induced by the microwave radiation.

To describe this system, we use the formalism of Bloch equations (BE), i.e. a master equation for the reduced atomic (or qubit) density matrix ρ_A . In the absence of probe

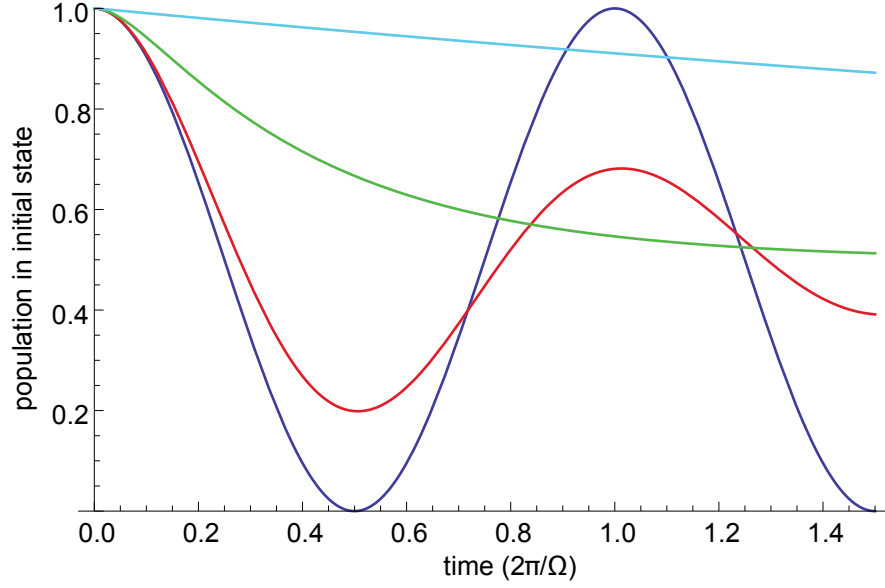


Figure 5.9.: Illustration of the Zeno effect, here seen as an effect of measurements on a driven Rabi oscillation. Measurements are distributed randomly over time with a rate Γ_m . The measurements rate are $\Gamma_m/\Omega = 0$ (blue), $1/3$ (red), 3 (green), 30 (light blue). The Zeno effect is most easily seen for a π -pulse ($t=0.5$), where the measurements drastically decrease the transfer probability to the second qubit state.

light, the evolution of the qubit state is described by simple Rabi oscillations:

$$\frac{d\rho_{00}}{dt} = \Omega_R(\rho_{10} - \rho_{10}^*) \quad (5.22)$$

$$\frac{d\rho_{10}}{dt} = i\frac{\Omega_R}{2}(\rho_{00} - \rho_{11}) \quad (5.23)$$

To integrate the effect of the probe light on the evolution, we consider the master equation of the whole system, and in particular the Liouville term originating from cavity leakage (see [136])

$$\frac{d\rho}{dt} = \mathcal{L}_\kappa(\rho) = 2\kappa \left(a\rho a^\dagger - \frac{1}{2} \{a^\dagger a, \rho\} \right). \quad (5.24)$$

Assuming that the qubit state $|1\rangle$, which is resonant to cavity and probe light, completely blocks the probe light, we put $a = \alpha|0\rangle\langle 0|$, where $\alpha = \eta/\kappa$ (it can be verified that this approximation leads to the same results as numerical calculations of the full master equation, see [66, 136]). The evolution of the atomic part of the density matrix is obtained by tracing over the cavity variables, yielding

$$\mathcal{L}_\kappa(\rho_A) = 2\frac{\eta^2}{\kappa} \left(|0\rangle\langle 0|\rho_A|0\rangle\langle 0| - \frac{1}{2} \{|0\rangle\langle 0|, \rho_A\} \right) \quad (5.25)$$

Expressing this equation in the qubit base, we get the term to be added to the coherent evolution expressed in equation 5.22:

$$\frac{d\rho_{10}}{dt} = -\Gamma_m \rho_{10} \quad (5.26)$$

where $\Gamma_m = \eta^2/\kappa$. The effect of the probe light is therefore an exponential decay of the qubit coherence with a decay constant of Γ_m . The complete Bloch equations therefore are

$$\frac{d\rho_{00}}{dt} = \Omega_R(\rho_{10} - \rho_{10}^*) \quad (5.27)$$

$$\frac{d\rho_{10}}{dt} = i\frac{\Omega_R}{2}(\rho_{00} - \rho_{11}) - \Gamma_m \rho_{10} \quad (5.28)$$

Figure 5.9 shows the evolution of the qubit populations for different intensities of the probe light. For measurement rates above Ω , the Rabi oscillations are suppressed. Note how the transfer efficiency of a MW π -pulse goes from one to zero with increasing measurement rate.

The physical interpretation of the decay term in the density matrix's coherence is straightforward. Bloch equations like 5.27 have been shown ([137]) to be equivalent to a wave-function evolution with stochastically distributed perfect state projections. In this picture, the qubit evolves unitarily according to equations 5.22, but this evolution is interrupted at random times with a rate Γ_m . At these random times, the coherence of the qubit is set to zero, i.e. a perfect measurement of the qubit state occurs. This is the quantum Zeno effect for randomly distributed measurement intervals. The measurement rate η^2/κ is just the rate at which photons couple to the cavity, whereas spontaneous emission plays no role. In the above reasoning, the Liouville term for spontaneous emission can be neglected as long as $\gamma \ll \kappa$. Instead of spontaneously emitted photons, photons impinging onto the cavity lead to the measurement backaction on the qubit coherence.

We are now in a situation to establish the link between the Zeno effect and the Helstrom bound. For a measurement pulse of a given length t_d , the Bloch equations 5.27 predict a decay of the qubit's coherence by $\exp(-\Gamma_m t_d)$. Here, $\Gamma_m t_d = \tilde{n}$ is the average number of projective measurements occurring during the measurement time t_d . We have shown above (equation 5.11) that the coherence of the qubit is reduced by a factor corresponding to the overlap of the final light states $\langle \Psi_1 | \Psi_0 \rangle$. We thus have

$$\langle \Psi_1 | \Psi_0 \rangle = \exp(-\tilde{n}). \quad (5.29)$$

Measuring the strength of the Zeno effect therefore allows us to measure the overlap $\langle \Psi_1 | \Psi_0 \rangle$, and thereby the Helstrom bound I_{tot} of our detection method.

5.4.3. Zeno effect for a single atom

To observe the quantum Zeno effect, we perform the following experiment: We prepare an atom in either $|0\rangle$ or $|1\rangle$ coupled to the cavity. We apply a microwave π -pulse of

$\tau_\pi = 8.8 \mu\text{s}$ duration on the $|0\rangle \leftrightarrow |1\rangle$ transition. During the π -pulse of duration τ , we apply detection light of variable intensity. We then measure the final state of the atom, and thereby the probability of the π -pulse to have transferred the atom to the other clock state.

The measured transfer probability of the π -pulse as a function of the mean number of photons incident on the cavity is shown in figure 5.10 a). The measured transfer probability when no probe light is turned on is 95% for both initial states, limited by preparation and detection efficiencies. With increasing probe power, the transfer probability decreases to below 5%.

An anomaly can be seen for atoms initially in $|1\rangle$ for high probe powers. When pump strength increases to above 300 photons/ τ , the atom-cavity system starts to saturate, and the cavity transmission increases. As a consequence, the atom scattering rate is strongly increased until the atom is pumped to the off-resonant $F = 1$ hyperfine state during the π -pulse.

A given number of probe photons give rise to certain reduction in transfer probability. Using the model of the system (equations 5.27), we determine the number of projective measurements necessary to obtain this reduction in transfer probability. Figure 5.10 b) shows the relation between incident photons n and the number of projective measurements \tilde{n} . As expected, the relationship is linear, with a fit yielding $\tilde{n} = 0.37n$. This shows that every incident photon leads to a significant decrease in the qubit state's coherence. It is interesting to note that for $F = 2$ atoms, a strong quantum Zeno effect occurs for a negligible intracavity photon number.

5.4.4. The Helstrom bound

The measured projection rate from the Zeno effect allows us to obtain the Helstrom bound of our detection scheme. In terms of incident photons, the Helstrom bound is $I_{\text{tot}} = I_H(2\tilde{n}) = I_H((0.74 \pm 0.04)n)$. Given the measured scattering rate $m/n = 1/118$, this is equivalent to $I_H((87 \pm 17)m)$. Figure 5.11 shows this result (green curve). The right-hand y-axis in figure 5.11 shows the detection error we could obtain if we had access to all of I_{tot} . As an example, it would be possible to detect the qubit state with an error of 1% with less than 0.03 photons scattered on average. In reality, the accessible information $I_{\text{acc}} = I_H((5.4 \pm (0.9)n)$ is small compared to the total extracted information.

How much can this situation be improved? The orange curve in figure 5.11 shows the accessible information we could obtain if we had a lossless detection of all photons in the reflected and transmitted light modes without any change to the cavity itself. This would lead to approximately $I_{\text{acc}} = 14m$.

5.5. Conclusion

In this chapter, we have analyzed our detection scheme in terms of scattering caused during the detection. A measurement of the scattering rate induced by the probe light

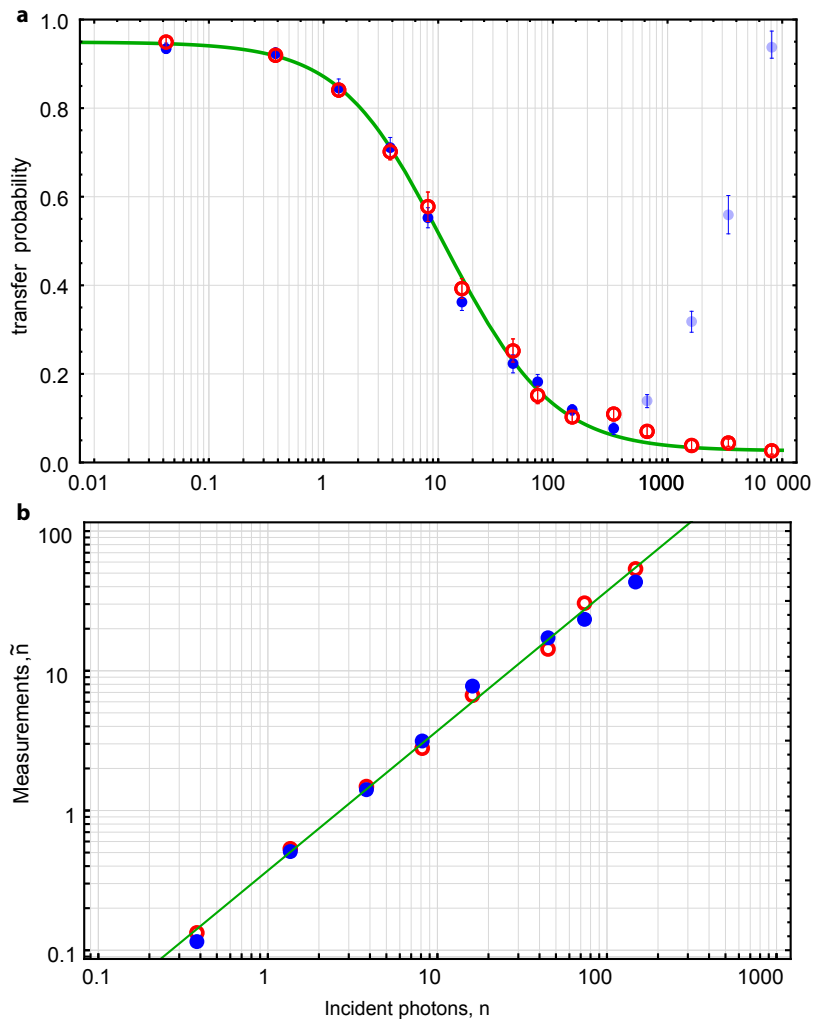


Figure 5.10.: Observation of the quantum Zeno effect. A MW π -pulse is applied to an atom initially in $|1\rangle$ (blue dots) or $|0\rangle$ (red circles). a) Data points show the transfer efficiency of the π -pulse as function of the number of photons incident on the cavity during the pulse. We model the qubit dynamics as described in the text. The bright blue points deviate from the theoretical curve because of depumping into state $F = 1$ for that happens for strongly saturating pump power. b) The average number of projective measurements \tilde{n} we deduce for each data point from our model; the solid line is a linear fit, yielding $\tilde{n} = (0.37 \pm 0.02)n$. The solid line in a) shows the prediction of the model supposing this linear relation.

showed that a read-out of the qubit state with an error below 10% is possible with less than a single spontaneously emitted photon. We then presented a quantum Zeno type experiment to quantify the projection caused by the incident photons.

Together, these results constitute a full experimental characterization of a quantum

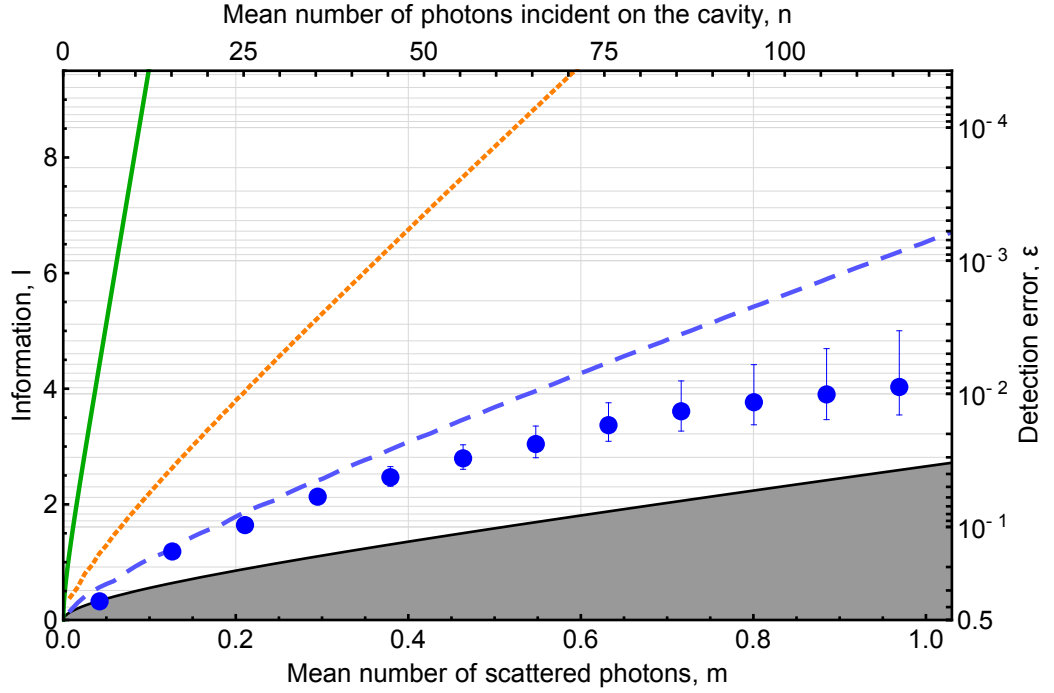


Figure 5.11.: Detection error and information versus the number of scattered photons. The gray area is the range accessible to free-space detection schemes. The green line is the total information I_{tot} extracted by the cavity measurement, deduced from the data from the Zeno effect (figure 5.10). The orange dotted line is the information accessible in our experiment using perfect photon counters to detect reflected and transmitted photons. Blue dots and dotted line are as in figure 5.8.

measurement in the energy exchange free regime below a single spontaneous emission event. Besides its fundamental interest, the scheme could lead to significant simplification for proposed neutral atom computation schemes. Furthermore, it may enable sensitive detection of molecules and atoms lacking closed transitions.

For future implementations, the cavity could quite easily be improved. Cavity losses can be reduced by at least a factor of four ([69]) simply by using state of the art mirror coatings in an otherwise identical fiber cavity.

Furthermore, the closely spaced second cavity is a limiting factor since it leads to increased scattering. By making the birefringence that causes it much larger than g_0 ($\Delta_{bi} \gg g_0$), the second mode could be made far-detuned to the atom. In the limit of a far-detuned mode, the Purcell-enhanced atomic decay rate is $2g_d^2\kappa/\Delta_{bi}^2$, where g_d is the coupling between the atom and the detuned mode. With a birefringence increased

by a factor of 4 from the current value of 540 MHz, this scattering would be made negligible. With these improvements and a photon detection efficiency of 70%, the accessible information would increase to $I_{\text{acc}} \approx I_H(110m)$.

6. Conclusion and Outlook

The experiments presented in this thesis demonstrate an unprecedented control over the external and internal state of a single atom on an atom chip. We have presented a complete set of techniques allowing the preparation of an ultracold atom at the exact center of a miniature high-finesse cavity, leading to a deterministic strong coupling between the atom and the cavity light mode. Since the single atom preparation starts with a Bose-Einstein condensate, the method presents a new way to obtain ground state single atoms that does not require cooling methods such as resolve sideband cooling that are difficult to implement for neutral atoms.

The regime of very high cooperativity that is realized in the atom-cavity system enables us to implement a hyperfine state read-out that surpasses previous neutral atom detection methods in both fidelity and detection time. We presented two methods to read out the hyperfine state of the atom based on cavity reflection and transmission. We reached a read-out fidelity of 99.93% in a detection time of 100 μs , and 99.4% in 2 μs . The fidelities obtained are as good as those reached in the best ion trap experiments.

Our cavity-based detection method does not rely on spontaneous emission, as we have shown by measuring the scattering rate of the atom during detection. A state read-out with less than one spontaneous emission event is therefore possible. Together with the measurement of the atomic state collapse induced by single photons incident on the cavity, our result constitute a full experimental characterization of a measurement in the energy exchange free regime.

Due to the combination of outstanding capabilities, the presented state detection could lead to a variety of applications. For quantum information purposes, the possibility of high-fidelity state detection while staying in the ground state of the trap removes the necessity of recooling after read-out. A drastic improvement in the cycling time of atom-based quantum computing schemes could therefore be obtained. In view of recently realized state-dependent microwave potentials [138], the elements for chip-based two-qubit gates with neutral atoms have now been demonstrated. An atom chip combining a microwave stripline and a fiber cavity could enable the realization of a collisional phase gate [139, 140].

Instead of single atoms, we can also prepare small ensemble of atoms, all of which identically couple to the cavity. Experiments in the little explored regime of tens of atoms are therefore possible. Using off-resonant probe light, the non-destructive observation of Rabi oscillations of these small ensembles are possible [141]. An interesting possibility would be the measurement of the onset of the quantum Zeno effect by increasing the measurement strength while decreasing the atom number, thereby mapping out a transition from a classical measurement regime to a regime dominated by quantum state projection.

Exciting a single atom from a reservoir into a different state, in the way presented in this thesis, leads to the creation of a symmetrical Dicke state [142], since the flipped spin is shared among all atoms. A tomography of the state can be implemented in a straightforward manner using microwave induced state rotations and the cavity-based hyperfine state detection.

A. Appendix

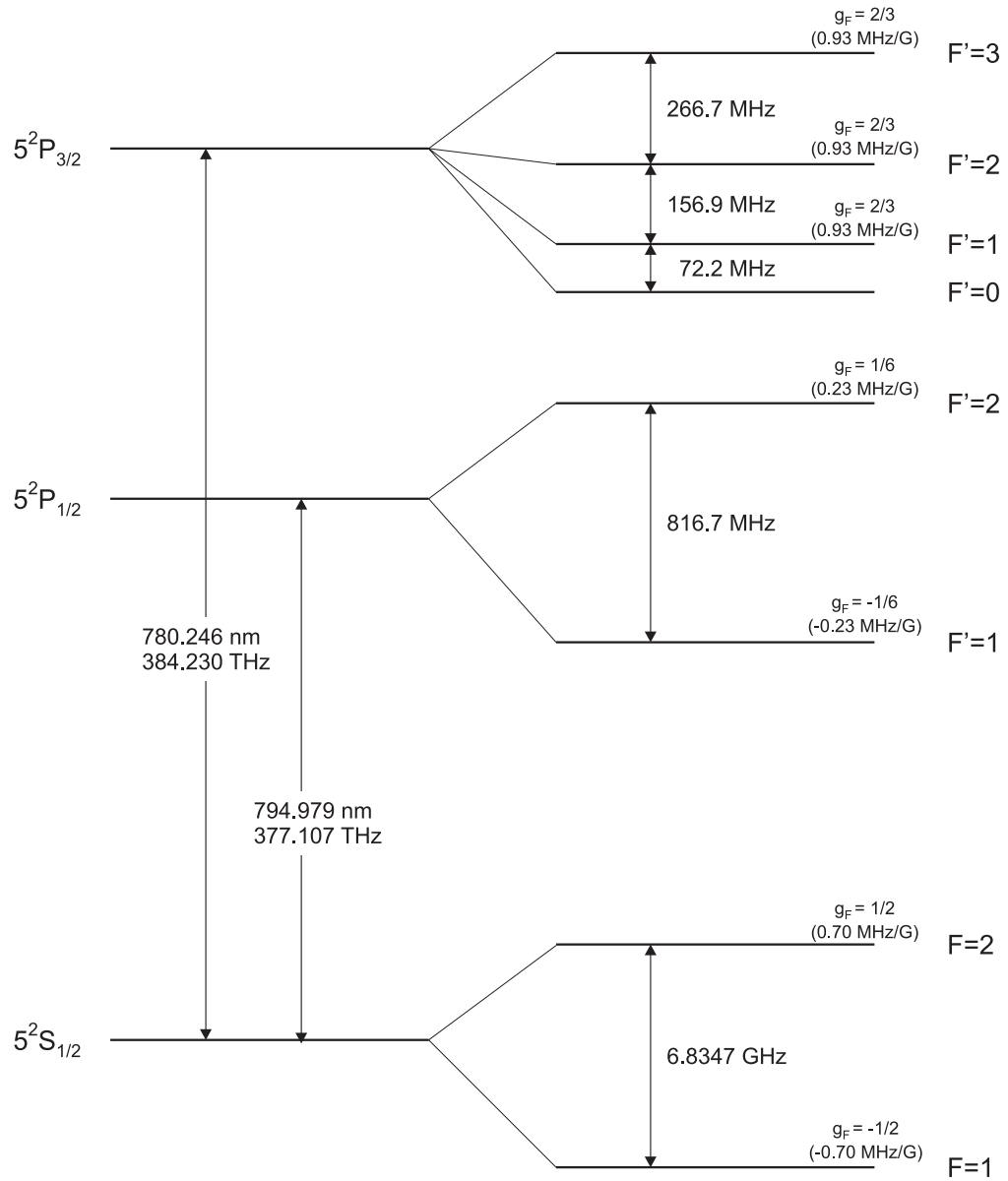
A.1. Rubidium data

A.1.1. Physical properties

Atomic Number	Z	37
Total nucleons	Z+N	87
Relative natural abundance		27.83%
Nuclear spin	I	3.2
Atomic mass	M	86.9092 u
Vacuum wavelength D_1 transition	λ_{D_1}	794.979 nm
Vacuum wavelength D_2 transition	λ_{D_2}	780.246 nm
Lifetime $5^2P_{1/2}$	τ_{D_1}	27.70 ns
Lifetime $5^2P_{3/2}$	τ_{D_2}	26.24 ns
Natural line width D_1 transition	Γ_{D_1}	$2\pi \times 5.746(8)$ MHz
Natural line width D_2 transition	Γ_{D_2}	$2\pi \times 6.065(9)$ MHz
Ground state hyperfine splitting	ν_{HFS}	6834.68 MHz
D_2 transition recoil velocity	v_R	5.885 mm/s
D_2 transition recoil temperature	T_R	361.95 nK
D_2 transition Doppler velocity	v_D	11.75 cm/s
D_2 transition Doppler Temperature	T_D	146 μ K
D_2 transition dipole matrix element	$\langle J \hat{d} J'\rangle$	$3.584(4) \times 10^{-29}$ Cm
Saturation intensity $5^2S_{1/2}, F = 2, m_F = \pm 2 \rightarrow$ $5^2P_{3/2}, F = 3, m_F = \pm 3$	I_{sat}	1.67 mW/cm ²

Table A.1.: Physical properties of ^{87}Rb . From [143]

A.1.2. Hyperfine structure

Figure A.1.: ^{87}Rb hyperfine structure of the D_1 and D_2 transitions. From [143]

A.2. APD correction factor

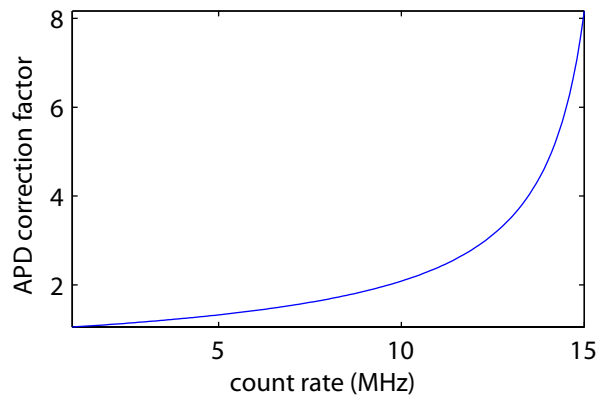


Figure A.2.: The APD correction factor as a function of count rate. Saturation is reached for around 15×10^6 counts/s.

A.3. Publications

Publications related to this thesis:

- *Cavity-Based Single Atom Preparation and High-Fidelity Hyperfine State Readout*
Roger Gehr, Jürgen Volz, Guilhem Dubois, Tilo Steinmetz, Yves Colombe, Benjamin L. Lev, Romain Long, Jérôme Estève, and Jakob Reichel
Phys. Rev. Lett. **104**, 203602 (2010)
- *Measuring the internal state of a single atom without energy exchange*
Jürgen Volz, Roger Gehr, Guilhem Dubois, Jérôme Estève, and Jakob Reichel
accepted for publication in Nature

Bibliography

- [1] M. Planck. Über das Gesetz der Energieverteilung im Normalspektrum. *Annalen der Physik*, 4:553, 1901.
- [2] A. Einstein. Über einen die Erzeugung und Verwandlung des Lichtes betreffenden heuristischen Gesichtspunkt. *Annalen der Physik*, 322:132–148, 1905.
- [3] P Berman, editor. *Cavity Quantum Electrodynamics (Advances in Atomic, Molecular and Optical Physics)*. Academic Press, January 1994.
- [4] S. Haroche and J.-M. Raimond. *Exploring the Quantum: Atoms, Cavities and Photons*. Oxford University Press, 2006.
- [5] E. M. Purcell. Spontaneous emission probabilities at radio frequencies. *Phys. Rev.*, 69,:681–, 1946.
- [6] J. M. Raimond, M. Brune, and S. Haroche. Colloquium: manipulating quantum entanglement with atoms and photons in a cavity. *Rev. Mod. Phys.*, 73:565–582, 2001.
- [7] E. Jaynes and F. Cummings. Comparison of quantum and semiclassical radiation theories with application to the beam maser. *Proc. IEEE*, 51:89–109, 1963.
- [8] Bruce W. Shore and Peter L. Knight. The Jaynes-Cummings model. *Journal of Modern Optics*, 40(7):1195–1238, 1993.
- [9] Y. Kaluzny, P. Goy, M. Gross, J. M. Raimond, and S. Haroche. Observation of self-induced rabi oscillations in two-level atoms excited inside a resonant cavity: The ringing regime of superradiance. *Phys. Rev. Lett.*, 51(13):1175–, September 1983.
- [10] D. Meschede, H. Walther, and G. Mueller. One-atom maser. *Physical review letters*, 54(6):551–554, 1985.
- [11] G. Rempe, H. Walther, and N. Klein. Observation of quantum collapse and revival in a one-atom maser. *Physical review letters*, 58(4):353–356, 1987.
- [12] M. Brune, JM Raimond, P. Goy, L. Davidovich, and S. Haroche. Realization of a two-photon maser oscillator. *Physical review letters*, 59(17):1899–1902, 1987.

- [13] M. Brune, P. Nussenzveig, F. Schmidt-Kaler, F. Bernardot, A. Maali, J. M. Raimond, and S. Haroche. From lamb shift to light shifts: Vacuum and subphoton cavity fields measured by atomic phase sensitive detection. *Phys. Rev. Lett.*, 72(21):3339–, May 1994.
- [14] H. Walther. Quantum phenomena of single atoms. *Adv. Chem. Phys.*, 122:167–197, 2002.
- [15] G. Rempe, R. J. Thompson, R. J. Brecha, W. D. Lee, and H. J. Kimble. Optical bistability and photon statistics in cavity quantum electrodynamics. *Phys. Rev. Lett.*, 67(13):1727–, September 1991.
- [16] R. J. Thompson, G. Rempe, and H. J. Kimble. Observation of normal-mode splitting for an atom in an optical cavity. *Phys. Rev. Lett.*, 68:1132–1135, 1992.
- [17] P. W. H. Pinkse, T. Fischer, P. Maunz, and G. Rempe. Trapping an atom with single photons. *Nature*, 404:365–368, 2000.
- [18] C. J. Hood, T. W. Lynn, A. C. Doherty, A. S. Parkins, and H. J. Kimble. The atom-cavity microscope: single atoms bound in orbit by single photons. *Science*, 287:1447–1453, 2000.
- [19] A. Boca, R. Miller, K. M. Birnbaum, A. D. Boozer, J. McKeever, and H. J. Kimble. Observation of the vacuum rabi spectrum for one trapped atom. *Phys. Rev. Lett.*, 93(23):233603–, December 2004.
- [20] P. Maunz, T. Puppe, I. Schuster, N. Syassen, P. W. H. Pinkse, and G. Rempe. Cavity cooling of a single atom. *Nature*, 428(6978):50–52, March 2004.
- [21] H. J. Kimble. Strong interactions of single atoms and photons in cavity qed. *Phys. Scr.*, T76:127–137, 1998.
- [22] A. Ottl, S. Ritter, M. Kohl, and T. Esslinger. Correlations and counting statistics of an atom laser. *Phys. Rev. Lett.*, 95:090404–, 2005.
- [23] A. Imamoglu, D. D. Awschalom, G. Burkard, D. P. DiVincenzo, D. Loss, M. Sherwin, and A. Small. Quantum information processing using quantum dot spins and cavity qed. *Phys. Rev. Lett.*, 83(20):4204–, November 1999.
- [24] G. S. Solomon, M. Pelton, and Y. Yamamoto. Single-mode spontaneous emission from a single quantum dot in a three-dimensional microcavity. *Phys. Rev. Lett.*, 86(17):3903–, April 2001.
- [25] T. Yoshie, A. Scherer, J. Hendrickson, G. Khitrova, H. M. Gibbs, G. Rupper, C. Ell, O. B. Shchekin, and D. G. Deppe. Vacuum rabi splitting with a single quantum dot in a photonic crystal nanocavity. *Nature*, 432(7014):200–203, November 2004.

- [26] J. P. Reithmaier, G. Sek, A. Löffler, C. Hofmann, S. Kuhn, S. Reitzenstein, L. V. Keldysh, V. D. Kulakovskii, T. L. Reinecke, and A. Forchel. Strong coupling in a single quantum dot-semiconductor microcavity system. *Nature*, 432(7014):197–200, November 2004.
- [27] G. Khitrova, H. M. Gibbs, M. Kira, S. W. Koch, and A. Scherer. Vacuum rabi splitting in semiconductors. *Nat Phys*, 2(2):81–90, February 2006.
- [28] A. Wallraff, D. I. Schuster, A. Blais, L. Frunzio, R.-S. Huang, J. Majer, S. Kumar, S. M. Girvin, and R. J. Schoelkopf. Strong coupling of a single photon to a superconducting qubit using circuit quantum electrodynamics. *Nature*, 431(7005):162–167, September 2004.
- [29] JM Fink, M. Göppl, M. Baur, R. Bianchetti, PJ Leek, A. Blais, and A. Wallraff. Climbing the Jaynes–Cummings ladder and observing its nonlinearity in a cavity QED system. *Nature*, 454(7202):315–318, 2008.
- [30] Frank Deppe, Matteo Mariani, E. P. Menzel, A. Marx, S. Saito, K. Kakuyanagi, H. Tanaka, T. Meno, K. Semba, H. Takayanagi, E. Solano, and R. Gross. Two-photon probe of the jaynes-cummings model and controlled symmetry breaking in circuit qed. *Nat Phys*, 4(9):686–691, September 2008.
- [31] M. Brune, F. Schmidt-Kaler, A. Maali, J. Dreyer, E. Hagley, J. M. Raimond, and S. Haroche. Quantum rabi oscillation: A direct test of field quantization in a cavity. *Phys. Rev. Lett.*, 76(11):1800–, March 1996.
- [32] Samuel Deleglise, Igor Dotsenko, Clement Sayrin, Julien Bernu, Michel Brune, Jean-Michel Raimond, and Serge Haroche. Reconstruction of non-classical cavity field states with snapshots of their decoherence. *Nature*, 455(7212):510–514, September 2008.
- [33] Christine Guerlin, Julien Bernu, Samuel Deleglise, Clement Sayrin, Sebastien Gleyzes, Stefan Kuhr, Michel Brune, Jean-Michel Raimond, and Serge Haroche. Progressive field-state collapse and quantum non-demolition photon counting. *Nature*, 448(7156):889–893, August 2007.
- [34] Ferdinand Brennecke, Stephan Ritter, Tobias Donner, and Tilman Esslinger. Cavity optomechanics with a bose-einstein condensate. *Science*, 322(5899):235–238, 2008.
- [35] Paul Benioff. The computer as a physical system: A microscopic quantum mechanical hamiltonian model of computers as represented by turing machines. *Journal of Statistical Physics*, 22(5):563–591, 1980-05-01.
- [36] D Deutsch. Quantum Theory, the Church-Turing Principle and the Universal Quantum Computer. *Proceedings of the Royal Society of London A*, 400:97–117, 1985.

- [37] C. H. Bennett and D. P. DiVincenzo. Quantum computing-towards an engineering era? *Nature*, 377:389–390, 1995.
- [38] Charles H. Bennett and David P. DiVincenzo. Quantum information and computation. *Nature*, 404(6775):247–255, March 2000.
- [39] Richard Feynman. Simulating physics with computers. *International Journal of Theoretical Physics*, 21(6):467–488, June 1982.
- [40] H. Mabuchi and A. C. Doherty. Cavity quantum electrodynamics: coherence in context. *Science*, 298:1372–1377, 2002.
- [41] J. Pachos and H. Walther. Quantum computation with trapped ions in an optical cavity. *Physical Review Letters*, 89(18):187903, 2002.
- [42] B. Tregenna, A. Beige, and P.L. Knight. Quantum computing in a macroscopic dark period. *Physical Review A*, 65(3):32305, 2002.
- [43] L. You, XX Yi, and XH Su. Quantum logic between atoms inside a high-Q optical cavity. *Physical Review A*, 67(3):32308, 2003.
- [44] S. J. van Enk, H. J. Kimble, and H. Mabuchi. Quantum information processing in cavity-qed. *Quantum Inform. Process.*, 3:75–90, 2004.
- [45] T. Pellizzari, S. A. Gardiner, J. I. Cirac, and P. Zoller. Decoherence, continuous observation, and quantum computing: A cavity qed model. *Phys. Rev. Lett.*, 75(21):3788–, November 1995.
- [46] L.-M. Duan, M. D. Lukin, J. I. Cirac, and P. Zoller. Long-distance quantum communication with atomic ensembles and linear optics. *Nature*, 414(6862):413–418, November 2001.
- [47] J. I. Cirac, P. Zoller, H. J. Kimble, and H. Mabuchi. Quantum state transfer and entanglement distribution among distant nodes in a quantum network. *Phys. Rev. Lett.*, 78:3221–3224, 1997.
- [48] A. Kuhn, M. Hennrich, and G. Rempe. Deterministic single-photon source for distributed quantum networking. *Phys. Rev. Lett.*, 89:067901–067901, 2002.
- [49] Tatjana Wilk, Simon C. Webster, Axel Kuhn, and Gerhard Rempe. Single-atom single-photon quantum interface. *Science*, 317(5837):488–490, 2007.
- [50] A. D. Boozer, A. Boca, R. Miller, T. E. Northup, and H. J. Kimble. Reversible state transfer between light and a single trapped atom. *Physical Review Letters*, 98(19):193601, 2007.
- [51] W. Ketterle, D.S. Durfee, and D.M. Stamper-Kurn. Making, probing and understanding bose-einstein condensates. *Arxiv preprint cond-mat/9904034*, 1999.

- [52] F. Diedrich, J. C. Bergquist, Wayne M. Itano, and D. J. Wineland. Laser cooling to the zero-point energy of motion. *Phys. Rev. Lett.*, 62(4):403–, January 1989.
- [53] P. Munstermann, T. Fischer, P. W. H. Pinkse, and G. Rempe. Single slow atoms from an atomic fountain observed in a high-finesse optical cavity. *Opt. Commun.*, 159:63–67, 1999.
- [54] J. Ye, D. W. Vernooy, and H. J. Kimble. Trapping of single atoms in cavity qed. *Phys. Rev. Lett.*, 83:4987–4990, 1999.
- [55] M Khudaverdyan, W Alt, I Dotsenko, T Kampschulte, K Lenhard, A Rauschenbeutel, S Reick, K Schörner, A Widera, and D Meschede. Controlled insertion and retrieval of atoms coupled to a high-finesse optical resonator. *New Journal of Physics*, 10(7):073023 (16pp), 2008.
- [56] P. Maunz, T. Puppe, I. Schuster, N. Syassen, P. W. H. Pinkse, and G. Rempe. Normal-mode spectroscopy of a single-bound-atom-cavity system. *Phys. Rev. Lett.*, 94(3):033002–, January 2005.
- [57] Ferdinand Brennecke, Tobias Donner, Stephan Ritter, Thomas Bourdel, Michael Kohl, and Tilman Esslinger. Cavity qed with a bose-einstein condensate. *Nature*, 450(7167):268–271, November 2007.
- [58] Yves Colombe, Tilo Steinmetz, Guilhem Dubois, Felix Linke, David Hunger, and Jakob Reichel. Strong atom-field coupling for Bose-Einstein condensates in an optical cavity on a chip. *Nature*, 450(7167):272–276, November 2007.
- [59] A. H. Myerson, D. J. Szwer, S. C. Webster, D. T. C. Allcock, M. J. Curtis, G. Imreh, J. A. Sherman, D. N. Stacey, A. M. Steane, and D. M. Lucas. High-fidelity readout of trapped-ion qubits. *Phys. Rev. Lett.*, 100(20):200502–4, May 2008.
- [60] H.J. Carmichael. *An Open Systems Approach to Quantum Optics*. Springer-Verlag, 1992.
- [61] M. J. Collett and C. W. Gardiner. Squeezing of intracavity and traveling-wave light fields produced in parametric amplification. *Phys. Rev. A*, 30(3):1386–1391, Sep 1984.
- [62] P. Goy, J. M. Raimond, M. Gross, and S. Haroche. Observation of cavity-enhanced single-atom spontaneous emission. *Phys. Rev. Lett.*, 50(24):1903–, June 1983.
- [63] Gerald Hechenblaikner, Markus Gangl, Peter Horak, and Helmut Ritsch. Cooling an atom in a weakly driven high-q cavity. *Phys. Rev. A*, 58(4):3030–, October 1998.
- [64] K. Murr. On the suppression of the diffusion and the quantum nature of a cavity mode. Optical bistability: Forces and friction in driven cavities. *J. Phys. B*, 36,:2515–2537, 2003.

- [65] LA Lugiato. Theory of optical bistability. *Progress in optics*, 21:69–216, 1984.
- [66] Guilhem Dubois. *Préparation, manipulation et détection d'atomes uniques sur une puce à atome*. PhD thesis, LKB/ENS, 2010.
- [67] Peter Maunz. *Cavity cooling and spectroscopy of a bound atom-cavity system*. PhD thesis, Max Plack Institut fur Quanten Optik, 2005.
- [68] R Grimm, M Weidemuller, and Yu B Ovchinnikov. Optical dipole traps for neutral atoms. *Adv. At. Mol. Opt. Phys.*, 42:95–170, 2000.
- [69] D Hunger, T Steinmetz, Y Colombe, C Deutsch, T W Hänsch, and J Reichel. A fiber fabry-perot cavity with high finesse. *New Journal of Physics*, 12(6):065038–, 2010.
- [70] Tilo Steinmetz. *Resonator-Quantenelektrodynamik auf einem Mikrofallenchip*. PhD thesis, Ludwig-Maximilians-Universität München, 2008.
- [71] J. D. Jackson. *Classical electrodynamics*. Wiley, 3rd edition, 1998.
- [72] William D. Phillips, John V. Prodan, and Harold J. Metcalf. Laser cooling and electromagnetic trapping of neutral atoms. *J. Opt. Soc. Am. B*, 2(11):1751–1767, November 1985.
- [73] J. Reichel, W. Hansel, and T. W. Hansch. Atomic micromanipulation with magnetic surface traps. *Phys. Rev. Lett.*, 83:3398–3401, 1999.
- [74] W. Hansel, P. Hommelhoff, T. W. Hansch, and J. Reichel. Bose-einstein condensation on a microelectronic chip. *Nature*, 413:498–501, 2001.
- [75] R. Folman, P. Kruger, J. Schmiedmayer, J. Denschlag, and C. Henkel. Microscopic atom optics: From wires to an atom chip. *Adv. At. Mol. Opt. Phys.*, 48:263–356, 2002.
- [76] Kenneth Maussang, G. Edward Marti, Tobias Schneider, Philipp Treutlein, Yun Li, Alice Sinatra, Romain Long, Jérôme Estève, and Jakob Reichel. Enhanced and reduced atom number fluctuations in a bec splitter. *Phys. Rev. Lett.*, 105(8):080403–, August 2010.
- [77] L Ricci. A compact grating-stabilized diode laser system for atomic physics. *Optics Communications*, 117(5-6):541–549, June 1995.
- [78] Gary C. Bjorklund. Frequency-modulation spectroscopy: a new method for measuring weak absorptions and dispersions. *Opt. Lett.*, 5(1):15–17, January 1980.
- [79] G. C. Bjorklund, M. D. Levenson, W. Lenth, and C. Ortiz. Frequency modulation (fm) spectroscopy. *Applied Physics B: Lasers and Optics*, 32(3):145–152, 1983.

- [80] Theodor W. Haensch. Nobel lecture: Passion for precision. *Rev. Mod. Phys.*, 78(4):1297–, November 2006.
- [81] Ron Folman, Peter Krüger, Donatella Cassetari, Björn Hessmo, Thomas Maier, and Jörg Schmiedmayer. Controlling cold atoms using nanofabricated surfaces: Atom chips. *Phys. Rev. Lett.*, 84(20):4749–, May 2000.
- [82] A. Ottl, S. Ritter, M. Kohl, and T. Esslinger. Hybrid apparatus for bose-einstein condensation and cavity quantum electrodynamics: Single atom detection in quantum degenerate gases. *Rev. Sci. Instrum.*, 77:063118–, 2006.
- [83] A.E. Siegman. *Lasers*. University Science Books, Mill Valley, California, 1986.
- [84] M.B. Gray B.J.J. Salomon, D.A. Shaddock and D.E. McClelland. Frequency stability of spatial mode interference (tilt) locking. *IEEE J. Quantum Electron.*, 38:1521, 2002.
- [85] J. Dalibard and C. Cohen-Tannoudji. Laser cooling below the doppler limit by polarization gradients: simple theoretical models. *J. Opt. Soc. Am. B*, 6(11):2023–2045, November 1989.
- [86] H. Mabuchi, Q. A. Turchette, M. S. Chapman, and H. J. Kimble. Real-time detection of individual atoms falling through a high-finesse optical cavity. *Opt. Lett.*, 21:1393–1395, 1996.
- [87] Stefan Nussmann, Markus Hijlkema, Bernhard Weber, Felix Rohde, Gerhard Rempe, and Axel Kuhn. Submicron positioning of single atoms in a microcavity. *Physical Review Letters*, 95(17):173602, 2005.
- [88] J. A. Sauer, K. M. Fortier, M. S. Chang, C. D. Hamley, and M. S. Chapman. Cavity qed with optically transported atoms. *Phys. Rev. A.*, 69:051804–, 2004.
- [89] M. Khudaverdyan, W. Alt, T. Kampschulte, S. Reick, A. Thobe, A. Widera, and D. Meschede. Quantum jumps and spin dynamics of interacting atoms in a strongly coupled atom-cavity system. *Phys. Rev. Lett.*, 103(12):123006–, September 2009.
- [90] DM Harber, JM Obrecht, JM McGuirk, and EA Cornell. Measurement of the Casimir-Polder force through center-of-mass oscillations of a Bose-Einstein condensate. *Physical Review A*, 72(3):33610, 2005.
- [91] F. Bloch. Nuclear induction. *Phys. Rev.*, 70(7-8):460–, October 1946.
- [92] P. Horak, G. Hechenblaikner, K. M. Gheri, H. Stecher, and H. Ritsch. Cavity-induced atom cooling in the strong coupling regime. *Phys. Rev. Lett.*, 79:4974–4977, 1997.
- [93] D. B. Hume, T. Rosenband, and D. J. Wineland. High-fidelity adaptive qubit detection through repetitive quantum nondemolition measurements. *Phys. Rev. Lett.*, 99(12):120502–, September 2007.

- [94] D DiVincenzo. The physical implementation of quantum computation. *Fort. Phys.*, 48:771–793, 2000.
- [95] Jan Benhelm, Gerhard Kirchmair, Christian F. Roos, and Rainer Blatt. Towards fault-tolerant quantum computing with trapped ions. *Nat Phys*, 4(6):463–466, June 2008.
- [96] E. Knill. Quantum computing with realistically noisy devices. *Nature*, 434(7029):39–44, March 2005.
- [97] Robert Raussendorf and Jim Harrington. Fault-tolerant quantum computation with high threshold in two dimensions. *Phys. Rev. Lett.*, 98(19):190504–, May 2007.
- [98] Philipp Treutlein, Peter Hommelhoff, Tilo Steinmetz, Theodor W. Hänsch, and Jakob Reichel. Coherence in microchip traps. *Phys. Rev. Lett.*, 92(20):203005–, May 2004.
- [99] C. Monroe, D. M. Meekhof, B. E. King, W. M. Itano, and D. J. Wineland. Demonstration of a fundamental quantum logic gate. *Phys. Rev. Lett.*, 75(25):4714–, December 1995.
- [100] D. Jaksch, J. I. Cirac, P. Zoller, S. L. Rolston, R. Côte, and M. D. Lukin. Fast quantum gates for neutral atoms. *Phys. Rev. Lett.*, 85(10):2208–, September 2000.
- [101] L. Isenhower, E. Urban, X. L. Zhang, A. T. Gill, T. Henage, T. A. Johnson, T. G. Walker, and M. Saffman. Demonstration of a neutral atom controlled-not quantum gate. *Phys. Rev. Lett.*, 104(1):010503–, January 2010.
- [102] T. Wilk, A. Gaëtan, C. Evellin, J. Wolters, Y. Miroshnychenko, P. Grangier, and A. Browaeys. Entanglement of two individual neutral atoms using rydberg blockade. *Phys. Rev. Lett.*, 104(1):010502–, January 2010.
- [103] S. Kuhr, W. Alt, D. Schrader, I. Dotsenko, Y. Miroshnychenko, A. Rauschenbeutel, and D. Meschede. Analysis of dephasing mechanisms in a standing-wave dipole trap. *Phys. Rev. A*, 72(2):023406–, August 2005.
- [104] Jurgen Volz, Markus Weber, Daniel Schlenk, Wenjamin Rosenfeld, Johannes Vrana, Karen Saucke, Christian Kurtsiefer, and Harald Weinfurter. Observation of entanglement of a single photon with a trapped atom. *Phys. Rev. Lett.*, 96(3):030404–4, January 2006.
- [105] D. D. Yavuz, P. B. Kulatunga, E. Urban, T. A. Johnson, N. Proite, T. Henage, T. G. Walker, and M. Saffman. Fast ground state manipulation of neutral atoms in microscopic optical traps. *Phys. Rev. Lett.*, 96(6):063001–, February 2006.
- [106] M. P. A. Jones. Fast quantum state control of a single trapped neutral atom. *Phys. Rev. A*, 75:040301 (R)–, 2007.

- [107] Wenjamin Rosenfeld, Markus Weber, Jürgen Volz, Florian Henkel, Michael Krug, Adan Cabello, Marek Zukowski, and Harald Weinfurter. Towards a loophole-free test of bell's inequality with entangled pairs of neutral atoms. *Advanced Science Letters*, 2(4):469–474, December 2009.
- [108] M. L. Terraciano, R. Olson Knell, D. G. Norris, J. Jing, A. Fernandez, and L. A. Orozco. Photon burst detection of single atoms in an optical cavity. *Nat Phys*, 5(7):480–484, July 2009.
- [109] Makoto Takeuchi, Nobuyuki Takei, Kodai Doi, Peng Zhang, Masahito Ueda, and Mikio Kozuma. Single-nuclear-spin cavity qed. *Phys. Rev. A*, 81(6):062308–, June 2010.
- [110] A. D. Boozer, A. Boca, R. Miller, T. E. Northup, and H. J. Kimble. Cooling to the ground state of axial motion for one atom strongly coupled to an optical cavity. *Physical Review Letters*, 97(8):083602, August 2006.
- [111] T. Puppe, I. Schuster, A. Grothe, A. Kubanek, K. Murr, P. W. H. Pinkse, and G. Rempe. Trapping and observing single atoms in a blue-detuned intracavity dipole trap. *Phys. Rev. Lett.*, 99(1):013002–4, July 2007.
- [112] J. Bochmann, M. Mücke, C. Guhl, S. Ritter, G. Rempe, and D. L. Moehring. Lossless state detection of single neutral atoms. *Phys. Rev. Lett.*, 104(20):203601–, May 2010.
- [113] Michael J. Gibbons, Christopher D. Hamley, Chung-Yu Shih, and Michael S. Chapman. Nondestructive fluorescent state detection of single neutral atom qubits. *Phys. Rev. Lett.*, 106(13):133002–, March 2011.
- [114] A. Fuhrmanek, R. Bourgain, Y. R. P. Sortais, and A. Browaeys. Free-space lossless state detection of a single trapped atom. *Phys. Rev. Lett.*, 106(13):133003–, March 2011.
- [115] D. J. Wineland, J. C. Bergquist, Wayne M. Itano, and R. E. Drullinger. Double-resonance and optical-pumping experiments on electromagnetically confined, laser-cooled ions. *Opt. Lett.*, 5(6):245–247, June 1980.
- [116] W. Nagourney, J. Sandberg, and H. Dehmelt. Shelved optical electron amplifier-observation of quantum jumps. *Physical Review Letters (ISSN 0031-9007)*, 56, 1986.
- [117] JC Bergquist, R.G. Hulet, W.M. Itano, and DJ Wineland. Observation of quantum jumps in a single atom. *Physical review letters*, 57(14):1699–1702, 1986.
- [118] T. Sauter, W. Neuhauser, R. Blatt, and PE Toschek. Observation of quantum jumps. *Physical review letters*, 57(14):1696–1698, 1986.

- [119] S. Kuhr, W. Alt, D. Schrader, I. Dotsenko, Y. Miroshnychenko, W. Rosenfeld, M. Khudaverdyan, V. Gomer, A. Rauschenbeutel, and D. Meschede. Coherence properties and quantum state transportation in an optical conveyor belt. *Phys. Rev. Lett.*, 91(21):213002–, November 2003.
- [120] A. Lengwenus, J. Kruse, M. Volk, W. Ertmer, and G. Birkl. Coherent manipulation of atomic qubits in optical micropotentials. *Applied Physics B: Lasers and Optics*, 86(3):377–383, 2007-02-01.
- [121] Sebastien Gleyzes, Stefan Kuhr, Christine Guerlin, Julien Bernu, Samuel Deleglise, Ulrich Busk Hoff, Michel Brune, Jean-Michel Raimond, and Serge Haroche. Quantum jumps of light recording the birth and death of a photon in a cavity. *Nature*, 446(7133):297–300, March 2007.
- [122] Jay Gambetta, W. A. Braff, A. Wallraff, S. M. Girvin, and R. J. Schoelkopf. Protocols for optimal readout of qubits using a continuous quantum nondemolition measurement. *Phys. Rev. A*, 76(1):012325–11, July 2007.
- [123] Ferdinand Schmidt-Kaler, Hartmut Haffner, Mark Riebe, Stephan Gulde, Gavin P. T. Lancaster, Thomas Deuschle, Christoph Becher, Christian F. Roos, Jurgen Eschner, and Rainer Blatt. Realization of the cirac-zoller controlled-not quantum gate. *Nature*, 422(6930):408–411, March 2003.
- [124] C.W. Helstrom. Quantum detection and estimation theory. *Mathematics in science and engineering*, 123, 1976.
- [125] H Chernoff. A measure of asymptotic efficiency for tests of a hypothesis based on the sum of observations. *Ann. Math. Stat.*, 23:493–507, 1952.
- [126] J. J. Hope and J. D. Close. General limit to nondestructive optical detection of atoms. *Phys. Rev. A*, 71(4):043822–6, April 2005.
- [127] Peter Horak, Bruce G. Klappauf, Albrecht Haase, Ron Folman, Jörg Schmiedmayer, Peter Domokos, and E. A. Hinds. Possibility of single-atom detection on a chip. *Phys. Rev. A*, 67(4):043806–, April 2003.
- [128] S. Gerber, D. Rotter, M. Hennrich, R. Blatt, F. Rohde, C. Schuck, M. Almendros, R. Gehr, F. Dubin, and J. Eschner. Quantum interference from remotely trapped ions. *New Journal of Physics*, 11(1):013032–, 2009.
- [129] B. Misra and E. C. G. Sudarshan. The zeno’s paradox in quantum theory. *Journal of Mathematical Physics*, 18(4):756–763, 1977.
- [130] Wayne M. Itano, D. J. Heinzen, J. J. Bollinger, and D. J. Wineland. Quantum zeno effect. *Phys. Rev. A*, 41(5):2295–, March 1990.

- [131] Chr Balzer, R. Huesmann, W. Neuhauser, and P. E. Toschek. The quantum zeno effect - evolution of an atom impeded by measurement. *Optics Communications*, 180:115, 2000.
- [132] K. Mølhave and M. Drewsen. Demonstration of the continuous quantum zeno effect in optical pumping. *Physics Letters A*, 268(1-2):45–49, April 2000.
- [133] J. Bernu, S. Deléglise, C. Sayrin, S. Kuhr, I. Dotsenko, M. Brune, J. M. Raimond, and S. Haroche. Freezing coherent field growth in a cavity by the quantum zeno effect. *Phys. Rev. Lett.*, 101:180402, 2008.
- [134] Erik W. Streed, Jongchul Mun, Micah Boyd, Gretchen K. Campbell, Patrick Medley, Wolfgang Ketterle, and David E. Pritchard. Continuous and pulsed quantum zeno effect. *Phys. Rev. Lett.*, 97:260402, 2006.
- [135] T. Fischer, P. Maunz, T. Puppe, P. W. H. Pinkse, and G. Rempe. Collective light forces on atoms in a high-finesse cavity. *N. J. Phys.*, 3:11–, 2001.
- [136] JI Cirac. Interaction of a two-level atom with a cavity mode in the bad-cavity limit. *Physical Review A*, 46(7):4354–4362, 1992.
- [137] Jean Dalibard, Yvan Castin, and Klaus Mølmer. Wave-function approach to dissipative processes in quantum optics. *Phys. Rev. Lett.*, 68(5):580–, February 1992.
- [138] Pascal Bohi, Max F. Riedel, Johannes Hoffrogge, Jakob Reichel, Theodor W. Hansch, and Philipp Treutlein. Coherent manipulation of bose-einstein condensates with state-dependent microwave potentials on an atom chip. *Nat Phys*, 5(8):592–597, August 2009.
- [139] T. Calarco, E. A. Hinds, D. Jaksch, J. Schmiedmayer, J. I. Cirac, and P. Zoller. Quantum gates with neutral atoms: Controlling collisional interactions in time-dependent traps. *Phys. Rev. A*, 61(2):022304, Jan 2000.
- [140] Olaf Mandel, Markus Greiner, Artur Widera, Tim Rom, Theodor W. Hansch, and Immanuel Bloch. Controlled collisions for multi-particle entanglement of optically trapped atoms. *Nature*, 425(6961):937–940, October 2003.
- [141] Daniel Oblak, Plamen G. Petrov, Carlos L. Garrido Alzar, Wolfgang Tittel, Anton K. Vershovski, Jens K. Mikkelsen, Jens L. Sørensen, and Eugene S. Polzik. Quantum-noise-limited interferometric measurement of atomic noise: Towards spin squeezing on the cs clock transition. *Phys. Rev. A*, 71(4):043807–, April 2005.
- [142] H. Haffner, W. Hansel, C. F. Roos, J. Benhelm, D. Chek-al kar, M. Chwalla, T. Korber, U. D. Rapol, M. Riebe, P. O. Schmidt, C. Becher, O. Guhne, W. Dur, and R. Blatt. Scalable multiparticle entanglement of trapped ions. *Nature*, 438(7068):643–646, December 2005.
- [143] Daniel A. Steck. Rubidium 87 d line data (rev. 2008).

Acknowledgment

This thesis is the result of over three years of teamwork, and I would like to thank all those who were involved in its success. First of all, I am thankful to Jakob Reichel for giving me the opportunity to work in his group and on the cavity experiment. His advice throughout all stages of the thesis has been thoughtful, patient, and always helpful.

I was lucky to have Guilhem Dubois as a fellow PhD student during the first two years or so. I fondly remember many hours in the lab with him, experimenting, discussing and building stuff. Many thanks to him for always being cheerful and enthusiastic, and for following many a Federer-Nadal match with me.

Jürgen Volz was "my" post-doc during the whole thesis, and I could not have wished for a better colleague, or more knowledgeable physicist, to accompany long nights made short in the lab. I thank him for teaching me a great deal about physics and for being ready to explain anything at any time. I will miss the long discussion we had on just about any subject.

Thanks to Jérôme Estève for the insight and good ideas he brought to the experiment, as well as for remaining good-humored when unexpected measurement results turned out to be caused by errors in the experimental sequence...

I thank Yves Colombe for being very kind and helpful when introducing me to the experiment. It was a great pleasure to work on the experiment he and Tilo Steinmetz built so well.

I am thankful to all group members, past and present, for many discussions, helpful advice and just generally a good time. Kenneth Maussang, Romain Long, Christian Deutsch, Vincent Dugrain, Ed Marti and Yun Li were always great lab and office neighbors. I am very happy to leave the experiment in the hands of Florian Haas and Markus Zwerger and I thank them for their motivation to carry on the work.

I would like to thank my family, and especially my parents, for their continued support. I would not have been able to do this without them.

Thanks to Nathalie Hubaux for her love, kindness and support.